Multiphysical Modelling of Mechanical Behaviour of Soft Tissue: Application to Prostate

Behnam Esfandiar Jahromi

Submitted for the degree of Doctor of Philosophy

Heriot-Watt University

School of Engineering and Physical Sciences

August 2017

ABSTRACT

The aim of this thesis is to propose computational methodologies to analyse how the morphological and microstructural changes in the soft tissues, caused by various pathological conditions, influence the mechanical properties of tissue. More importantly, how such understanding could provide more insights into the mechanical properties of tissue for the purpose of quantitative diagnosis. To achieve this objective, statistical analysis of tissue microstructure based on image processing of tissue histology has been carried out. The influence of such microstructural changes due to different pathological conditions has also been compared to the mechanical properties of the tissue by means of the homogenization approach. To understand better the influence of fluid movement in viscoelastic behaviour of tissue, an optimization based method using numerical homogenization that is integrated with fluid-structure interaction (FSI) modelling is presented. The microstructures of soft tissue are treated as bi-phasic materials, solid material representing the cells and extracellular materials and fluid phase for the interstitial fluid. Such proposed method would be beneficial for quantitative assessment of mechanical properties of soft tissue, as well as understanding the role of multiscale microstructural features of soft tissues in its functionality. It is envisaged that this work will pave the road towards more precise characterization of mechanical properties of soft tissue which can be implemented to non-invasive diagnostic techniques, in order to improve the effectiveness of a range of diagnostic methods such as palpation for primary prostate diagnosis and, more importantly, the life quality of patients.

ACKNOWLEDGEMENTS

I would also like to express my gratitude to my supervisors Dr Yuhang Chen and Prof Bob Reuben for giving me the opportunity to pursue my PhD at Heriot-Watt and their constant support, encouragement and guidance.

I would like to thank Dr Daniel W. Good (University of Edinburgh, Edinburgh, UK), Dr Grant D. Stewart (Cambridge Cancer Centre, Cambridge, UK) and Prof S. Alan McNeill (Western General Hospital, NHS Lothian, Edinburgh, UK) for sharing key clinical data and their scientific insights for this thesis.

I would also like to thank the rest of our research group for their support and insightful comments. Thanks, Javi, Jess, Solenn, Frank, Antonio, Judith.

I am very grateful to Heriot-Watt University for the scholarship awarded to me which allowed me to continue my study.

I would like to thank all my friends who made this journey more interesting especially Giovanna for her continuous moral support.

Last, but certainly not least, I would like to thank my family: my parents and to my brother and my sister for supporting me spiritually throughout my study and my life in general.

DEDICATION

To my family.

“Strive not to be a success, but rather to be of value.”

Albert Einstein

LIST OF PUBLICATIONS

Journal Publications

1. **B. Esfandiar Jahromi**, J. Palacio-Torralba, D. W. Good, G. D. Stewart, S. Alan McNeill, R.L. Reuben and Y.Chen. Microstructure-induced Viscoelasticity in Soft Tissue - A Numerical Fluid-structure Interaction Analysis .*Journal of the Mechanical Behavior of Biomedical Materials*. *Submitted*

2. **B. Esfandiar Jahromi**, J. Palacio-Torralba, R. L. Reuben and Y. Chen. Image processing and structural characterization of prostatic histology .*To be submitted*

3. **B. Esfandiar Jahromi**, R. L. Reuben and Y. Chen. Tissue specific fluid-structure interaction modelling .*To be submitted.*

Conferences and Presentations

1. **B. Esfandiar Jahromi**, R. L. Reuben, Y, Chen. Fluid-Structure Interaction Based Multiscale Characterization Of Viscoelasticity In Soft Tissue. *22nd Congress of the European Society of Biomechanics*, Lyon, France, 2016.

2. J. Palacio-Torralba, E. Jiménez Aguilar, **B. Esfandiar Jahromi**, S.A. McNeill, G.D. Stewart, R.L. Reuben, Y. Chen. Patient specific modelling and quantitative tissue quality assessment for prostate cancer diagnosis. *21st Congress of the European Society of Biomechanics*, Prague, Czech Republic, 2015.

3. **B. Esfandiar Jahromi**, J. Palacio-Torralba, F. Yntema, R. L. Reuben, Y. Chen. Fluid-structure interaction and Optimization-based approach for homogenization of soft tissue viscoelasticity. *11th World Congress on Structural and Multidisciplinary Optimisation*. Sydney, Australia. 2015

4. **B. Esfandiar Jahromi**, R. L. Reuben, Y. Chen. Fluid-Structure interaction in biomaterials. *Simulia UK Academic Forum,* Glasgow, UK, 2015.

5. **B. Esfandiar Jahromi**, R. L. Reuben, Y, Chen. Fluid-Structure Interaction Based Multiscale Characterization Of Viscoelasticity In Soft Tissue In Soft Tissue. *4th IMPEE conference*, Edinburgh, UK, 2015

6. **B. Esfandiar Jahromi**, R. L. Reuben, Y, Chen. Multiscale Modelling and Structural Pathology of Soft Tissue *3rd IMPEE conference*, Edinburgh, UK, 2014

ACADEMIC REGISTRY

Research Thesis Submission

Name*:*	BEHNAM ESFANDIAR JAHROMI		
School/PGI:	Engineering and Physical Sciences		
Version: *(i.e. First, Resubmission, Final)*	First	Degree Sought (Award **and** Subject area)	Ph.D. in Mechanical Engineering

---

Declaration

In accordance with the appropriate regulations I hereby submit my thesis and I declare that:

1) the thesis embodies the results of my own work and has been composed by myself
2) where appropriate, I have made acknowledgement of the work of others and have made reference to work carried out in collaboration with other persons
3) the thesis is the correct version of the thesis for submission and is the same version as any electronic versions submitted*.
4) my thesis for the award referred to, deposited in the Heriot-Watt University Library, should be made available for loan or photocopying and be available via the Institutional Repository, subject to such conditions as the Librarian may require
5) I understand that as a student of the University I am required to abide by the Regulations of the University and to conform to its discipline.

* *Please note that it is the responsibility of the candidate to ensure that the correct version of the thesis is submitted.*

Signature of Candidate*:*		Date:	

Submission

Submitted By *(name in capitals):*	BEHNAM ESFANDIAR JAHROMI
Signature of Individual Submitting:	
Date Submitted:	

For Completion in the Student Service Centre (SSC)

Received in the SSC by *(name in capitals):*			
1.1Method of Submission *(Handed in to SSC; posted through internal/external mail):*			
2.1*E-thesis Submitted (**mandatory for final theses)***			
Signature:		Date:	

TABLE OF CONTENTS

LISTS OF FIGURES

LISTS OF TABLES

LISTS OF ABBREVIATIONS

FSI	Fluid-Structure Interaction
ECM	Extracellular Matrix
GAG	Glycosaminoglycan
BPH	Benign Prostate Hyperplasia
H&E	Hematoxylin And Eosin
PCa	Prostate Cancer
FD	Fractal Dimension
ECF	Extracellular Fluid
KVFD	Kelvin-Voigt Fractional Derivative
RVE	Representative Volume Elements
EMT	Effective Medium Theory
FEM	Finite Element Method
SUBC	Static Uniform Boundary Conditions
KUBC	Kinematic Uniform Boundary Conditions
ROI	Region Of Interest
PBC	Periodic Boundary Condition
DRE	Digital Rectal Examination

CHAPTER 1

Introduction

Contents

1.1 Motivation

Although engineering is a subject with a thousands of years heritage, its applications in life science and medicine have seen radical developments in the last few decades, including genetic modification and synthetic biology, medical imaging techniques for diagnostic purposes and biomaterial science. These developments embrace elements of medicine, biology, chemistry, tissue engineering and materials science. Among those, the field of biomechanics has grown rapidly since the pioneering work of YC Fung and his co-workers, due to its potential to improve quality of life, in developing methods and theories to study the mechanics of molecules, cells, tissues, and organs. In parallel, recent advances in computational methods have brought innovative approaches to solving biomechanical problems, by increasing the capability of quantification and prediction when making sense of data acquired from experiments. Among the numerous areas where computational modelling has become an essential tool alongside experimental exploration, tissue mechanics is one that has seen balanced and parallel developments in both approaches. This is due to the complex nature of biological tissues, which have hierarchical and heterogeneous structures across a range of length scales, whose microstructures and functionality over different time scales, and which present different degrees of variation between samples from and between individuals. Modelling the mechanical behaviour of tissue has followed two distinct approaches; the first approach which is more traditional, considers the tissue as a structural material and predicts its behaviour of tissue by applying the principles of structural mechanics. The second approach, which is known as the mechanobiological approach, takes into account the microstructural and biological foundation of a tissue. In this approach, it is key to understand, quantitatively, the relationships between the tissue microstructures and its apparent properties, as well as their evolutions with respect to the various aspects of the biological environment.

When it comes to clinical applications, the challenge, however, is to investigate the least invasive and cheap method for early diagnosis of pathologies. biopsy remains a key indicator in diagnosis, but subjective, as the histological slides need to be interpreted by a pathologist, and the diagnostic outcome may involve a certain degree of uncertainty depending on the pathologist's experience [1]. Furthermore, biopsy involves sampling of suspect in vivo tissue and even though recent advances have been made in finding biopsy, remains a risk that diseased tissue has been missed. Although various palpation devices and methodologies have been proposed to measure the mechanical properties of soft tissue and so reduce the cost and invasiveness of diagnosis, the accuracy of these devices is still not high for some pathologies. The microstructural morphology of tissue can be affected by various pathophysiological conditions, e.g. by the presence of cancer, and such changes in tissue morphology could become useful indices for clinical diagnoses, such as for diseases of the liver, in the forms of fibrosis, carcinoma and cavernous hemangioma [2], and for various carcinomas in breast [3]. These microstructural changes often affect the mechanical properties of the tissue, and can be utilised by various diagnostic approaches. Palpation has been widely used for early diagnostic purposes in soft tissue where the practitioner looks for abnormalities such as changes in the texture or the existence of nodule. However, palpation is highly dependent on the experience of the doctor, which therefore decreases the reliability of the method.

This thesis specifically addresses a model system, human prostate, where distinguishing between healthy tissue, benign disease and cancer is particularly challenging. In most palpation devices, the viscoelastic nature of tissue has been neglected for the sake of simplicity. Viscoelasticity, however, could provide a more accurate outcome for tissue assessment due to its potential sensitivity to the very changes in tissue arrangement induced by pathophysiological conditions. This is beneficial to practitioners for making a better decision for treatment and also patients to be diagnosed accurately and have higher life expectancy.

1.2 Scope and structure

This thesis has two major goals. The first is to develop a framework for quantifying the microstructural changes in soft tissue subject to various pathophysiological conditions using prostate tissue as an exemplar system. This then leads us to the second goal of this thesis, which is to build a framework of characterizing the viscoelasticity of tissue arising from the movement of interstitial fluid, taking into account the tissue’s hierarchical nature. The ultimate impact of this work could be critical for early diagnostics of various pathologies, especially cancer, and to reduce the amount of invasive procedures such as biopsy. Notwithstanding the limitations, it is expected, in the long term, to increase the life expectancy of patients with instrumentation which exploits this framework in conjunction with a suitable palpation device in order to increase the accuracy of the method in performing the assessment in a cheaper way.

The objectives of this thesis are:

- to develop a computational framework, based on the tissue histology, to analyse the microstructural indices for the respective tissue types;
- to quantify the 3-way relationship between the tissue microstructural indices, their variations with respect to pathological condition, and the macroscopic mechanical properties;
- to develop a novel methodology for quantifying the viscoelasticity of soft tissue arising from the physical interaction between solid and fluid phases in the tissue microstructure;
- to apply the proposed methodology to histological samples of prostate tissue and investigate the influence of the microstructural changes in cancerous and non-cancerous tissues in such a multiphasic framework.

The thesis is organized to illustrate how each of these objectives are achieved, as follows:

Chapter 2: Multiscale modelling of multi-phasic soft tissue: state of the art

This chapter reviews a range of topics investigated in this thesis. Firstly, tissue morphology and its pathophysiological changes in prostate are reviewed. Secondly, mechanical properties of soft tissue is assessed, including elasticity and viscoelasticity, at various length scales, as well as methods for viscoelasticity characterization, both experimentally and computationally. Finally, the approaches which have been taken to deal with the heterogeneous nature of prostate tissue in the framework of fluid-structure interaction (FSI) and integrated to in numerical homogenization are discussed.

Chapter 3: Image processing and microstructural characterization of prostatic histology

This chapter deals with the establishment of the qualification framework based on histological images of prostate tissue. The framework categorizes three main pathologies (i.e. cancer, healthy and Benign Prostatic Hyperplasia (BPH)) based on proposed microstructural indices, such as acinus average size, acinus area fraction and fractal dimensions of the acinar structure. The proposed methodology is then correlated to Gleason scores for enhanced diagnosis.

Chapter 4: Multiscale mechano-morphological homogenization of prostate tissue

This chapter presents a complementary methodology to the previous chapter, in order to better understand the influence of apparent mechanical properties changes due to microstructural variations in the prostate tissue. A methodology for numerical homogenization to predict the apparent mechanical properties of cancerous, healthy and BPH tissue samples is presented. The influence of such pathologies on the apparent tissue elasticity is analysed and compared with the microstructural indices reported in the Chapter 3.

Chapter 5: Parametric study of simplified tissue structure – considering the biphasic nature of prostate tissue

In order to further investigate the influence of microstructural changes due to various pathophysiological conditions, a fluid-structure interaction (FSI) methodology is introduced. The influence of parameters such as strain rate, viscosity of the interstitial fluid, and microstructure on the mechanical properties of prostate tissue is explored. The focus is on how fluid movement within the microstructure influences viscoelastic behaviour. The FSI method proposed here servers as a key basis for further investigation of prostate histological models in the next chapter.

Chapter 6: Viscoelasticity in prostate tissue – fluid-structure interaction modelling

This chapter shows the application and feasibility of the framework presented in chapter 5 in the more realistic scenario of prostate diseases diagnosis. A computational framework that takes into account microstructural changes in prostate tissue is proposed. Samples which were extracted from histology images are used to implement stress-relaxation test for viscoelasticity characterisation. The effect of morphological changes in two sets of samples namely cancerous and non-cancerous samples, were assessed. Results show that the microstructural changes in those sample groups influence the viscoelastic response of tissue, largely affected by the fluid movement therein.

Chapter 7: Conclusions and a glimpse into the future

In this chapter, the work carried out in the thesis is summarized and the main conclusions are highlighted. Following this, the main areas of future work are suggested.

CHAPTER 2

Multiscale modelling of multiphasic soft tissue: state of the art

Contents

2.1 Summary

SECTION	OBJECTIVE
2.2 Tissue microstructure and histopathology	• Describe the hierarchy in soft tissue; • Review the changes in tissue microstructure subject to various pathophysiological conditions; • Describe the microstructure of prostate tissue; • Review the advantage of and limitations of image processing of tissue histology; • Review the state of art of microstructure-based methods used for tissue diagnosis;
2.3 Tissue mechanical properties and its components	• Review elasticity and viscoelasticity of soft tissue, particularly for prostate tissue; • Review various viscoelastic models.
2.4 Computational methods in soft tissue mechanics –multiscale and multiphysics	• Review the concept of homogenization and multiscale modelling. • Demonstrate the Fluid-structure Interaction method.
2.5 Motivation and objectives of this thesis	• Identify the objectives of the thesis

2.2 Tissue microstructure and histopathology

2.2.1 Biological tissue and its hierarchy

Biological tissues are hierarchical and heterogeneous, composite materials, consisting of cells and extracellular matrices built up into a variety of morphologies, and forming an important element of the human body. They often have a number of key structural features at a range of length scales, as shown in Fig. 2-1. Among various tissue types, soft tissue, widespread across the entire body, surrounds, connects and supports organs. It is classified into four major tissue types, all having different microscopic structural features, as shown in Fig. 2-2.

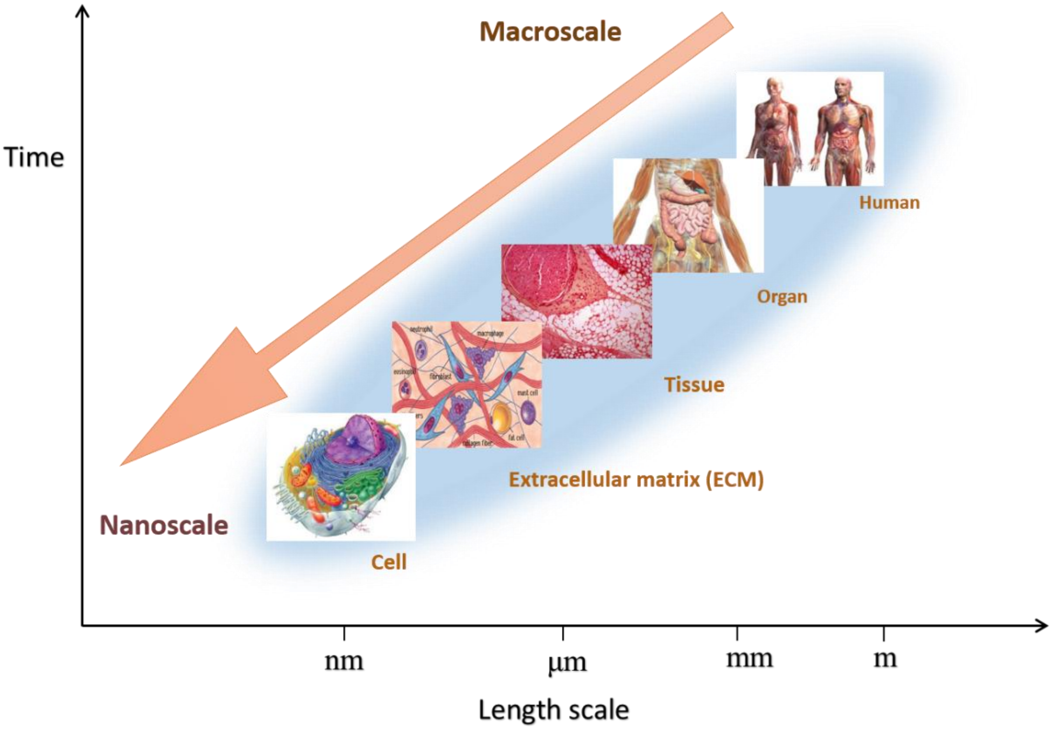

Figure 2-1. Hierarchical nature of biological tissues, from macroscale to microscale.

Firstly, epithelial cells are always attached to each other and arranged in a fashion of a single or multiple layers. They are often dense, with minimum intercellular space. This type of tissue usually covers the exterior of the body and outer surface of many internal organs i.e. body cavities and cardiovascular system; secondly, connective tissue forms and ‘fills’ the body organs and tissues including cartilage, tendons, ligaments, bone matrix, and the adipose (fatty) tissues as well as skin, blood, and lymph. It is composed of various types of cells and extracellular matrix (ECM) and contains a complex mixture of molecules including proteins such as collagen, elastin, laminin, fibronectin and polysaccharides such as glycosaminoglycan (GAG). Thirdly, muscle tissues are mostly responsible for movement in the body. This type of tissue is formed from aggregates of elongated muscle cells. There are three main types of muscle tissues, cardiac muscles help the heart to pump the blood, skeletal muscle is attached to bone and is responsible for mechanical movement and smooth muscles are often found in internal organs i.e. bladder, digestive tract and veins. Finally, the nervous system transfers information between various parts of body. Nerve tissue consists of nerve cells which receive and process the information with their dendrites form internal and external environment.

Prostate will be used as an exemplar tissue system for this thesis, and its histopathology and microscopic structural features will be discussed in detail in the following sections. Prostate is a glandular organ of the male reproductive system. It is normally in a size of a walnut in younger men and it may get larger in older men. It mainly consists of columnar glandular epithelial cells which are surrounded by connective tissue and muscle fibres.

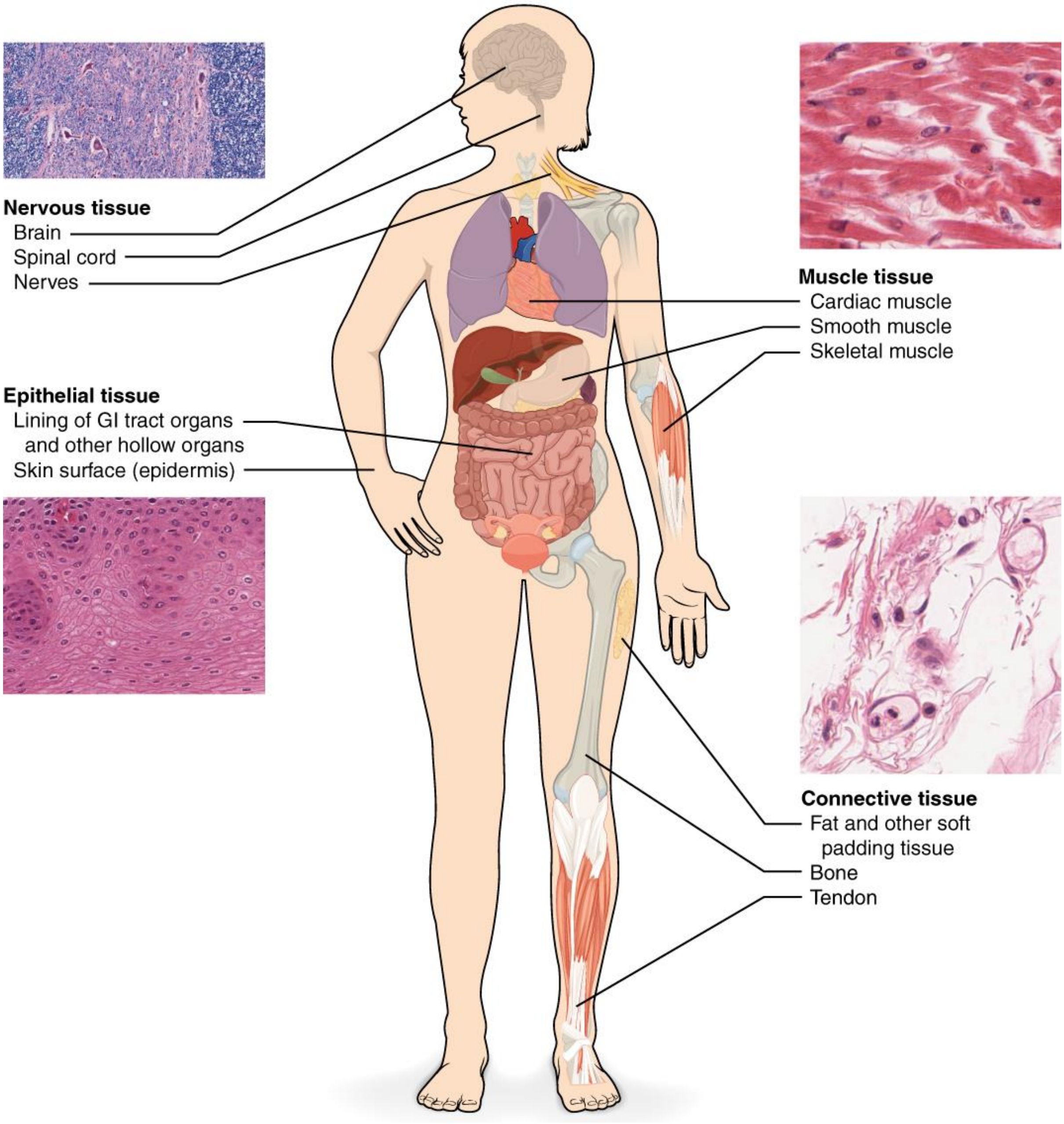

Figure 2-2. Illustration of the four types of tissue in the human body. The four types of tissue are exemplified in nervous tissue (with a magnification of ×872), stratified squamous epithelial tissue (× 282), cardiac muscle tissue (× 460), and connective tissue in the small intestine (× 800). [4]

2.2.2 Tissue histopathology

The microstructural morphology of tissue can be affected by various pathophysiological conditions, e.g. by the presence of cancer or benign prostate hyperplasia (BPH) in prostate. Such changes in tissue morphology are often revealed by histological analysis via microscopic means, which is then used by the pathologist for clinical diagnosis. Histology is the study of the microscopic anatomy of cells and tissues and to correlate their structure with function. Histological analysis is often performed by examining a thin slice (section) of tissue under a light (optical) or electron microscope. Its resolution depends on the methods used, ranging from ~1 µm for light microscopy to 80–100 nm for electron microscopy [5], [6]. In order to produce the histology slide, the tissue samples need to be 'fixed' by chemical or physical means, cut into thin tissue sections (~4 µm for light microscopy), and histochemically stained by a certain type of 'dyes' (e.g. Hematoxylin and eosin (H&E) [7], one of the most commonly used stains – blue on cell nucleus and pink on cytoplasm, therefore capable of rendering ideal contrast in observing tissue microstructures).

2.2.3 Human prostate

Prostate, as an exemplar tissue investigated in this thesis, consists of round to irregular branching prostatic glands and stromal tissue. Prostate glands take approximately half of the volume of the entire prostate, and are connected by long tubular structures which subsequently lead to the urethra. The fluid secreted by prostate contains various enzymes, zinc and citric acid and consists of approximately one-third of the total volume of semen. Different conditions such as prostatitis, Benign Prostatic Hyperplasia (BPH) and prostate cancer can affect the morphology of the prostate tissue. In prostatitis, which may result from bacterial infection, inflammation of prostate occurs due to the presence of neutrophils inside glands [8] and the number of inflammatory cells also increases in the prostate gland. In BPH the prostate enlarges due to the accumulation of dihydrotestosterone in the prostate, which triggers tissue growth. Most of the abnormal cell growth is promoted by glandular proliferation but an increase in stromal content can also occur. The gland size may vary in BPH, however, the gland size generally becomes larger and more noticeable [9]–[11]. Morphological changes, which also occur in Prostate cancer (PCa), often leading to smaller glands, have also been reported to influence the mechanical properties of prostate gland [12].

Prostate carcinoma is one of the most common cancers in men [13]. It is classified as a glandular cancer, often causing severe disruption to the tissue microstructure, manifested as a reshaped glandular pattern and microstructure. Such microstructural changes are often utilized in diagnostic methods, including histopathology, for soft tissue cancers following biopsies, using certain microstructural indices such as those used in Gleason grading system [14]. The Gleason system classifies prostate cancer into five grades represented by numbers ranging from 1 to 5, with 5 being the most aggressive case [15]. It utilises microstructural indices of the prostatic tissue, such as morphological patterns, shape and size of the glands. Gleason "score" is based on recognizing the "primary" and "secondary" grade and then summation of the two gives the overall assessment. Fig. 2-3 shows schematic examples of the five grades. In the Grade 1 the glands are uniform and round; Grade 2 shows more variable shapes than Grade 1 and the stromal content increases between glands; in Grade 3 the tissue consists of well-formed glands with porous architecture and round nests which may be distorted or compressed; Grade 4 shows poorly formed glands and complex papillary-cribriform islands; and Grade 5 shows solid masses with no clear formation of gland and infiltrating cords and single cells [14]–[16]. Increasing Gleason grade is generally associated with a reduction in the differentiation of the epithelial – lumen structure of the granular component of the microstructure and so it would seen that tissue texture analysis could be of essential aid for the identification of tissue composition in prostatic neoplasia, based on the histological micrograph of tissue samples using staining methods such as Hematoxylin and Eosin (H&E).

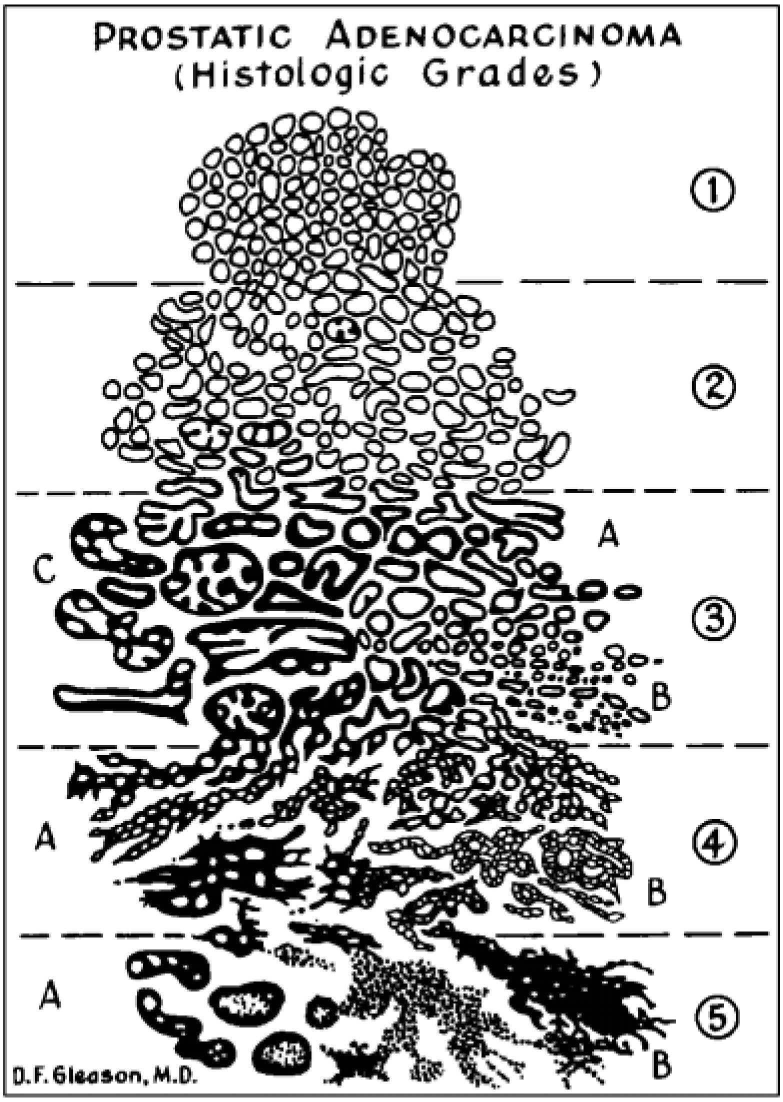

Figure 2-3. Schematic illustration of Gleason grade and the idea of scoring based on the microstructural changes. A, B and C are notations for different patterns [16].

2.2.4 Image Processing – Digital pathology

Image processing as has shown great potential an assistive tool in improving the effectiveness of clinical diagnostics, particularly in the area of digital pathology, using such methods as automated carcinoma detection and classification [17], in prostate [18],

[19], breast [20], [21] and lung [22] cancers. Image processing operates on the histological slides to enhance information and quantify the visual aspects of the tissue image. The first stage is to pre-process the image to remove the unwanted content (de-noise), and is followed by segmentation in which the image is divided into different sections. The morphological features (e.g. texture, colour intensity and etc.) of each section are then extracted for further characterization. Classification of the samples is the ultimate goal of image processing for digital pathology. For diagnostic purposes, tissue (or cell) samples are assigned and classified into cancerous, non-cancerous classifications and the level of malignancy may also be quantified.

Diamond et. al. [23] have shown the potential of quantitative classification of prostatic lesions by means of histological texture and processing the image patterns and morphologies. A number of indices have been used to describe the tissue microstructure, including morphometrically features such as boundary, shape (e.g. eccentricity, sphericity) [21], [24], [25], topological features based on Voronoi diagrams [18], [20], intensity of the colour and architectural and global texture features [18], [19]. A different approach which has recently received some attention is using fractal dimension (FD) to describe the texture of tissue. This method has been used to differentiate between benign and malignant cases of breast cancer mammograms [26], psoriatic lesions [27] and trabecular and cortical bone [28], [29]. Recent studies have shown that fractal geometry is useful in describing pathological structures of prostatic carcinoma [30]. Automated grading systems using fractal features and other types of image processing techniques have also been introduced for improved classification of the Gleason grading system [31].

2.2.5 Diagnosis

Diagnosis of soft tissues is a complex task due to inter-patient variability as well as variations with age, physiology and other factors such as the use of drugs (e.g. antibiotics and anti-inflammatories).

Palpation has been used to detect abnormality in tissue for centuries. It consists of touching the tissues, looking for lumps or changes in roughness that can be related to pathophysiological anomalies. The technique is still used nowadays due to its non-invasiveness and low cost, even though, it is subject to inter-practitioner variations. More importantly, the results are qualitative rather than quantitative. Novel devices such as those using instrumented palpation have been developed to address this problem, were being used in pre-clinical studies [12], [32] as illustrated in Fig. 2-4. Nevertheless, developments are still required to determine the mechanical properties based on the force feedback received and, more crucially, relate them to the underlying microstructures and ultimately to its pathological condition. The gold standard in soft tissue diagnosis is the biopsy where tissue samples are taken invasively, usually in an operating theatre, and later analysed under the microscope histopathologically. However, biopsies have certain disadvantages: they are invasive, expensive and not free from post-operation risks. Furthermore, it has been shown that some biopsies such as prostatic biopsies have a high rate of false positives and negatives [33]. Image based analysis such as MRI [34], [35], CT scans [36], [37], PET scans [38] and elastrography have the advantage of providing the useful information of the anatomy necessary to make appropriate diagnosis or surgery, however they are unfortunately not often used as a primary screening approach. Therefore, it is essential to develop methodologies to link the apparent mechanical behaviour of tissue (such as those derived from instrumented palpation) to its underlying pathological conditions, via an established quantitative structure-property relationship.

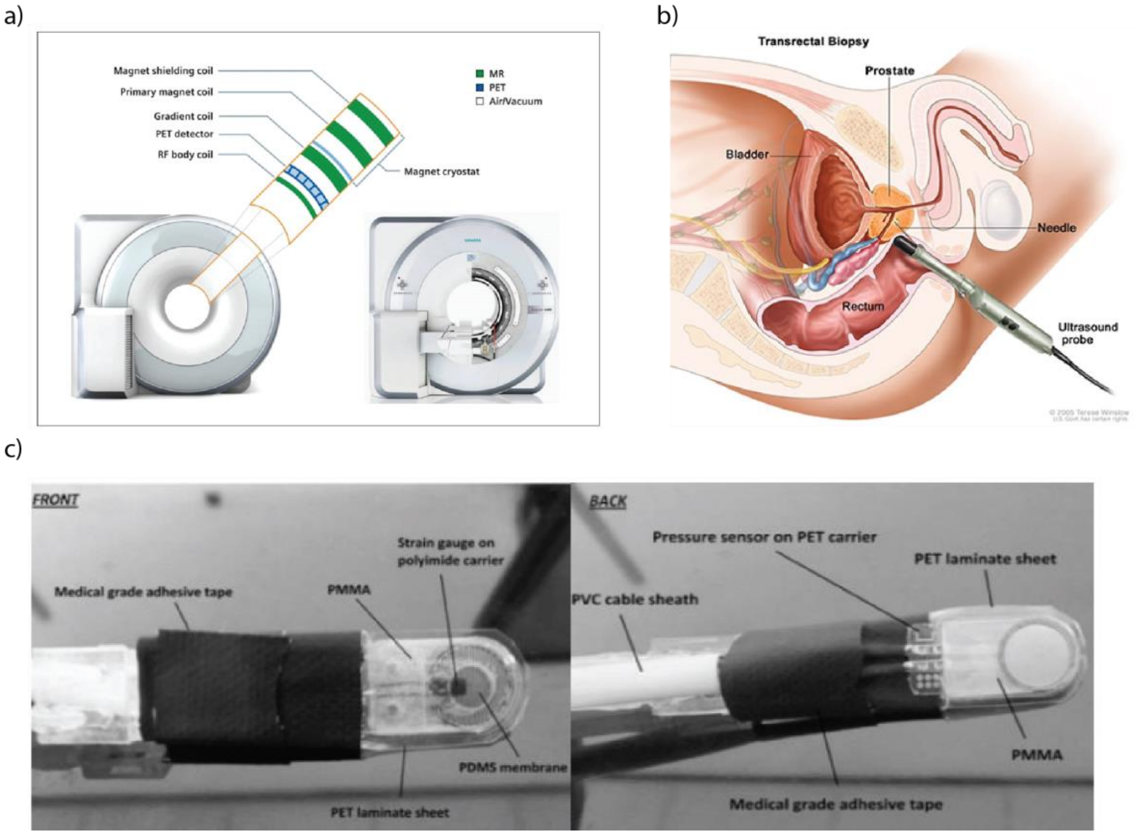

Figure 2-4. Examples of clinical diagnostic methods for prostate. a) Clinical applications of PET/MRI [38] b) Prostate biopsy with ultrasound probe [39] c) front/back view of probe device prototype for diagnosis with palpation [32]

2.3 Mechanics of soft tissues

Mechanical properties of soft tissue, like most engineering materials, are dependent on microstructure and are subject to the hierarchal nature discussed above. However, their mechanical properties, even at the same structural length scale, are well known to vary: (i) between samples from the same tissue type, namely intra-/inter-patient variabilities; (ii) between various tissue types; and, (iii) subject to development of disease or ageing. This, in addition to its well-known variations across a range of spatial scales, is illustrated in Fig. 2-5. For example, an increase of stiffness in large arteries has been reported due to ageing and among haemodialysis patients and type 2 diabetics [40]–[42]. Tissue stiffness (i.e. ECM stiffness) has also been reported to vary as a result of the progression of diseases and tissue homoeostasis [43]. Mueller et al. [44] proposed stiffness of liver tissue as a novel index to quantify the degree of liver disease, in order to better understand the mechanisms of liver fibrosis. In addition, elasticity of prostate tissue has been used as a qualitative biomarker for the detection and quantification of prostate cancer[45].

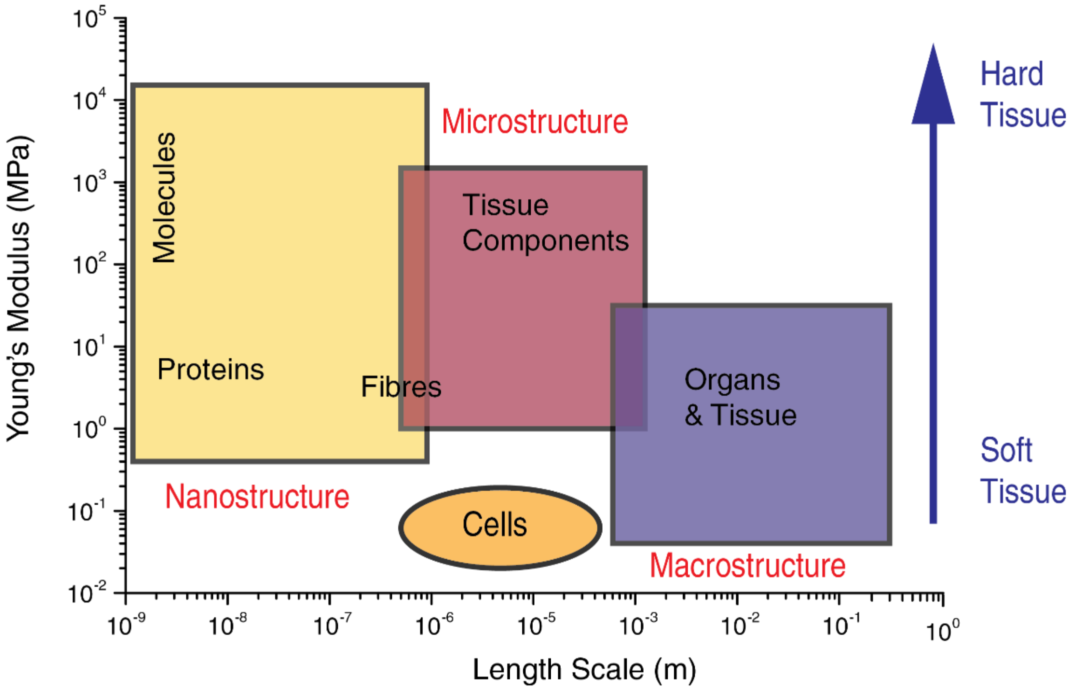

Figure 2-5. Mechanical properties (elastic modulus) of aorta, as an example, in different length scale from ECM level to organ level [42].

2.3.1 Elasticity

Soft tissues present complex mechanical behaviour. The Elastic part has been modelled with different constitutive equations such as neo-Hooken[46], Mooney-Rivlin [47] and Ogden [48]. The elastic behaviour of soft tissues has been studied in the literature, at both tissue scale and the microscopic cellular scales. Firstly, at the tissue scale, multiple studies have been carried out to analyse the elasticity of muscle [49], [50], whose behaviour can be modelled using a hyperelastic law [51]. Of particular interest is the work of Holzapfel and Gasser in the modelling of aortic tissue using a novel strain energy function that is capable of accounting for the inherent anisotropy of soft tissues due to the collagen fibres therein. In fact, their work has led to the Vascops software (i.e. vascular diagnostic software to provide patient specific risk assessment on vascular treatment based on imaging data) [52], [53] that is currently used in clinical practice. In addition, heart and mitral valve tissue have also been widely studied due to an increasing number of casualty caused by cardiovascular diseases. In particular Li et al. [54] has studied the anisotropic property of porcine aortic valve and its effects on its mechanical behaviour and the failure mechanisms. Furthermore, studies on breast tissue have shown that the stiffness of cancerous breast tissue is between 2.5 – 5 times, higher than healthy tissue [55] depending on the strain rate used. The mean elastic modulus of prostate tissue from the cancerous and noncancerous regions have been reported as 24.1 ± 14.5 and 17.0 ± 9.0 kPa [56], respectively.

At the cellular scale, on the other hand, variations of the mechanical properties of cells in both cancerous and BPH conditions in prostate have been reported measured using atomic force microscopy [57]. This study indicated that the cancerous cells are often softer, in contrast, to the macroscale where the tissue is stiffer in the cancerous regions which could be due to higher cell density and higher content of stromal tissue. For tendons, the large strain behaviour of tendons has been analysed by Shearer [58], who developed a strain energy density function that links the mechanical behaviour at large scale with the underlying fibres and their intrinsic properties (e.g. length, crimp length, diameter of the fibres).

2.3.2 Viscoelasticity in soft tissue

2.3.2.1 Origin of viscoelasticity

The main focus of this thesis is to investigate the influence of fluid filled in tissue on its apparent viscoelasticity. This would offer a model which is able to mimic the viscoelasticity of tissue given rise by the hierarchical and biphasic nature of soft tissue, and will form the basis of this thesis. Viscoelasticity in soft tissue has been traditionally believed to arise from the shear interaction of collagen fibrils within the matrix of proteoglycans, in which the matrix provides viscous lubrication between collagen fibrils [59], [60]. This model is alien to the theory of viscoelasticity in polymers where the shear interaction is conditioned by crosslinking and van der waals forces between them .Collagen fibres have been suggested to exhibit progressive decreases in stiffness with ageing, due to breakage of interfibrillar bonds or, on the contrary, irreversible un-crimping of collagen fibres leading to increase in the tissue stiffness of tissue [61]. However, the origin of viscoelasticity in biological tissues is still unclear [62], [63]. Many researchers investigated that redistribution of interstitial fluid is involved in the viscoelastic (i.e. stress relaxation/creep) behaviour of soft biological tissue [64], [65]. Haslach et al.[66] investigated the role of the extracellular fluid (ECF) in the dynamic mechanical response of rat brain tissue, where the behaviour of ECF can be influenced by the interaction of compression and translational shear due to hydrostatic pressure which supports stress. Parker [67], [68] has proposed a cubical model with an internal fluid micro-channel which represents an idealized tissue block subjected to uniaxial loading.

2.3.2.2 Continuum mechanics approach for tissue viscoelasticity

Viscoelastic materials exhibit both elastic and time dependent (i.e. viscous) behaviour in tension and compression. Unlike elastic materials, stress can relax over time, e.g. under constant strain in viscoelastic materials. Creep (i.e. deformation changes with time under constant stress), stress relaxation (i.e. varied stress under constant deformation), and dynamic (e.g. deformation changes under sinusoidal loading) are commonly used for mechanical characterization of viscoelastic materials, as illustrated in Fig. 2-6.

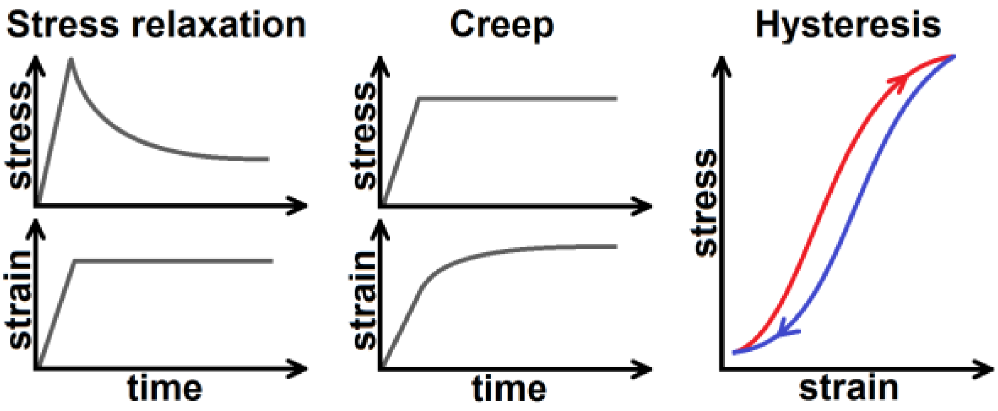

Figure 2-6. Common methods for viscoelastic characterization.

Maxwell and Kelvin-Voigt models are often used, as shown in Fig 2-7 for characterizing viscoelasticity, use elastic springs and viscous dashpots, connected sequentially (i.e. Maxwell) or in parallel (i.e. Kelvin-Voigt), to represent time dependent behaviour of a viscoelastic system. However these models, Maxwell and Kelvin-Voigt, are only accurate to model stress-relaxation and creep individually.

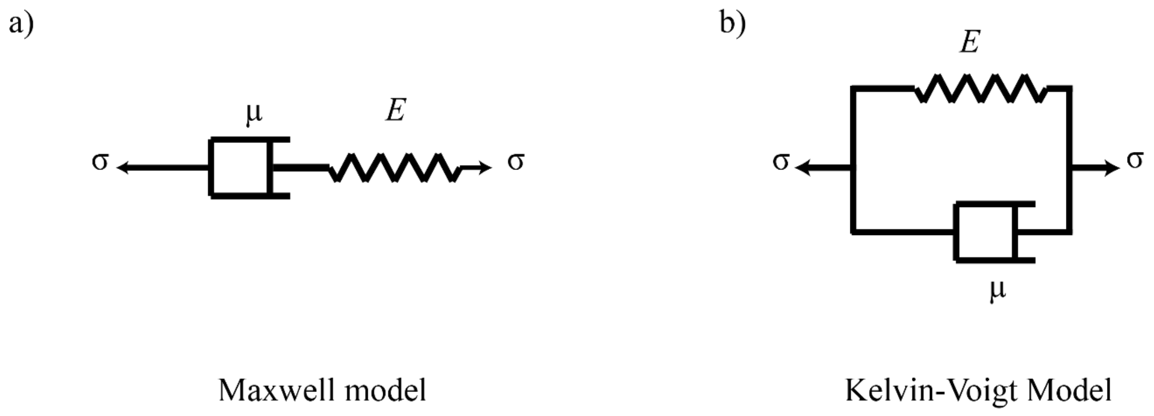

Figure 2-7. Schematic of Maxwell model (a) and Kelvin-Voigt model (b), as examples of phenomenological models often used to characterize material viscoelasticity. μ is viscosity of damper and E is stiffness of spring

The equations below represent the Maxwell and Kelvin-Voigt models, respectively, when σ is applied stress. For a Maxwell model, equilibrium gives,

$$\sigma = \sigma_s = \sigma_d \tag{2-1}$$

where σ is the applied stress, σ_s is the stress in the spring and σ_d is the stress in the damper. The kinematic condition is,

$$\varepsilon = \varepsilon_s + \varepsilon_d \tag{2-2}$$

where ε is the total strain in the Maxwell element, ε_d is the strain in the damper and ε_s is the strain in the spring

$$\sigma = \sigma_s = E \cdot \varepsilon_s \tag{2-3}$$

$$\sigma = \sigma_d = \mu \cdot \dot{\varepsilon}_d \tag{2-4}$$

Differentiating Eq. (2-2) and replacing the strain rates of the spring and damper using Eqs. (2-3) and (2-4) gives after rearrangement

$$\dot{\sigma} + \frac{E}{\mu}\sigma = E\dot{\varepsilon} \tag{2-5}$$

To obtain the solution of Eq. (2-5) for the case of creep note the applied stress is constant and can be written as

$$\sigma(t) = \sigma_0 . \mathrm{H}(t) \tag{2-6}$$

where H(t) is the unit step function (otherwise known as Heaviside function) and is defined as

$$\begin{aligned} \mathrm{H}(t) &= 1 \quad \text{for t > 0} \\ \mathrm{H}(t) &= 0 \quad \text{for t < 0} \end{aligned} \tag{2-7}$$

In other words the stress is constant for time greater than zero. With this input the solution of Eq. (2-5) is

$$\varepsilon(t) = \sigma_0 \left(\frac{1}{\mathrm{E}} + \frac{t}{\mu}\right) \tag{2-8}$$

the solution of Eq. (2-5) for relaxation is obtained using a step input in strain,

$$\varepsilon(t) = \varepsilon_0 . \mathrm{H}(t) \tag{2-9}$$

With the resulting stress output of

$$\sigma(t) = \varepsilon_0 . \mathrm{E}e^{-t/\tau} \tag{2-10}$$

where E is the spring constant and $\tau=\mu/\mathrm{E}$ is the relaxation time.

For the Kelvin-Voigt model the equilibrium equation and the kinematic condition are,

$$\sigma = \sigma_s + \sigma_d \tag{2-11}$$

$$\varepsilon = \varepsilon_s = \varepsilon_d \tag{2-12}$$

Under the creep loading the solutions becomes

$$\varepsilon(t) = \frac{\sigma_0}{\mathrm{E}}(1 - e^{-t/\tau}) \tag{2-13}$$

A more realistic mathematical model can be developed by considering series of Maxwell elements in parallel, a model with many elements called a Generalized Maxwell Model as shown below in Fig. 2-8,

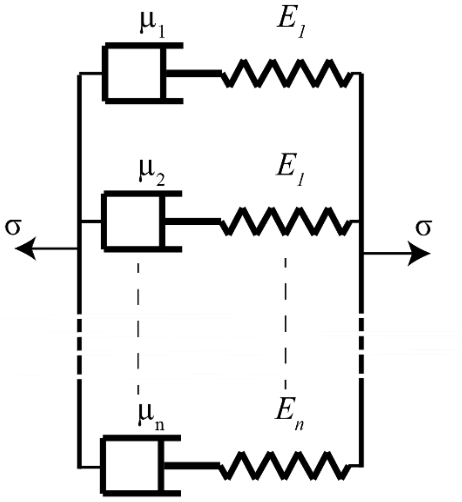

Figure 2-8. Schematic of Generalized Maxwell Model

The solution of Generalized Maxwell model for given strain input, ε(t), can be found by superposition of n first order differential equation solutions or by solution of the single n^th order differential equation.

$$\sigma_i + \tau_i \mathrm{D}\sigma_i = \mu_i \mathrm{D}\varepsilon_i(t) \tag{2-14}$$

where i ranges from 1 to n. The kinematic constraint again assumes that the strain in each element is the same as the global strain, $\varepsilon_i(t) = \varepsilon(t)$. And the equilibrium constraint assumes that the solution for the global stress is simply a sum of the individual stresses, $\sigma(t) = \sigma_1(t) + \sigma_2(t) + \ldots + \sigma_n(t)$. For the condition of stress relaxation, $\varepsilon(t) = \varepsilon_0 H(t)$, the solution of these linear differential equations can again easily be found by superposition

$$\sigma(t) = \varepsilon_0 \sum_{i=1}^{n} E_i \, e^{-\frac{t}{\tau_i}} \tag{2-15}$$

This type of representation is sometimes called Prony series [69] and such an exponential expansion is often used to describe the relaxation modulus of a viscoelastic material even without reference to a mechanical model. The method of Prony series is often used to fit the results from stress relaxation or creep tests, with a number of decay functions. This method is simple and provides a good insight in the relationship between modulus and relaxation times. It has been used for characterizing different tissue types, including viscoelasticity in prostatic tissue where the time constants have been used as a quantitative assessment index for tissue quality [70]. Also the time-dependent behaviour of aortic valve tissue has investigated under various strain and loading conditions, in both circumferential and radial directions using Prony series [71]. Kelvin-Voigt fractional derivative (KVFD) [72], [73] is also capable of characterizing stress-relaxation and creep behaviour simultaneously. The KVFD model is a generalization of the Kelvin-Voight model where the stress in the dashpot is equal to the first derivative with respect to time of the strain. In the KVFD model the stress in the dashpot is equal to the fractional derivative of order α of the strain[74]. The KVFD has been proposed to investigate the frequency-dependent viscoelastic material properties of liver tissue [75], [76].

More sophisticated models such as a recruitment model (i.e. power law) extend the idea of using spring and dashpot for specific applications (e.g. modelling of lung tissue) by introducing sequential series of Maxwell elements [77]. This model, which works well in the case of lung tissue, involves recruitment at two different levels, one being at the level of the elastic elements within each relaxation unit and the other being at the fibre–fibre level (i.e. stiffening in lung parenchyma) [78].

For dynamic measurements, on the other hand, cyclic loading is often applied to the tissue sample, usually in the form of sinusoidal deformation and the phase lag between stress and strain is analysed to characterize the viscoelasticity of the material. In such tests, different techniques can be used to identify the corresponding transfer functions related to the stress and strain in Laplace space [79]–[81]. Both quasi-static and dynamic tests can measure the characteristics of the material therefore these tests should be selected based on the individual applications. Among them, Prony series has shown great feasibility and been widely used to fit experimental data (mostly in the forms of creep or stress relaxation) of various materials such as polymers [82], silicon [83] and biological tissues including blood vessels [84], prostate [70], ligament [85] and brain [86].

One of the aims of viscoelastic characterization is to obtain the time constants or phases lag which describe the behaviour of the material. However, there are some limitations for such models for such purposes the method of Prony series is used to model of linear viscoelasticity and, on its own, is not capable of modelling nonlinear behaviours. Unsatisfactory curve fitting of experimental data has also been observed [87] when Prony series is used. There is still ambiguity about the number of fitting parameters in using Prony series - using a large number of fitting parameters may sometimes lead to more accurate fitting, but the model could become unnecessarily complicated and it will be difficult to provide clear physical interpretation of what the derived parameters mean.

Therefore, it is critical to find the balance between the fitting error and the number of parameters used, and this will be explored in this thesis in the context of viscoelastic characterisation of prostate tissue.

2.3.2.3 Other approaches of viscoelasticity characterization

Holzapfel and co-workers [88]–[90] have proposed a series of viscoelastic models which characterise the viscoelasticity in soft tissues related to the constituents of tissue hierarchy, such as the arterial wall, based on postulating a particular anisotropic fibre-reinforced strain energy density function. Strain hardening or softening may appear in viscoelastic materials especially biomaterials and elastomers, and viscoelastic models have been proposed to predict the behaviour of vascular tissue including softening due to damage [91]. Gasser et al. [92] emphasized the influence of material anisotropy on viscoelasticity and proposed a framework for viscoelasticity application with finite strain to muscular tissue in heart. Bergström and Boyce presented a model to predict time dependent behaviour of soft tissues under cyclical loading, and their model decomposes the stress-strain behaviour into contributions of micro mechanics of macromolecular networks (i.e. fibre network in tissue) [93], [94]. Screen [95] has shown that sliding between collagen fibers contribute to the viscoelastic behaviour of tendon fascicles, by testing viscoelasticity and stress relaxation in tendon fascicles under the confocal microscope and comparing this with the tissue responses at the macroscopic level. Poroelasticity and poro-viscoelasticity have also been used to model the mechanical behaviour of biphasic tissues such as cartilage [96], [97], tendon [98] and liver [99]. In these studies, it was found that the interstitial fluid pressure has a significant influence in the apparent mechanical properties of the tissue.

2.3.2.4 Tissue heterogeneity and multiphasic and multiphysical nature – a potential source of viscoelasticity

Most soft tissues such as skin, breast and prostate are materials with a high degree of heterogeneity and complex underlying microstructure, as illustrated in Fig. 2-8. more importantly they are also multiphasic with components such as cells and elastic fibres that are often described using the laws of solid mechanics [100], [101], but incorporating fluidic components. These fluidic components can operate at a range of scales, from the interstitial fluid that is in constant exchange with the vascular network [102] as well as larger fluid-filled components such as glands, and larger blood and lymph vessels. The interaction between the solid and fluid phases within such heterogeneous and multiphasic materials, alongside the intrinsic properties of the constituents, contributes as a whole to the apparent properties of tissue. However, a quantitative structure-property relationship, i.e. how the mechanical interaction between the solid and fluid components in the heterogeneous microstructure of tissue affects its apparent properties, is still unclear.

Viscoelasticity, as an apparent mechanical property of tissue affected by microstructural changes, has been proposed for the diagnosis of pathological conditions in such tissues as prostate cancer [103], liver tumors [104], breast cancer [105], [106] and is based on metabolic activity or cyclic loading in tendons [107]. In prostate tissue, for example, acinus in malignant tissue usually has irregular geometries and is found scattered in stroma as clusters or isolated, becoming less recognizable compared to those in healthy tissue [108], [109]. Such changes in tissue morphology could subsequently lead to a change in the mechanical properties at the macroscopic level [12], which can be used in clinical diagnosis such as instrumented digital rectal examination [110] and elastography [111], [112]. It is therefore critical to understand how morphological change in tissue subject to certain pathological conditions manifests itself in its apparent viscoelasticity, in particular taking into account the heterogeneous and multiphasic nature of the tissue microstructure.

The influence of the movement of interstitial fluid a the mechanical behaviour of tissue, such as in cartilage [64], [113], brain tissue of rats [114] and the micromechanics of tissue growth [115], [116], has been reported in the literature. Methods based on a continuum mechanics approach such as poroelasticity have been proposed to model the fluid flow in porous media [117], cartilage [118] and soft tissue [96]. Although successful in modelling the behaviour of the fluid flow at the apparent continuum scale, such a continuum approach is incapable of accounting for the tissue heterogeneity arise from its underlying microstructure. More recently, Parker and co-workers [67], [119] have proposed a series of mathematical models that take into account the biphasic nature of tissue, including the flow of interstitial fluid in the tissue, subject to stress relaxation. Nevertheless, the critical role of the physical mechanism of the multiphasic and multiphysical interaction in the apparent tissue viscoelasticity is still unclear, particularly when it is affected by the tissue microstructure that may evolve with certain pathologies.

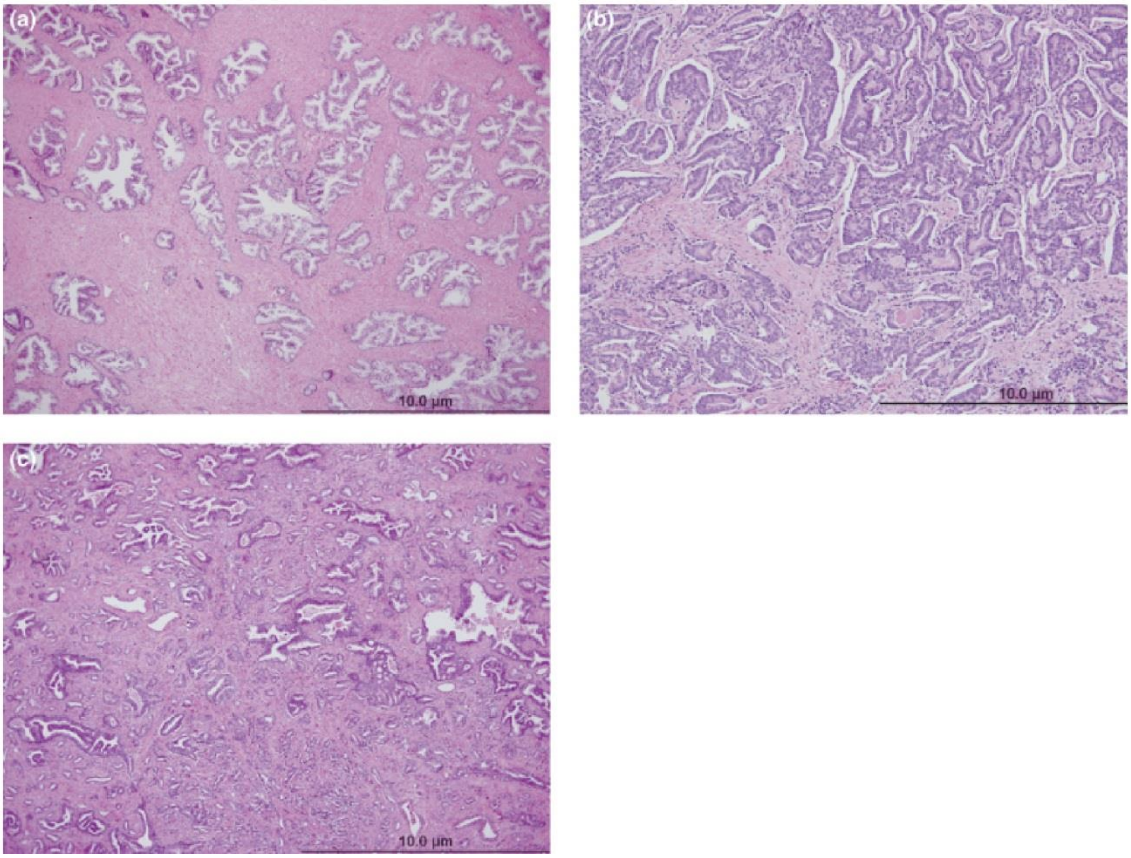

Figure 2-8. Histology images of prostate samples, where the complexity of tissue microstructure is illustrated. a) a healthy tissue sample b) a sample with 70% cancer and c) a sample with 100% cancer [120].

2.4 Histology-based computational methods–multiscale and multiphysics

2.4.1 Multiscale modelling – homogenization method

It is well-known that almost all engineering materials and biological tissues are heterogeneous to some extent. Heterogeneity in materials, covers a broad scope but is often defined as non-uniform distribution of components and their properties. Materials with heterogeneity often exhibit complex mechanical behaviour, as a result of such 'non-uniform distribution' of their material properties, at both macroscopic and microscopic scales. In general, there are two principles applied in modelling heterogeneous materials and their mechanical behaviour. The first is to utilize continuum approaches where the heterogeneous material is represented by an homogeneous one that presents equivalent behaviour, often at a higher length scale [121]. This approach is often adopted when the mechanical behaviour at the underlying length scale (i.e. microscopic) is not of particular interest. The second approach is based on micromechanical principles, accounting for the underlying microstructure of the material and its heterogeneity [122] so the detailed mechanical behaviour at the microscopic scale is modelled. The combination of the two, i.e. starting off from the microscopic scale to derive the constitutive laws in order to understand the resulting macroscopic behaviours, is often referred to as ‘multiscale modelling’, which may involve more than two scales with additional meso-scales in between.

The microstructure of heterogeneous materials (for the sake of simplicity, only two materials are considered) can be observed in two phases, including the material which forms the continuous base and often referred to as a *matrix*, and the other material which is often discretely embedded in the matrix and often referred to as an *inclusion*. The process of finding the ‘apparent’ behaviour of such heterogeneous material is therefore called ‘homogenization’. This approach, originally developed mainly as a group of mathematical methods for multiscale problems, has become popular in solving practical engineering problems especially in materials with periodically-distributed microstructures such as fiber- reinforcement composites [123].

Among the many homogenization methods as discussed above, two types of implementation are particularly popular, namely analytical and numerical. Firstly, analytical homogenization methods, taking asymptotic homogenization as an example, often assume that a composite is assembled from representative volume elements (RVEs) which are repeated periodically. On the other hand, numerical homogenization, e.g.

methods based on the finite element method (FEM), is a well-known approach which was developed to evaluate the effective mechanical properties of various composite materials with periodic microstructure in the 1960s [124], [125]. Therefore, the characteristic of the composite as a whole is assumed to be the same as the characteristic of the RVE, as long as there is a distinct difference between the two length scales [126], as illustrated in Fig. 2-9.

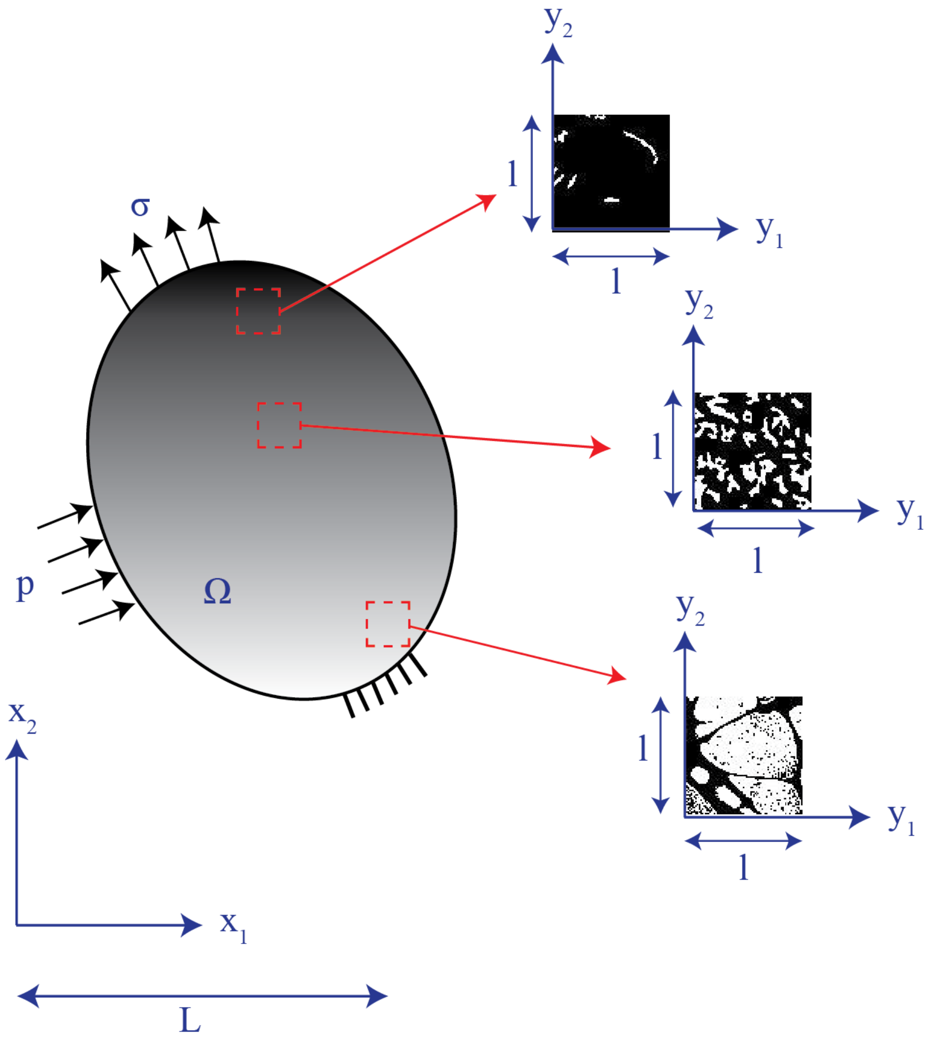

Figure 2-9. Schematic illustration of homogenization of hierarchical, multiscale structures by choosing an RVE. The three microstructures are representative ones from prostate histology.

A number of analytical approaches have been described in the literature [127]. The Parallel and Series models, known as Voigt [128] and Reuss [129] models, are the simplest ones that can be used to characterise biphasic systems. These models are often used as benchmarks for validation of new models since they offer upper and lower bounds of effective properties of biphasic materials. The effective medium theory (EMT) model [130] is based on the assumption that the materials have a completely random distribution of all constituents, and provides a qualitative trend of effective properties which represent the whole material. Some other models have also been proposed, based on combination of basic models, for more complex structures or forming a network of simple parallel and series models [131][132].

Alternatively, Hashin and Shtrikman [133] have derived theoretical material bounds for the apparent properties for biphasic systems, which are available for elastic problems [134], based on presumed quasi-homogeneity and macroscopic isotropy of the materials, but without accounting for the geometries/topologies of the inclusions. Friedman used analytical approaches to predict the effective conductivity of unsaturated porous media [135]. Other models have been proposed to derive the effective property based on the volume fractions of the multiple phases and their mechanical properties, often fitting the experimental data or expanding from the existing models such as Maxwell-De Loor [136] and Friedman models [137]. Although many analytical models have been introduced to predict the effective properties of complex structures, there are still some limitations: firstly, most of those theoretical models introduce factors with no physical meanings, such as experimental parameters; secondly, most models become over-simplified, making them incapable of modelling complex physical phenomena (e.g. nonlinear problems and fluid flow); thirdly, most are incapable of dealing with heterogeneous materials with more than two phases.

Numerical homogenization has been used to predict the effective material properties of both compressible and incompressible composite materials with small or large strain [138] and also for nonlinear materials (e.g. viscoelastic) [139]. Different boundary conditions have been proposed for the purpose of numerical homogenization. For example, static uniform boundary conditions (SUBCs) consist of imposing a set of stress fields, and kinematic uniform boundary conditions (KUBCs) consist of a set of prescribed displacement fields, at the boundaries of the chosen region of interest (ROI). Applying such boundary conditions often results in an upper bound for the effective mechanical properties in the case of KUBCs which is recognized to be an over estimate and a lower bound on the effective mechanical properties in the case of SUBC [140]. In addition, a periodic boundary condition (PBC) can be used when there is an RVE that can be considered as ‘representative’, i.e. when there is a distinct difference between length scales and the material indeed has a periodic microstructure [141]. A PBC does not always give a robust solution, especially when the material cannot be considered to have periodic microstructure. To tackle this issue, Han and Wriggers [142] proposed a so-called window method in which the ROI is surrounded by a frame of homogenous material. This method was later developed where the frame material was iteratively optimised until it matches the macroscopic response obtained [143], [144], thus making the frame have a the equivalent apparent properties of the heterogeneous system. Other methods, such as the moving window method [145] can also improve the feasibility of numerical homogenization when tackling materials with non-periodic structures, where the sensitivity of the location and size of the chosen ROI is analysed in order to give a more detailed picture of the degree of heterogeneity of the macroscopic material.

2.4.2 Multiphysical modelling in tissue – Fluid-Structure Interaction

Multiphysical systems involve multiple physical phenomena that may affect each other, such as electromagnetics [146], solidification [147] and Fluid-Structure Interaction (FSI). The tissue is multiphasic, consisting of interstitial fluid and ‘solid’ tissue phase. In this regards, analysis of fluid-structure interaction becomes an ideal candidate, by which the interaction between the tissue solid and fluid phases can be modelled in the context of complex tissue microstructures. It is a multiphysical modelling technique and is often applied to complex systems in which interaction between a deformable structure and fluid flow is of interest, with a wide range of applications in engineering and biomechanics [148]–[150]. One major application of FSI is in the modelling of the cardiovascular system, where ‘solid’ tissue constantly mechanically interacts with blood flow. FSI has been used to simulate the behaviour of postulated flow through a flexible channel [151] as well as interaction of blood flow with the vessel walls which provides better understanding of blood flow dynamics and circulatory system [152]. At the organ scale, a realistic heart model has been used to predict the elastic behaviour of the mitral valve using a dynamic FSI modelling technique [153], [154]. Furthermore, Malve et al. [149], [155] have also shown the potential of FSI over standard CFD modelling by comparing the flow patterns through the airways in trachea and main bronchi, in order to explain possible mechanisms in respiratory mechanics. The influence of blood flow in causing atherosclerotic plaques to rupture in stenotic arteries has been studied using FSI simulation of lipid plaque [156], [157]. Another advantage of FSI in this field is that, because it is based on physical modelling and able to account for geometries and topologies from medical imaging, it is often used as a tool to investigate the influence of patient specific features. Wu et al. [158] recently used FSI for transcatheter valve replacement in both a patient specific scenario and an in vitro test to estimate the feasibility of the FSI model. Abdominal Aortic Aneurysm rupture risk has also been studied using FSI modelling. With this methodology Xenos et al. [159] could predict the potential position of the rupture. Birmingham et al. [160] developed an FSI framework for bone and marrow tissue to capture the influence of mechanobiological variations in the marrow such as its viscosity on the overall mechanical response of bone.

In summary, FSI has been used in biomechanics to take into account the interaction between the fluid and solid phases, but mostly in cardiovascular scenarios where the interaction occurs between tissue and the blood stream. There is little existing work on using such technique in tissue microstructure (i.e. between solid tissue phase and extracellular fluid), and this thesis will attempt to explore the complex mechanical behaviour of soft tissue by taking into account its multiphasic and multiphysical nature.

2.5 Bridging the gaps

Based on the motivations and objectives of this thesis mentioned above, the following topics will be studied in the succeeding chapters:

- Morphological changes often occur in tissue as a result of various pathophysiological conditions. Considering tissue as a hierarchical composite material, it is important to understand the influence of these microstructural changes on mechanical properties of the tissue at different length scales. To provide and appropriate analytical framework, it is critical to analyse tissue microstructure and find the correlation between microstructural changes and their mechanical properties which can provide better understanding of tissue quality for diagnostic purposes.
- Soft tissues are multiphasic, consisting of hierarchical and heterogeneous microstructures. It is therefore important to establish a quantitative structure-property relationship, taking into account its multiphasic and multiphysical microstructures.

By doing this, it is possible to further understand why soft tissue behaves in a specific mechanical way (e.g. viscoelasticity), and the multiphasic and extent to which is multiphysical nature influences properties, in addition to the established contribution to viscoelasticity due to the intrinsic properties of the tissue components.

- It is crucial to correlate the apparent mechanical properties of tissue with respect to the variations in tissue microstructures, which can be caused by certain pathologies. This could lead to an enhanced understanding in applications such as cancer diagnosis in prostate, where the viscoelastic properties have already been used as key indices in such diagnostic protocols as magnetic resonance elastography [161], ultrasound elastography [162] and instrumented palpation [70]. A deeper understanding of the relationship between the structure and its mechanical response could also complement and enhance the diagnostic power of imaging modalities; for example ‘restricted diffusion’ on Diffusion Weighted Imaging of an MRI scan is one of the parameters used to assess whether cancer is present or absent. It is likely that water “diffusion” is being restricted on MRI as the glandular spaces become more compressed by cancer cell growth.

CHAPTER 3

Image processing and microstructural characterization of prostatic histology

Contents

3.1 Summary

Prostate cancer is one of the most common cancer in men[13], often in forms of poorly differentiated carcinoma, presenting irregular acinar shape and size and less recognizable gland pattern in tissue morphology, causing severe disruption to the tissue microstructure and functionality. Such microstructural changes are often revealed by microscopic histology on tissue samples obtained from biopsies and subsequently utilized to study the manifestations of disease using such methods as Gleason grading system [14]. The Gleason grading system uses the morphological indices, as mentioned above, to help stage the cancer and evaluate the prognosis. However, it is a subjective procedure as the histological slides need to be interpreted by a pathologist, and the diagnostic outcome may involve a certain degree of uncertainty relying on the pathologist's experience which negatively influences patient care[1]. For example, disagreement among uropathologists interpretation of Gleason score for some cases (e.g. low grade tumours, tumours defined with small cribriform structures and tumours in the border areas between the classic Gleason patterns) has been reported[163]. Therefore computational methods such as image processing may be of importance to assisting pathologists in processing the histological information, by reducing the subjectivity and increasing the efficiency of the clinical diagnostics of cancer[164].

Although automated grading system by use of those microstructural indices have been employed for tissue histopathological assessment, e.g. for better classification of Gleason grade system[31], this chapter aims to take this to the next level, by not only quantifying the sensitivity and effectiveness of a range of tissue microstructural indices such as area fraction and fractal dimension for samples in healthy, BPH and cancerous conditions. This chapter is structured as follow: first the image processing and sample preparation are discussed; then the methodologies and indices are introduced; finally, the results are shown and discussed. The result of this chapter, i.e. the morphological indices, will be attempted to link to the elasticity of the tissue samples in the next chapter, for the purpose of prostate cancer diagnosis.

3.2 Image processing and analysis of prostate histology

Prostate tissue obtained from a patient who was diagnosed with an acinar adenocarcinoma with a Gleason score of 4+3 (i.e. as described in page 13, most of the tumour is grade 4 and less is grade 3, and they are added for a Gleason score of 7) is selected in this study. Fig. 3-1(a) shows the histological image of the tissue sample stained with H&E and three regions, i.e. malignant, benign prostatic hyperplasia (BPH) and benign, marked and classified by the pathologist. The image was converted into binary, as shown in Figs. 3-1(b-d) using a grayscale range of 0-142 (where 0 denotes black and 255 white) to identify regions containing acinar fluid (white in both cases) in tissue histology and 143-255 for those of ‘solid’ tissue phase consisting of branches of glands and stromal tissue (pink in H&E; black in the binary images)

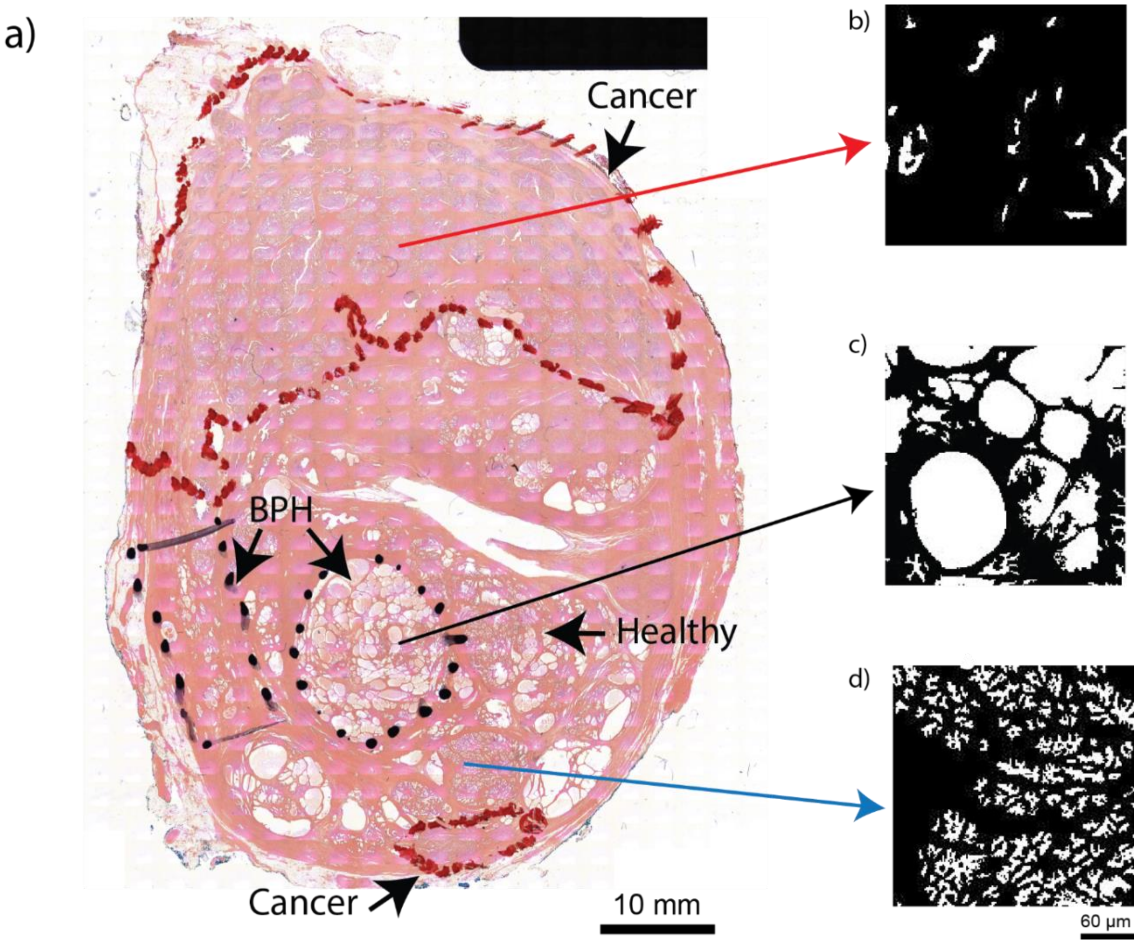

Figure 3-1. Histology of a prostate sample. (a) Prostate histology image stained with H&E contain three different zones namely: cancer (marked with red), BPH (marked with black) and healthy tissue. Microstructures of cancer (b), BPH (c) and healthy (d) samples are shown in regions of interest (ROIs) of 2.14mm.

As shown in Fig. 3-1, in order to investigate the heterogeneity and sensitivity (to the size of chosen sample) of tissue morphological indices, the entire histology image is divided into regions of interest (ROIs) using a range of sizes, i.e. 0.54 mm (40 × 40 pixels), 1.07 mm (80 × 80 pixels) and, 2.14 mm (160 × 160 pixels). It should be noted that the ROIs that contains the background of the histological image, i.e. those with the background colour of the histology slide, were discarded. A summary of ROI selections used in the study is shown in Table 3-1.

Table 3-1. Summary of the number of samples and sizes considered throughout the study.

ROI size	**0.54 mm (40 × 40 pixels)**			**1.07 mm (80 × 80 pixels)**			**2.14 mm (160 × 160 pixels)**		
	Healthy	**Cancer**	**BPH**	**Healthy**	**Cancer**	**BPH**	**Healthy**	**Cancer**	**BPH**
Number of ROIs	286	1042	485	87	421	149	31	139	49

3.3 Morphological characterization

Four microstructural indices, namely, average size of acinus (*A*), area fraction of acinus (*ρ*), fractal dimension (*FD*) and lacunarity (*L*) are analysed for all ROIs, and their definitions are given below.

3.4 Size and area fraction of acinus

Acinus, the smallest structural component of the prostate gland, contains fluid secreted and lined by secretory epithelial cells. Morphological changes of acini, such as their size and fraction, are therefore of critical importance. Mean size of acinus (*A*) is calculated by taking the average value of the acini areas in each ROI, whereas the area fraction of acinus (*ρ*) is calculated as a ratio of the areas between acinus and ROI.

3.5 Fractal dimension (FD)

FD is used here as a potential microstructural index for characterizing the complexity of prostatic gland patterns, measuring the length of a curve by dividing it to smaller scales. For a given geometry (i.e. an ROI), firstly the boundary of acini is detected from binary image (i.e. ROI). To calculate the value of FD, box counting method [165] is used, where a grid of certain spacing is placed over the ROI and the number of boxes that contain white pixels (i.e. acinar structure) is counted (Fig. 3-2). This process is then repeated for multiple grids with varying spacing. As the box size increases, the number of counted boxes decreases, and the FD is calculated using linear regression of the logarithmic plots between the number of boxes and the chosen spacing of the grid, as shown in Eq. (3-1)

$$FD = \frac{\log(N(s))}{\log(1/s)} \tag{3-1}$$

where $N(s)$ is the number of boxes counted (i.e. those that contain white pixels), when spacing s (i.e. size of box) is used.

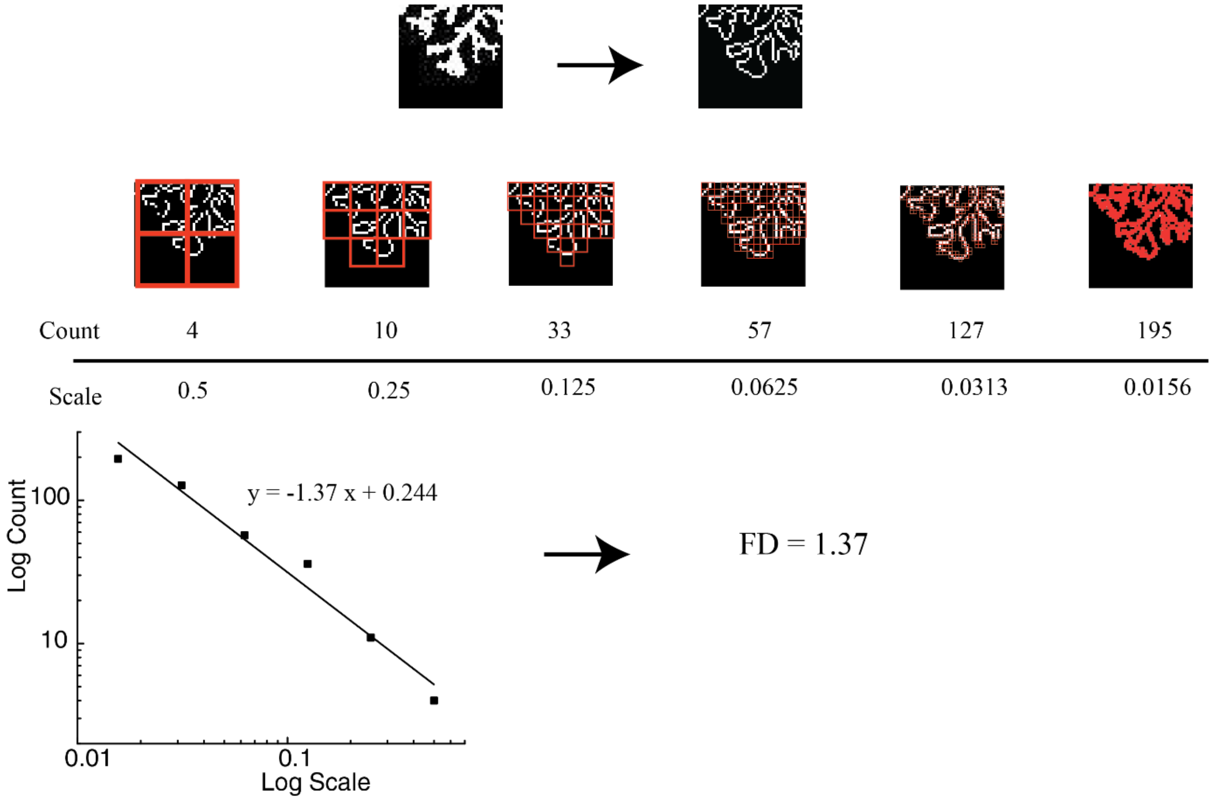

Figure 3-2. An example of analysis of single ROI, First the edge of the acinar structure is detected, followed by box counting method for fractal dimension. In which a series of girds of boxes progressively (from big to small) placed over the ROI and the number of boxes which has the acinar structure (i.e. white pixels) are counted. The FD value is measured by linear regression of natural logarithmic plot of box-count against scale.

3.6 Lacunarity

Lacunarity, L, is often used as a measure of how fractals (i.e. acinar fluid) fill space (i.e. prostatic tissue) with certain gaps (i.e. 'solid' tissue phase). The higher the lacunarity, the more or larger gaps a pattern presents (i.e. more tissue phase which are black pixels in binary image) which indicate a higher degree of heterogeneity (with respect to the distribution of acinar fluid) in tissue texture. In this study, L is used as one of the indices, which gives a quantitative measure of the heterogeneity of how the acinar structure is spatially distributed. It is obtained by means of box counting method, similarly to the method used for measuring the FD as mentioned above, and estimated based on the probability of the localization of the white pixels calculated from the number of white pixels per box as a function of box size, as shown in Eq. (3-2).

$$L_s = (\frac{\sigma_s}{\mu_s})^2 \tag{3-2}$$

where σ is the standard deviation and μ the mean of the number of pixels in white (i.e. those representing acinus fluid in binary images) in each counting box of size s. Similarly to Eq. (3-1), natural logarithmic plot of the number of boxes against scale and the gradient L was estimated using linear regression. It is important to note that, whilst FD represents how the curvature of a pattern changes over the varying scale as discussed above, lacunarity describes how the pattern is spatially distributed, thus providing additional information in quantifying the histological images (which may have same FD but different values of lacunarity due to different distributions of inclusions).

3.7 Influence Area fraction and size of acinus

Fig. 3-3 shows the variations in area fraction of acinar fluid (*A*) in healthy, BPH and cancerous samples of three different ROI sizes. For all ROI sizes used, the cancerous tissue is shown to have the least amount of acinar fluid, e.g. when ROI size of 0.54mm is used, with a median value of 3.2 %, followed by the benign samples (median value of 20.8%), and the BPH with the highest median value of 30.4%, although the BPH samples present a higher statistical variation, which is in line with what can be observed from the histological slide in Fig. 3-1. It is noted that the 25th and 75th percentile of the results in the cancerous tissue are significantly smaller than that of the non-cancerous tissues (i.e. BPH and healthy), however, their statistical distributions have certain overlap. This would mean that the area fraction of acinus in prostate may not be an effective microstructural index to distinguish the tissue pathological conditions for diagnostic purpose.

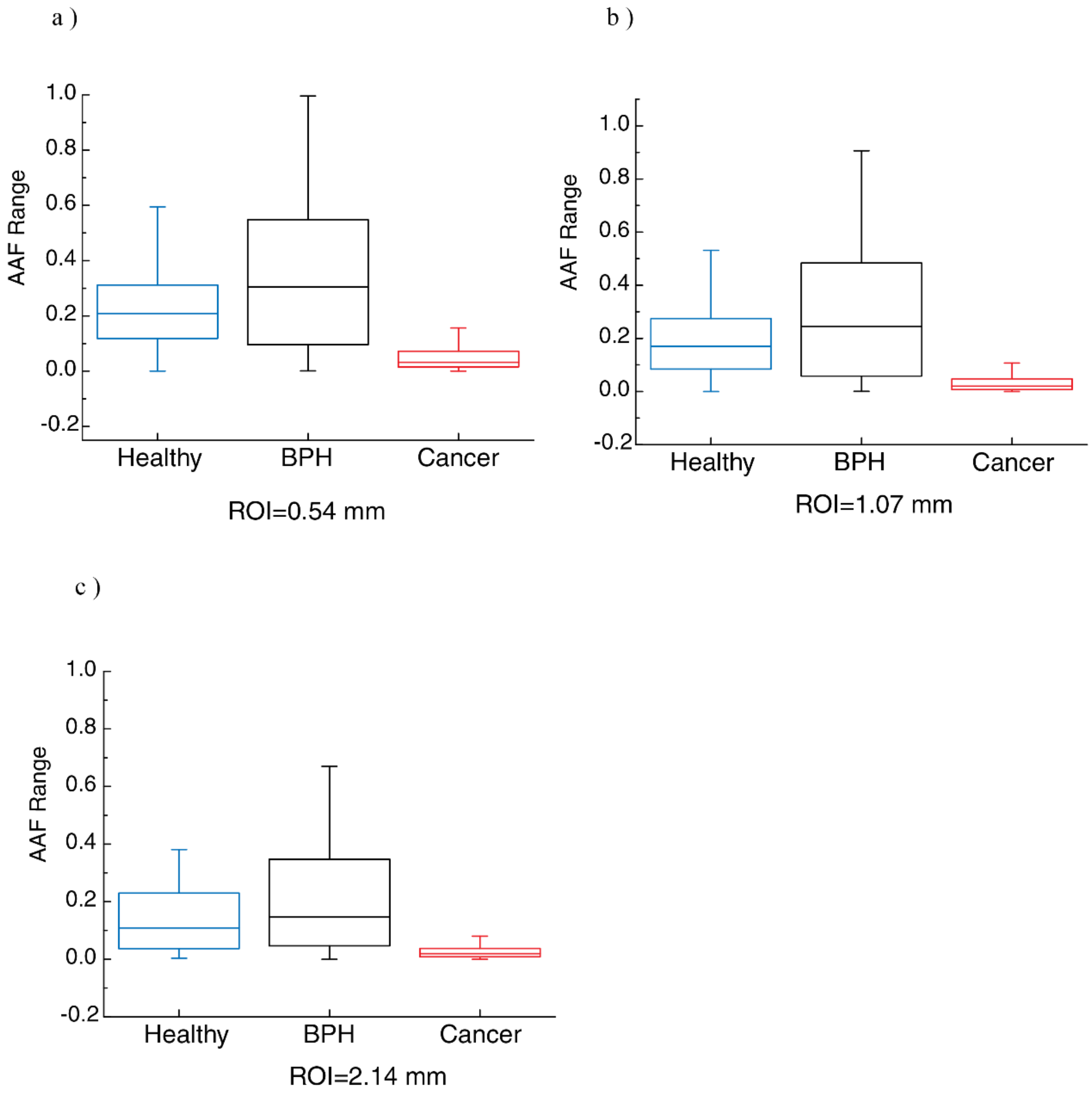

Figure 3-3. Range of acini area fraction in healthy, cancer and BPH tissues for different RVEs. Upper and lower whiskers represent 25th and 75th percentile and the horizontal line shows median.

Fig. 3-4a shows the size of acini for all ROIs considered. The mean acinar size varies among three tissue categories, lowest in cancerous tissue, followed by the healthy samples, and highest in BPH. It also varies with respect to the size of ROI , similar to the area fraction of acinus shown above, and a larger ROI size would result in a higher mean value of acinar size. This is due to the fact that, with larger ROI size being used, the acinar structures become less likely to be divided at the boundaries of the ROIs (i.e. included in more than one ROI), which is of particular relevance to BPH samples as the acinar size there is often much larger than in other two sample types. Fig. 3-4b shows the maximum acini size from all the samples and comparing them to the whole image, it is clear that for cancerous samples the the largest ROI covered the largest acini. However, for the healthy and BPH samples the convergence have not achieved in terms of covering the biggest acini.

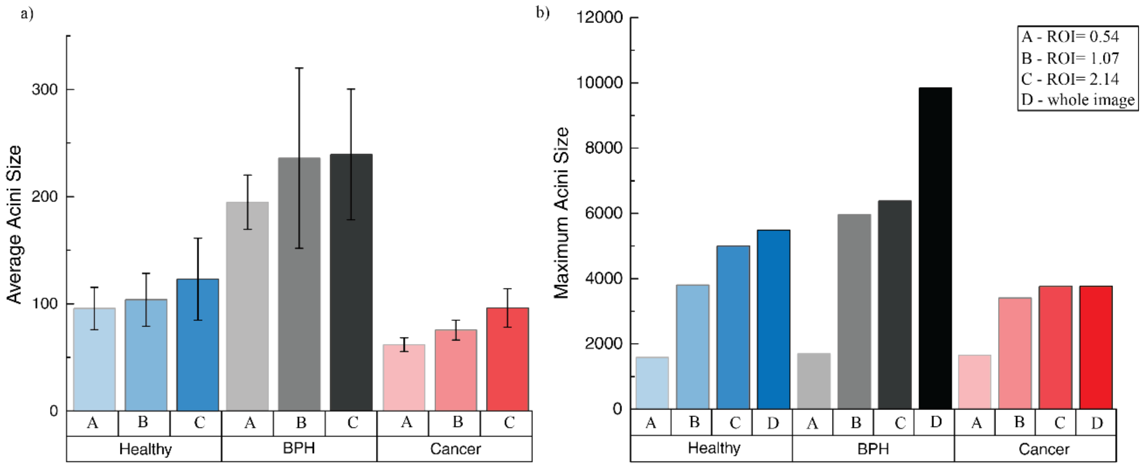

Figure 3-4. Average acini size for healthy, cancer and BPH in different ROIs (a). Standard deviation increase with increase of ROI size due to decrease of samples. The maximum acini size showed in (b) includes the largest acini in the whole image.

Change in acini size can be a useful parameter to distinguish between these three tissue conditions. In BPH the acini size increases due to enlargement of prostate glands, whilst the acinus becomes smaller in cancer due to irregular cell proliferation and penetration. It should be noted that the average acinar size, in comparison to acinar area fraction shown above, provides critical information about how ‘dispersed’ the acinar structures are. This finding is in fact in line with what has been reported where changes in acinar size have been shown to be correlated with the Gleason grade - the higher the Gleason grade the lower the average acini size[16].

3.8 Fractal Dimension Analysis

Fig. 3-5 shows the statistical distribution (in the form of histograms) of FD for all ROIs and sample groups considered. Interestingly, there are notable differences between the distributions of the relative frequency of FD presented for all ROIs assessed. For example when ROI size of 0.54 mm is used, as shown in Fig. 3-5(a), the mean value and standard deviation for FD is 0.93±0.30 for cancerous samples (in red) and 1.31±0.29 for healthy section and 1.04±0.21 for BPH section. Such trends also present in other cases using different ROI sizes. It is also crucial to note that, as FD represents the structural complexity at the pattern boundary, lower FD values in cancerous samples would indicate less ductal branches in acini, in comparison to healthy group which has the highest amount of branching of the acini and BPH which consists of mostly ‘round’ acini structure. This could be due to rapid proliferation of cells around acini which could make the acini smaller or cause the closure of acini ducts[16].

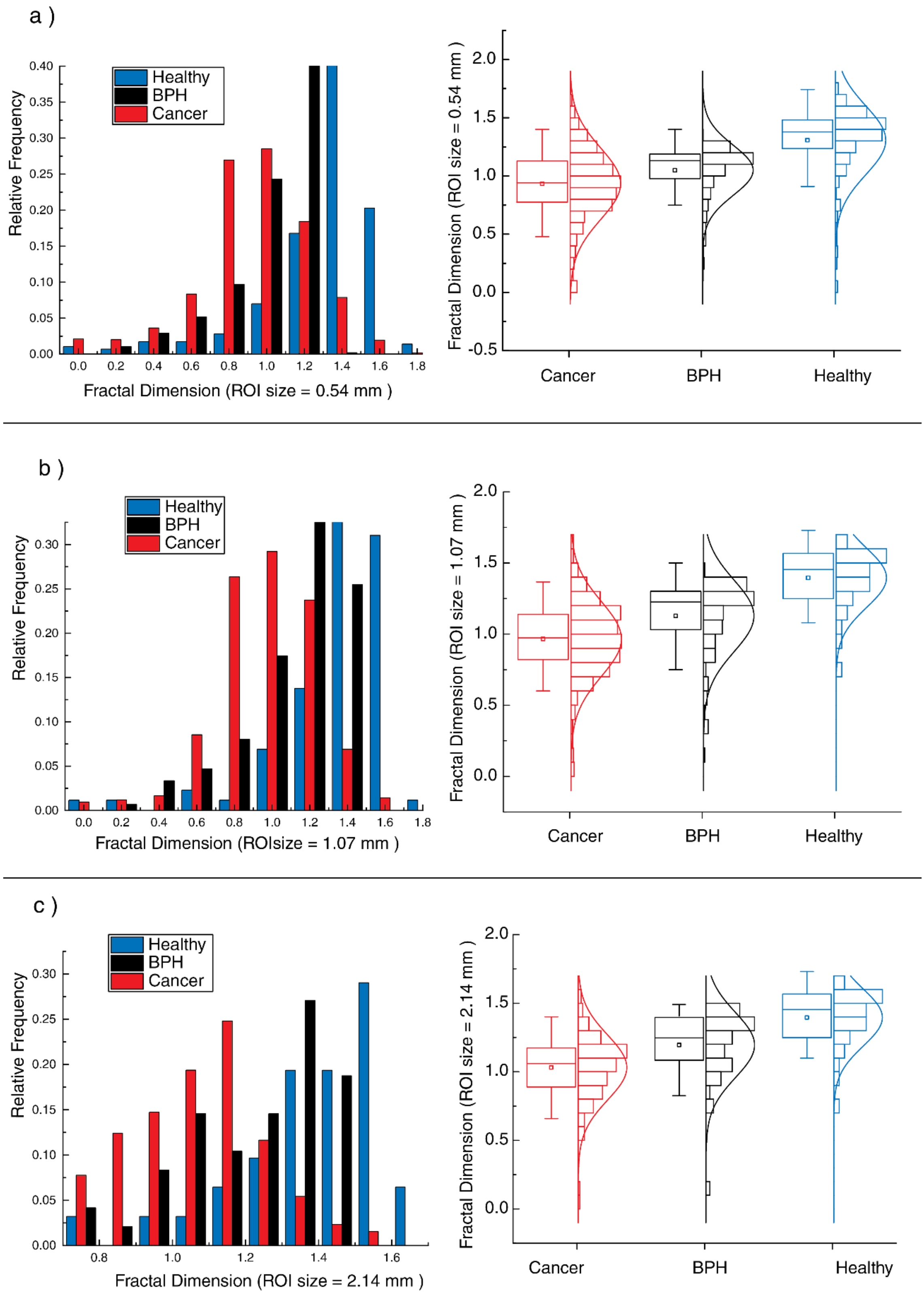

Figure 3-5. Statistical Fractal dimension analysis based on relative frequency and box chart for healthy, cancer and BPH tissues in three different ROIs. a) 0.54 mm b) 1.07 mm c) 2.14mm. Whiskers show the standard deviation and the box is boundaries are 25-75 percentile.

3.9 Lacunarity analysis

Fig. 3-6 illustrates the histogram of lacunarity, *L*, of healthy, BPH and cancerous samples for three ROI sizes considered, respectively. As mentioned above, it represents the heterogeneity of the tissue morphology (i.e. how the acinar structures are spatially distributed within the tissue 'solid' phase). It can be seen that the BPH samples present the lowest value of lacunarity, which could be due to the fact that acinar structure therein are large and the area fraction of acini to the tissue is high. In contrast, lacunarity of cancerous samples is the highest which shows the highly dispersed acinar phase therein. Healthy samples have overall intermediate value of lacunarity. With the increasing ROI size, lacunarity increase in all samples, which shows lacunarity can change due to ROI size especially in healthy and BPH samples. Therefore larger ROIs are better to be considered for healthy and BPH.

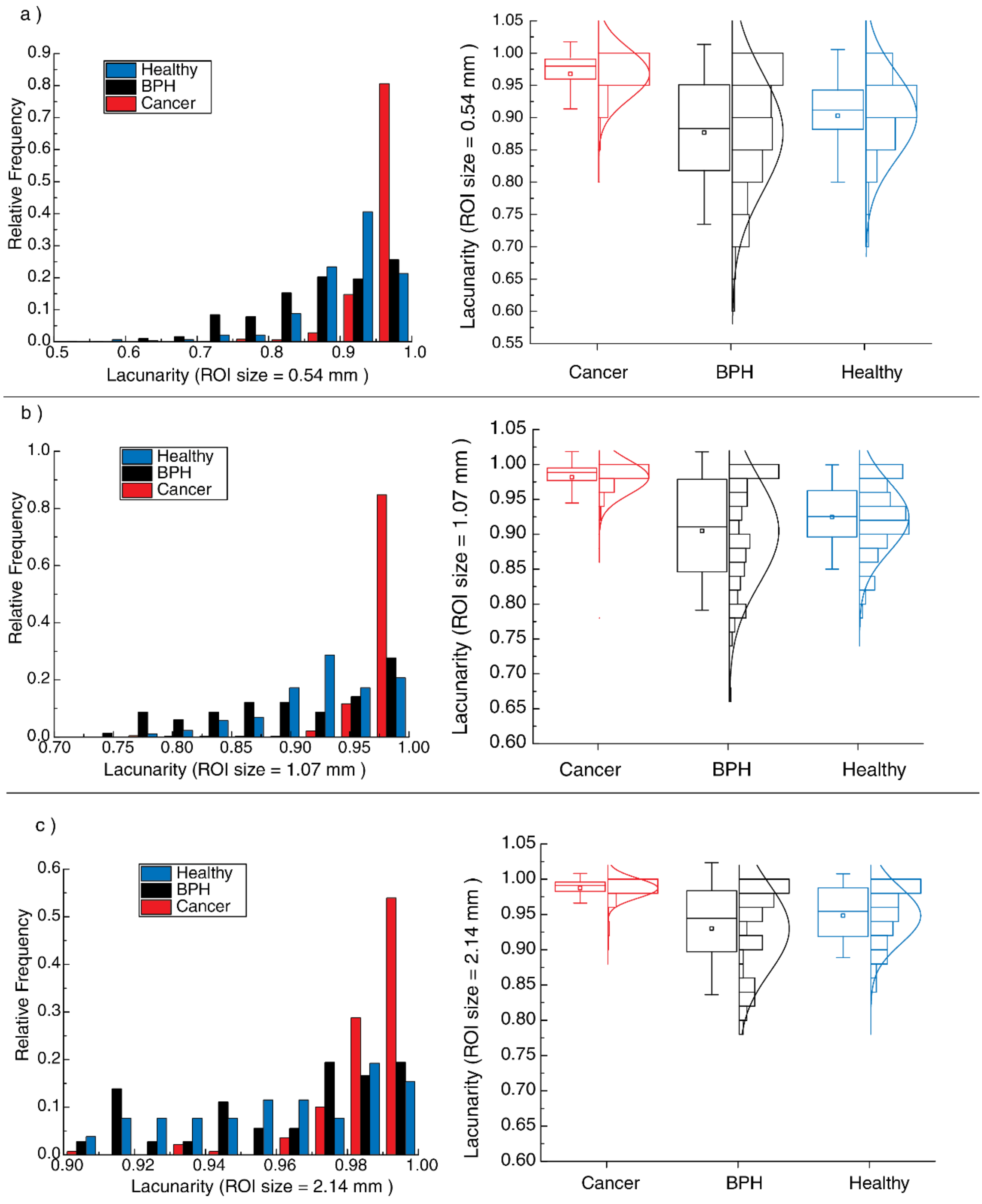

Figure 3-6. Statistical Lacunarity analysis based on relative frequency and box chart for healthy, cancer and BPH tissues in three different ROIs. a) 0.54 mm b) 1.07 mm c) 2.14mm. Whiskers show the standard deviation and the box is boundaries are 25-75 percentile.

3.10 Concluding remarks

This chapter aimed to establish microstructural indices based on the histological image and perform evaluations from a different perspectives i.e. microstructural and morphological variation of acini. It has been shown that the microstructure and texture of healthy tissue vary between healthy, BPH and cancerous tissues. In this chapter following conclusions were drawn:

- The average acini size and the acini ratio fraction: cancer presents the lowest acini fraction, which shows that the acini size reduces from healthy condition due to existence of cancer. BPH has the largest acini size also the highest acini fraction. There is also a certain degree of increase in acini size due to the presence of BPH.
- Fractal dimension could be a useful index for categorizing different tissue pathophysiology, which could be correlated to Gleason grade. Healthy tissue presents higher fractal dimension. Fractal dimension shows the branching feature in healthy tissue, however in other tissue conditions this value reduces.
- Lacunarity shows potential to be consider as a complementary index for the purpose of interpretation of tissue heterogeneity.

The methodology presented here, at its current stage, has some limitations; the number of histology and patients in this study is limited due to complexity of prostatectomy procedure for obtaining the complete histological image from patient; increase of such data would provide a better database and improved statistical analysis. Although biopsy is an ideal approach for diagnosing prostate cancer, it is invasive. It is therefore important to find a way to combine it with other non-invasive methods and use the current biopsies database for correlating tissue morphology to mechanical response which can be use in other non-invasive diagnostic methods (i.e. digital rectal examination (DRE) and elastography). This can be achieved, partly, by performing a structural homogenization computationally which will be presented in the following chapter.

CHAPTER 4

Mechano-morphological Homogenization of Prostate Tissue

Contents

4.1 Summary

In the previous chapter the importance of histological and morphological changes due to various pathophysiological conditions has been described. It is of critical importance to investigate the potential use of morphological changes in tissue microstructure in diagnosis. However it is still unclear how the microstructural changes in tissue

morphology quantitatively affect its apparent mechanical properties. This is of critical relevance to some clinical diagnostic methods such as those using palpation as primary diagnosis, and it is also necessary to explore the length scale at which the apparent mechanical properties should be measured.

In this chapter, a study on the effects of morphological changes in cancer, healthy and BPH samples on their apparent mechanical properties is carried out. The apparent mechanical properties of tissue samples is derived using numerical homogenization method based on the tissue microstructures reconstructed from histological images. Results will be compared to the microstructural indices presented in the previous chapter, with the aim of finding possible correlations between tissue morphological and mechanical properties. It is hoped that the combination of microstructural and mechanical indices can give more useful information for improved diagnostic capability.

4.2 Modelling of histological images

As mentioned in Chapter 3, prostatic tissue sample was excised during total prostatectomy using the laparoscopic approach. The pathological analysis showed the patient is diagnosed with acinar adenocarcinoma with a Gleason 4+3 grade albeit a lower PSA level of $9.1 ng/ml$. The image of the histological slide is segmented based on three main tissue conditions, i.e. healthy, cancerous, BPH tissues. To understand the sensitivity of ROI sizes with mechanical properties, three ROIs sizes, namely 0.54 mm (40 × 40 pixels), 1.07 mm (80 × 80 pixels) and, 2.14 mm (160 × 160 pixels), as described in Table 3-1, are used. The computational models were based on the segmented ROIs, which were firstly converted into grayscale using a range of 0-142 (where 0 is black and 255 is white) to identify regions containing acinar fluid in tissue histology and 143-255 for ‘solid’ tissue phase, in Scan-IP (Simpleware Ltd., Exeter, UK), and is imported in ABAQUS (Dassault Systemes, VlizyVillacoublay, France) for further numerical analysis.

4.3 Homogenization formulation

In this study, periodic boundary condition (PBC) is used for numerical homogenization to obtain effective properties of model microstructures. PBC, which can produce more realistic results than other methods[140] and is commonly used for homogenization such as kinematically uniform boundary condition (KUBC) and statically uniform boundary condition (SUBC), is a robust method that requires the periodicity for, e.g., displacement, at corresponding boundaries[140]. Therefore, to impose PBC in a rectangular ROI, it is usually achieved by linking the FE nodes at corresponding positions at the ROI boundaries and making them have the same displacement. However, this would require the ROI to have a symmetrical mesh, which is not always possible to have particularly for those reconstructed from histological slide with complex microstructures and geometries. In a recent study, Palacio-Torralba et.al.[166] suggested a novel numerical implementation of the PBC method using a non-symmetrical mesh by adding virtual periodic ‘nodes’ at the ROI boundaries. The variables of those nodes, different from the nodes used in FE model, are calculated using interpolation function from the adjacent FE nodes. The constraints that impose the periodic (e.g. on nodal displacement) at the boundary FE nodes are instead applied on those virtual interpolation points. By doing so, the periodic mesh at the ROI boundary is no longer required, which is of importance use to the histological images explored here.

Fig. 4-2 illustrates how this method is implemented in Finite Element, where Fig. 4-2(a) is the periodic meshing (i.e. each node on one boundary has a matching node at the corresponding boundary) used in the traditional PBC approach and Fig. 4-2(b) shows the new scheme with virtual interpolation points in addition to an arbitrary mesh. The periodicity is ensured between interpolation points, or between a node and an interpolation point, and the following equations should be satisfied (e.g. between the FE node *c* and an interpolation points *d*),

$$U_x^a = U_x^b \tag{4-1}$$

$$U_y^a = U_y^b \tag{4-2}$$

$$U_x^c = U_x^d \tag{4-3}$$

and

$$U_y^c = U_y^d \tag{4-4}$$

The displacements (i.e. x and y components) of the FE node c, equivalent to the corresponding interpolation point d, can be expressed by linear interpolation between two adjacent FE nodes as follows

$$U_x^c = \frac{(U_x^{d_{up}} - U_x^{d_{down}})}{l} \cdot \frac{l}{2} + U_x^{d_{down}} \tag{4-5}$$

and similarly for the y axis,

$$U_y^c = \frac{(U_y^{d_{up}} - U_y^{d_{down}})}{l} \cdot \frac{l}{2} + U_y^{d_{down}} \tag{4-6}$$

However, In case the control points are not coincident with the Finite Element nodes, therefore the displacements at both controls points need to be expressed as a function of FE nodes, e.g. in the case of points *f* and *g*, as

$$\frac{(U_x^{f_{left}} - U_x^{f_{right}})}{l} \cdot \frac{l}{2} + U_x^{f_{right}} = \frac{(U_x^{g_{left}} - U_x^{g_{right}})}{l} \cdot \frac{l}{2} + U_x^{g_{right}} \tag{4-7}$$

and

$$\frac{(U_y^{f_{left}} - U_y^{f_{right}})}{l} \cdot \frac{l}{2} + U_y^{f_{right}} = \frac{(U_y^{g_{left}} - U_y^{g_{right}})}{l} \cdot \frac{l}{2} + U_y^{g_{right}} + \epsilon_0 \tag{4-8}$$

where ϵ_0 is the global displacement applied along the y axis.

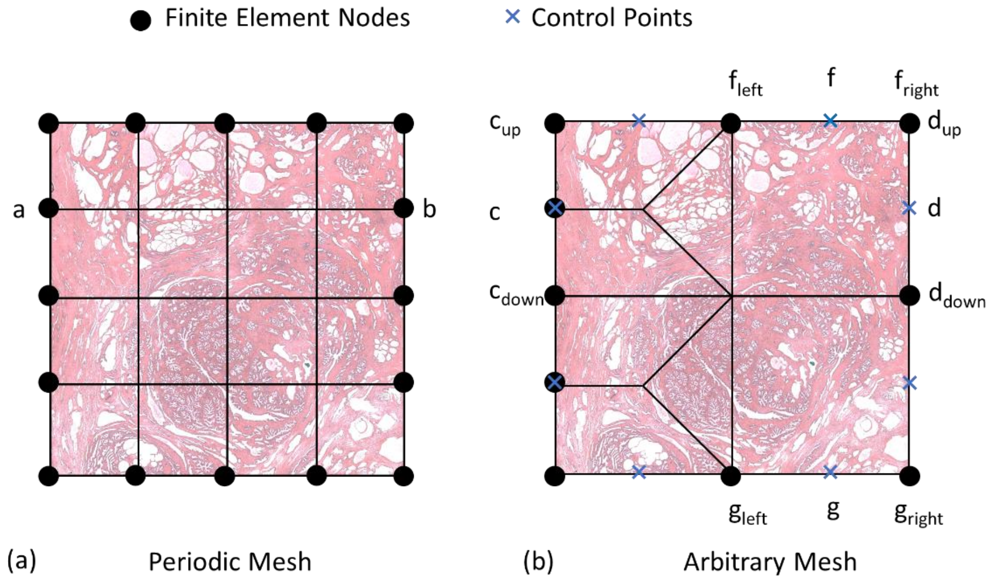

Figure 4-2. (a) Example of a periodic mesh where nodes in all the faces have a matching node at the opposite faces (e.g. node ‘a’ has a match node ‘b’). (b) shows an arbitrary mesh where some nodes do not have a matching node on the opposite face(for instance c)[166].

The homogenized stiffness matrix is derived from three trial tests, namely two uni-axial tensile tests in x and y axis, and a shear test. In the small strain scenario a 10% strain was considered. In each test the average strain $(\epsilon_{xx}, \epsilon_{yy}, \epsilon_{xy})$ and stress $(\sigma_{xx}, \sigma_{yy}, \sigma_{xy})$ were calculated over the ROI. Thus to obtain the 9 components of the stiffness tensor shown below, a set of linear equations needs to be solved so that following equations are satisfied

$$\langle \sigma \rangle = C_{ij}^{effective} \langle \epsilon \rangle \tag{4-9}$$

$where$ $\langle \sigma \rangle$ is the average stress and $\langle \epsilon \rangle$ the average strain in the ROI. $C_{ij}^{effective}$ is the apparent stiffness tensor of the ROI. For the sake of simplicity, small strains are considered in the modelling. In this study the stromal tissue (i.e. solid phase) is modelled with the elastic modulus of 17kPa and a Poisson's ratio of 0.3 and the mechanical properties of fluid phase is considered as water i.e. nearly incompressible solid with a bulk modulus of 2 GPa[167].

4.4 Effects of ROI size in apparent mechanical properties of prostate tissue

The aim of this section is to analyse the mechanical properties of each tissue type and to investigate the influence of ROI size in mechanical properties of healthy, cancerous and BPH samples. Fig. 4-3 shows the components of apparent elastic stiffness tensor for all three sample groups. It should be noted that the average stiffness values of cancerous tissue are higher than healthy samples, which have similar elastic properties to BPH ones. This finding is in line with the published data in experimental studies[12], [106], [166]. Cancerous tissue has higher elastic properties which could be due to the reduction of acini size thus increased fraction of solid tissue phase, due to fast proliferation of cells therein.

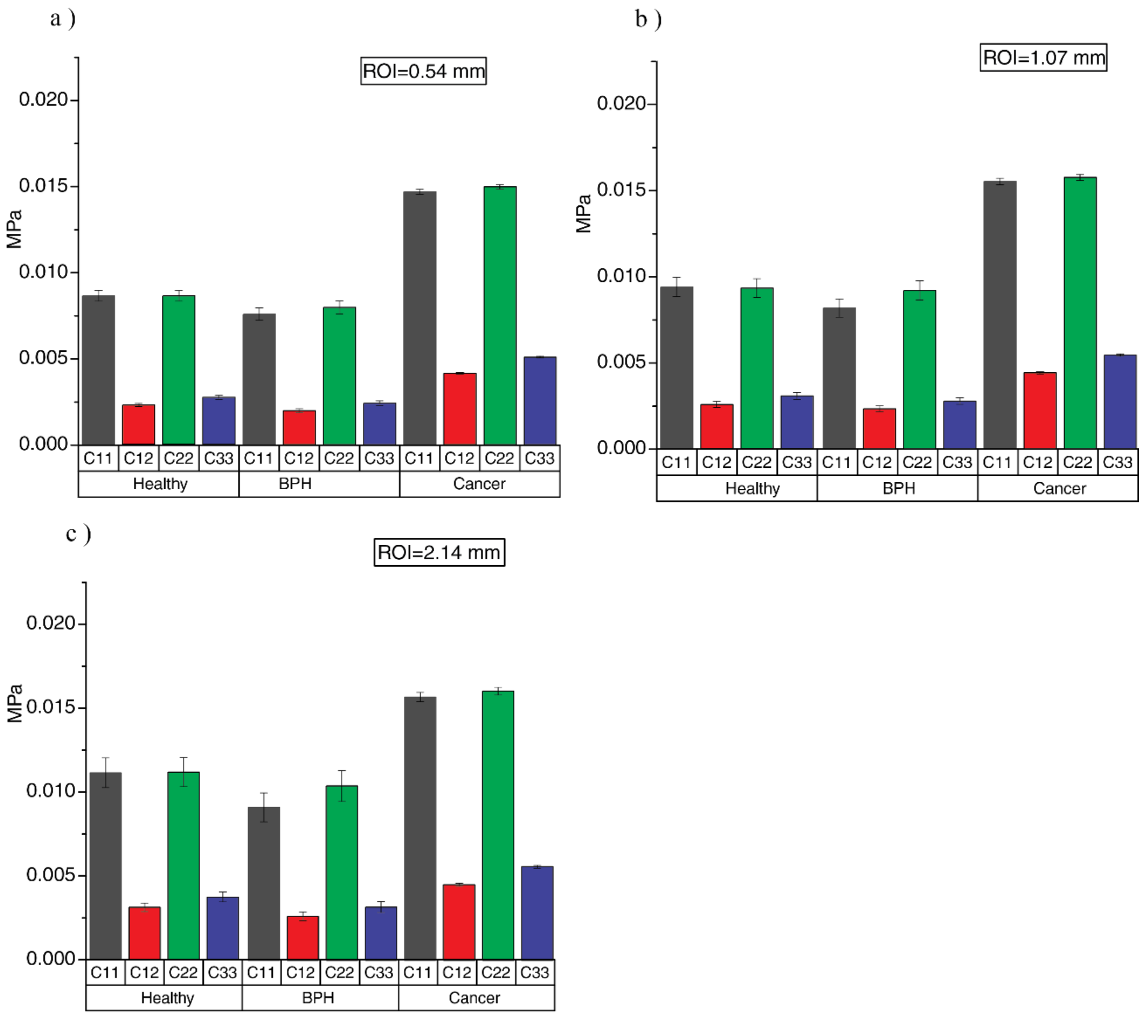

Figure 4-3. Average mechanical properties and their respective standard error for the healthy, BPH and cancerous ROI. Three different ROI size a) 0.54 mm b) 1.07 mm c) 2.14 mm have been used.

4.5 Anisotropy

Wilcoxon signed rank test was performed to analyse the statistical comparison of average of C11 and C22 component of effective stiffness tensor. The result of this test provides the anisotropy assessment of three tissue type's i.e. BPH, healthy and cancerous as illustrated in Table. 4-2. The value h = 1 indicates that the test rejects the null hypothesis that there is no difference between the grade medians at the 5% significance level (i.e. p-value > 0.05). Results show that BPH tissue show anisotropy for three ROI sizes, such behaviour could be due the fact that the acini structure in BPH tissue become large and the size and distribution of them are not uniform. Healthy samples, however, have shown isotropy for all ROI sizes i.e. H-value is 0, which indicate that C11 and C22 for healthy samples the distribution is not significantly different. Cancerous samples have shown anisotropy for the smallest ROI (i.e. 0.54 mm) and isotropy for ROI = 1.07 mm and ROI = 2.14 mm. This shows that the degree of isotropy increases by increasing the length scale of the tissue in cancerous samples.

Table 4-2. Statistical comparison of C11 and C22 component of effective stiffness tensor for BPH, healthy and cancerous samples by performing Wilcoxon signed rank test. Three different ROI size a) 0.54 mm b) 1.07 mm c) 2.14 mm have been used. H = 1 indicates the rejection of the null hypothesis (i.e. anisotropic) and H = 0 indicates the failure to rejection of the null hypothesis (i.e. isotropic)

Size of ROI	**0.54 mm (40 × 40 pixels)**		**1.07 mm (80 × 80 pixels)**		**2.14 mm (160 × 160 pixels)**	
	H-value	**P-value**	**H-value**	**P-value**	**H-value**	**P-value**
BPH	1	0.0116	1	2.7246e-05	1	0.0042
Healthy	0	0.7387	0	0.7246	0	0.5999
Cancer	1	0.0012	0	0.1088	0	0.3104

Fig. 4-4 illustrates the degree of anisotropy of BPH samples when three ROI sizes are used. Results show that BPH tissue has high degree of anisotropy since most samples present significant deviations from the anisotropy ‘line’. Fig 4-4 (a) shows that a high number of ROIs have stiffness values close to 0, which indicates that, when the smallest ROI size is used, the majority of acinar areas are larger than 0.54mm, making those ROI mostly consist of ‘water’. This would imply that using a very small value as the size of

ROI may not be appropriate for characterising the apparent mechanical properties of BPH samples, as the size is lower than the characteristic length scale (i.e. the size of the acinar structures) therein.

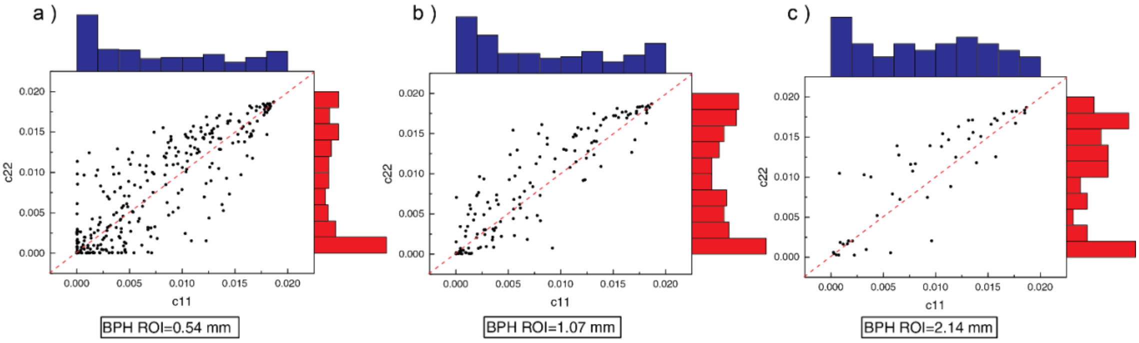

Figure 4-4. Comparison of anisotropy of C11 and C22 component of effective stiffness tensor for BPH samples. Three different ROI size a) 0.54 mm b) 1.07 mm c) 2.14 mm have been used.

Fig. 4-5 shows similar results, but for cancerous samples. Results indicate that the cancerous tissue has lower degree of anisotropy than BPH tissue, since the majority of data are positioned on the diagonal line. This could be related to lower amount of acini in cancerous tissue, during the cancer, acini become smaller due to the fast proliferation of cells[168]. Concentration of data in higher range of C11 and C22, again, emphasize the higher stiffness in cancerous tissue which could be related to the average acini size and also the area fraction of acini to tissue from previous chapter.

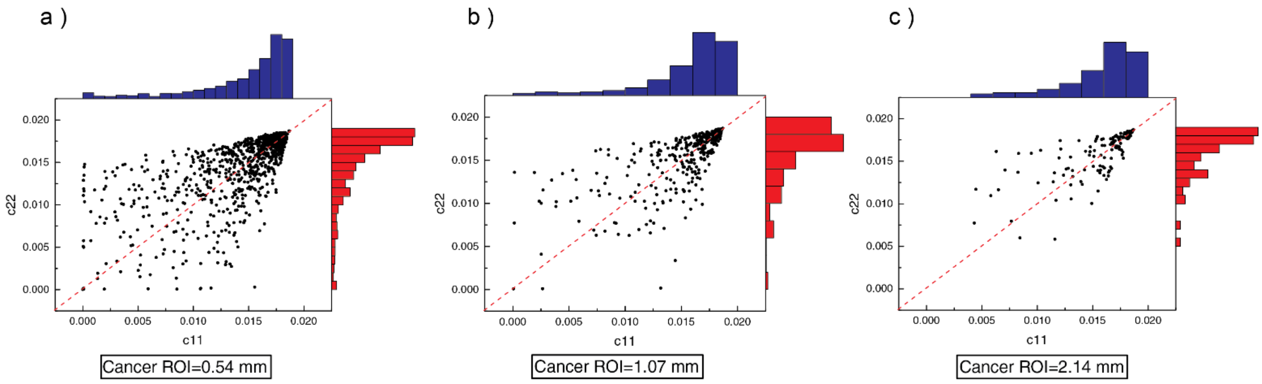

Figure 4-5. Comparison of anisotropy of C11 and C22 component of effective stiffness tensor for cancerous samples. Three different ROI size a) 0.54 mm b) 1.07 mm c) 2.14 mm have been used.

Fig. 4-6 shows the anisotropy assessment for healthy tissue in three ROI sizes. Results show that the degree of anisotropy in healthy tissue is less than BPH most of the samples have the same value in both axis (i.e.C11 and C22). The distribution of the samples shows that the healthy samples on the average have higher stiffness than BPH and lower than cancerous tissue. That would highlight that in healthy tissue the features of microstructure has scattered more uniformly and then due to different pathology (e.g. cancerous or BPH) the structure changes which has influence on increase (e.g. cancer) or decrease (e.g. BPH) of stiffness.

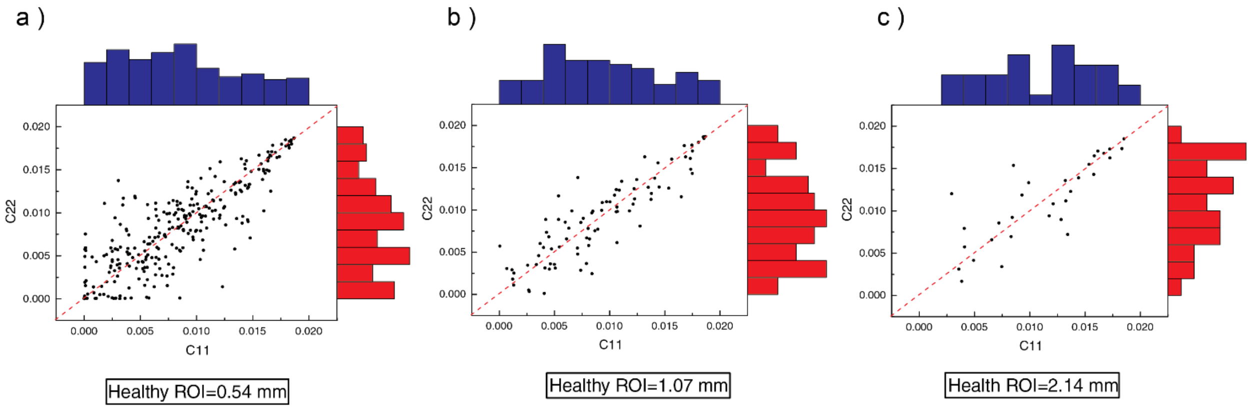

Figure 4-6. Comparison of anisotropy of C11 and C22 component of effective stiffness tensor for healthy samples. Three different ROI size a) 0.54 mm b) 1.07 mm c) 2.14 mm have been used.

These results suggest that with a sufficiently large database it would be possible to construct benchmark histograms for different types of pathologies at lower scales, against which clinical measurements could be employed to determine the presence of certain diseases.

4.6 Concluding remarks

The objective of this chapter was to analyse how changes in prostate tissue microstructure subject to various pathophysiological conditions influence the apparent tissue elasticity, and to assess the degree of anisotropy of aforementioned pathologies as well as their influences by the chosen ROI size and correlate them with the results of chapter 3.

In this chapter, apparent mechanical properties of prostate tissue which has three categories, namely healthy, BPH and cancerous tissues, have been analysed using numerical homogenization method with periodic boundary conditions. It has been shown that cancerous samples on average present highest elastic modulus among all three tissue types. This could be related to the smallest acini size in cancerous tissue (see Fig. 3-3 for details), due to cancerous and rapid proliferation of cells leading to smaller acinar structures and higher content of solid tissue phase. On the contrary, for BPH samples, the acinar structures become larger, therefore, BPH on average has lowest apparent mechanical properties, whilst healthy samples present elastic properties in between. On the other hand, anisotropy of all tissue samples have been performed. BPH samples, again, showed a higher degree of anisotropy among three tissue types. Healthy and cancerous have shown, on average, statistically isotropic (Table 4-2). The chosen size of ROI in those analysis has been proved to be critical - this is notable particularly in BPH samples when the smallest ROI size is used, since a large number of ROI present extremely low elastic properties, indicating high fractions of ‘water’ phase in those ROIs. It is worth mentioning that the anisotropy also varies with respect to the length scale chosen (i.e. the size of ROI). Results from lower scale can provide more information about stiffness of tissue at a local length scale, and from higher scale it can provide useful information that relate certain mechanical properties to its pathology for diagnosis purpose.

It is worth mentioning that based on the results of the chapter 3, cancerous and BPH tissues have smallest and highest acini area fraction respectively, the influence of this results could be observed in higher and lower stiffness of cancerous and BPH samples respectively.

Only the data from one histology image has been analysed in this study. It is expected to increase such database which would improve the quality of this study and provide better understanding of the changes in mechanical properties due to various pathologies at different stages of cancer development. In this chapter fluid was modelled as a solid material as one of the two phases modelled. In the next chapter biphasic model for homogenization using FSI will be employed to better understand the physical interaction between the solid tissue phase and interstitial fluid.

CHAPTER 5

Parametric study of simplified tissue microstructure – considering its biphasic nature

Contents

5.1 Summary

The influence of pathophysiological condition of tissue on its structure, as well as the tissue anisotropy, have been discussed in previous chapters. As emphasized in chapter 4, it is important to consider the biphasic nature of tissue for the homogenization purpose. This chapter, as a step forward, presents a computational framework for characterizing the viscoelasticity of soft tissue arising from the multiphasic and multiphysical interactions associated with its underlying microstructure. The mechanical interaction between the solid and fluid phases within the tissue microstructure is modelled by fluid-structure interaction (FSI) in a framework of numerical homogenization, subject to various parameters such as strain rate, tissue morphology, the viscosity of the interstitial fluid and tissue (solid) mechanical properties.

5.2 Simplified channel models – a parametric study

In order to understand the role of fluid-filled components on the dynamic mechanical properties of soft tissue, a simple biphasic model will be adopted based on similar structure as in real tissue histology Fig. 5-1, consisting of a nonlinear hyperelastic solid and a liquid whose essential property is its viscosity. This type of physical model is consistent with the viscoelastic approaches often used to fit experimental measurements of soft tissue [169].

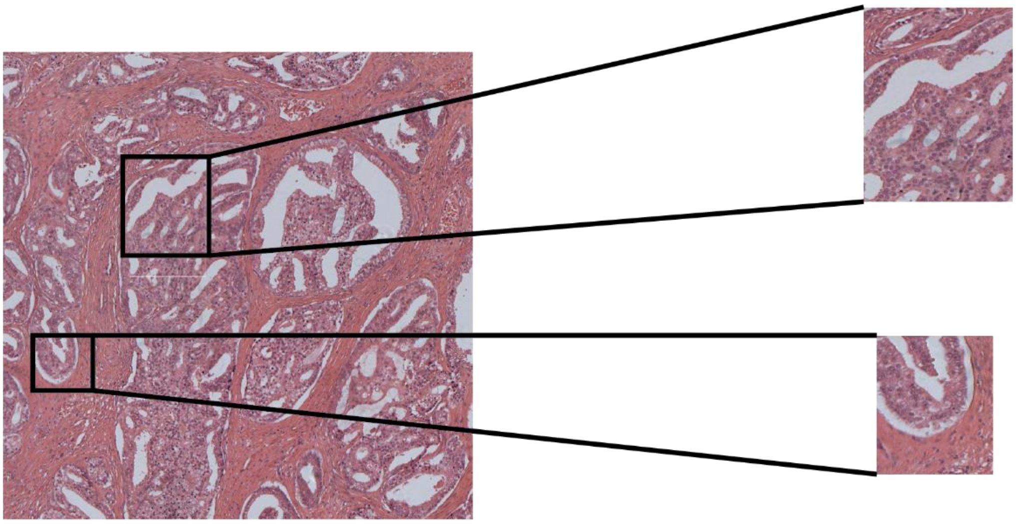

Figure 5-1. Prostate tissue histology which gives inspiration for the simple biphasic model

To better understand how the tissue microstructure, in particular the interaction between the fluid-filled areas and the “solid” phase, affects the apparent tissue viscoelasticity, a series of models were devised, all of size 560×560 μm, with systematically variable geometry corresponding to the size of a typical acinar structure in prostate as an exemplar tissue. The fluid channels are all of sinusoidal shape with various degrees of complexity, having two ‘frequencies’ (Models 1 and 2) and three ‘amplitudes’ (a, b and c) as illustrated in Fig. 5-2. The initial width of the channel (*G*, in Fig. 5-2) was fixed at 27 μm which corresponds to the size of the canaliculi connecting the acinar structures in human prostate. In order to characterize the viscoelastic behaviour of the models, a numerical homogenization formulation was adopted here using prescribed loading and boundary conditions.

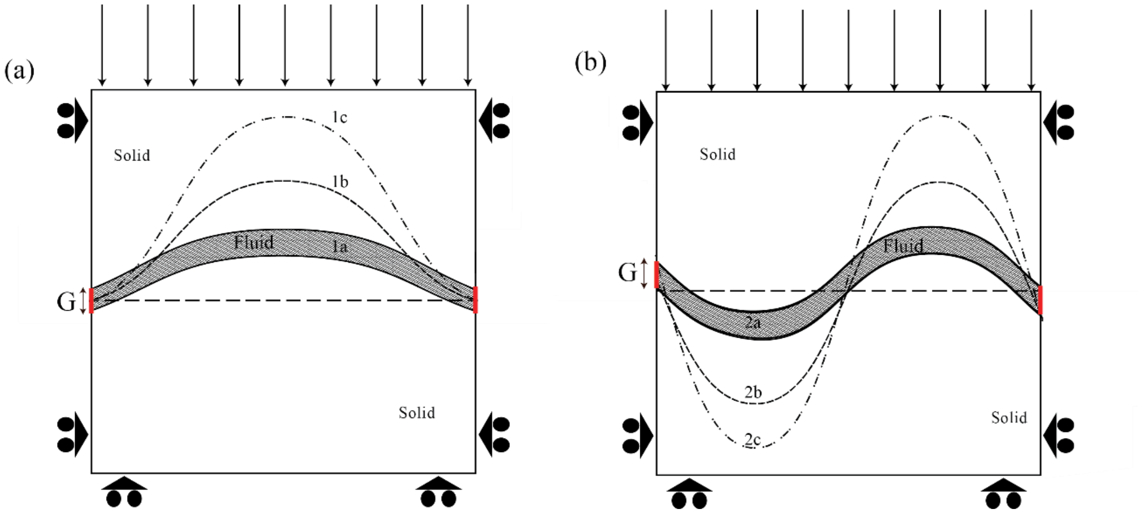

Figure 5-2. Schematic diagrams of two simplified yet representative tissue microstructural models (i.e. (a) model 1 and (b) model 2) with parameterized channel geometries (i.e. *a, b* and *c* are three 'amplitudes').

5.3 The theory of FSI

In FSI, fluid and solid mechanics are combined in order to simulate the interaction between fluid flow and solid structure (i.e. how fluid flow deforms the solid structure, and vice versa). The solid structure is often modelled in Lagrangian description and the fluid flow in Eulerian formulation, and the FSI couplings are often formulated at the boundaries between the fluid and the solid phases. However, when considering a fluid flow interacting with a solid medium the fluid domain changes as a function of time, and an arbitrary Lagrangian-Eulerian (ALE) description of motion is needed. The Lagrangian equation of motion of the structure is

$$\rho \frac{\partial^2 \boldsymbol{u}}{\partial t^2} = \nabla . \tau + \boldsymbol{f}^B \tag{5-1}$$

where ρ is the density, $\boldsymbol{u}$ is the vector of structural displacements, t is the time, τ is the Cauchy stress tensor, $\boldsymbol{f}^{\boldsymbol{B}}$ is the vector of body forces, and (∇.) represents the divergence operator (in the deformed configuration). The boundary conditions needed to solve Eq. (5-1) are,

$$\begin{aligned} \boldsymbol{u} &= \boldsymbol{u}_S \text{ on } S_u \\ \tau . \boldsymbol{n} &= \boldsymbol{f}^S \text{ on } S_f \end{aligned} \tag{5-2}$$

Where S_u and S_f represent the parts of the boundary with prescribed displacements, $\mathbf{u}_s$, and tractions, $\boldsymbol{f}^S$, respectively; and **n** is a unit outward normal vector to the boundary. The equations of motion of a compressible Newtonian fluid flow in the ALE description of motion are

$$\rho \frac{\partial \mathbf{v}}{\partial t^2} + \rho[(\mathbf{v} - \hat{\mathbf{v}}).\nabla]\mathbf{v} = \nabla.\tau + \boldsymbol{f}^B \tag{5-3}$$

$$\frac{\partial \rho}{\partial t} + (\mathbf{v} - \hat{\mathbf{v}}).\nabla \rho + \rho \nabla.\mathbf{v} = 0 \tag{5-4}$$

$$\rho \frac{\partial e}{\partial t} + \rho(\mathbf{v} - \hat{\mathbf{v}}).\nabla e = \tau.\boldsymbol{D} - \nabla.\mathbf{q} + q^B \tag{5-5}$$

where ρ here is the fluid density; **v** is the fluid velocity; $\hat{\mathbf{v}}$ is the velocity of the moving ALE frame; τ is the fluid stress tensor, $\boldsymbol{f}^B$ is the vector of body forces; e is the specific internal energy; **D** is the velocity strain (rate-of-strain) tensor, $2\mathbf{D} = \nabla\mathbf{v} + (\nabla\mathbf{v})^T$; **q** is the heat flux vector; q^B is the rate of heat generated per unit volume; (∇) represent the divergence and gradient operators. Equation (5-3) is the momentum equation and (5-4) and (5-5) are the equations of conservation of mass and energy respectively. The boundary conditions required to solve Eqs. (5-3) to (5-5) are discussed in detail in [170]. At the interface between fluid flow and solid equilibrium and compatibility conditions must be satisfied at the fluid-structure interface. These conditions are

$$\tau^S.\mathbf{n} = \tau^F.\mathbf{n} \tag{5-6}$$

$$\mathbf{u}^I(t) = \hat{\mathbf{u}}^I(t)$$

$$\dot{\mathbf{u}}^I(t) = \mathbf{v}^I(t) = \hat{\mathbf{v}}^I(t) \quad (5\text{-}7)$$

$$\ddot{\mathbf{u}}^I(t) = \dot{\mathbf{v}}^I(t) = \dot{\hat{\mathbf{v}}}^I(t)$$

where **n** is a unit vector normal to the fluid-solid interface, **u** and $\hat{\mathbf{u}}$ are the displacements of the structure and the fluid domain (or mesh in a finite element analysis), respectively, **v** is the fluid velocity and $\hat{\mathbf{v}}$ the velocity of the fluid domain, the dot represents a time derivative, and the superscripts *I*, *S* and *F* denote the interface, and the solid and fluid media, respectively. There are two different approaches that are often used in FSI, namely direct or iterative approach. In the direct (monolithic) approach, the governing equations of fluid flow and the solid structure are combined and treated all together, often solved simultaneously by the same solver. In contrast, in the iterative (partitioned) approach, the governing equations of fluid flow and the solid structure are solved individually in succession, feeding information at the interfaces to each other. In this thesis the FSI problem is solved in ADINA (ADINA R&D Inc., MA, USA), and the direct method has been adopted and will be explained below.[171]

5.3.1 Direct Two-way FSI

In this method, the fluid and solid equations are combined and treated altogether. They are often linearized in a matrix system and no iteration is needed for fluid and solid models. The direct FSI two way coupling method, in general, is faster than the iterative method. It has the advantage of solving very difficult FSI problem, such as large deformations with 'soft structure/material' or highly compressible flow.[171]

5.3.2 Iterative Two-way Fluid solid interaction

In this computing method, the fluid equations and the solid equations are solved individually until the solution reaches convergence. The fluid equations are solved using prescribed solid displacement until the stress criterion becomes satisfied, whereas the fluid nodal displacement also follows the same procedure. Convergence needs to be checked depending on the chosen criteria (i.e. displacement and stress). If convergence is not achieved, the solver starts the next iteration until convergence.[171]

5.4 Numerical implementation

The mechanical interaction between the solid and fluid phases within the tissue microstructure was modelled in ADINA (ADINA R&D Inc., MA ,USA) using fully coupled two-way fluid-structure interaction, where the fluid and structural models are mechanically coupled through displacement and traction conditions at the interface. Numerical homogenization was used here to quantify how the tissue microstructure and the movement of the fluid influence its apparent viscoelasticity. The solid phase was modelled as a nonlinear hyperelastic material and the fluid as incompressible laminar viscous fluid. All models were subjected to a stress relaxation test, consisting of increasing the compressive displacement of the upper surface at one of three strain rates to a fixed strain and following the decay in force with time thereafter. The same process was applied to the simplified geometries and then to the two simplified histological samples.

It is worth noting at the outset that, since this study aims at understanding the contribution of tissue viscoelasticity arising from the interaction between fluid and solid phases within the tissue microstructure, the use of macroscopically-determined mechanical properties for the “solid” phase is only strictly accurate if it contains no significant glandular material. Furthermore, viscoelasticity arising from the intrinsic properties of collagen fibres and the extracellular matrix is not modelled, in order to better reveal the viscoelastic behaviour that arises from the interaction between fluid-filled and solid phases. That said, a wide range of elastic moduli for soft tissue can be found in the literature, depending on tissue type, pathophysiological condition and details of the measurement method, for example 17.6-75.4 kPa for liver tissue [173] and 1-37 kPa for breast tissue [174], [175]. Even for a single tissue type, measured values of elastic modulus can vary considerably. For example, the measurements of Krouskop et al. (1998) on "small" excised pieces of prostate tissue, yielded values for apparent elastic modulus of 40-85kPa for normal tissue, 30-55kPa for tissue affected by BPH and 75-270kPa for tissue affected by cancer. These values were measured using sinusoidal indentation at 0.1, 1 and 4Hz using pre-strains of 2% and 4% and the fact that Krouskop et al. reported no phase difference would indicate that the relevant time constants, if any, were above 10 seconds.

Here, the solid phase is modelled using the neo-Hookean strain energy function:

$$W_D = C_1(I_1 - 3) + D_1\left(\exp\left(D_2(I_1 - 3)\right) - 1\right) \tag{5-8}$$

where C_1, D_1 and D_2 are material constants, and I_1 is the first invariant of the right Cauchy-Green deformation tensor. To derive the material constants in Eq. (5-6), the neo-Hookean model is fitted against the target elastic properties in the strain range of 0-10% (which is sufficient for the strain expected in this study), using the Levenberg-Marquardt algorithm for nonlinear least square approximation. For more details of the algorithm, the readers should refer to [176]. So, following Krouskop et al.[106], the model can be devised using a value for E from 10-100kPa with a median "benchmark" of 50kPa (i.e. $C_1 = 0.0075, D_1 = 5e^{-16}$ and $D_2 = 50$), and a Poisson's ratio of 0.49 [177]. The fluid is modelled as a slightly-compressible laminar viscous fluid [178]. The viscosity of interstitial fluid has been reported to vary with pathological condition, in the range of 1.5-

5 cP in rat mammary tumours [179] and 3.5 cP in a human interosseous membrane [178]. Therefore, in this study, the range of 1.5-5 cP was chosen for viscosity of the fluid phase, with 3.5 cP used as a benchmark value.

5.5 Formulation of numerical homogenization

All models (including those with simplified geometry and reconstructed from the histological image) were meshed in ADINA using 9-node, 2D, quadrilateral elements for the solid phase and 4-node, 2D, triangular elements for the fluid phase. As mentioned above, stress relaxation was used here to characterize the viscoelastic behaviour of the model microstructures, where a uniaxial strain was applied at strain rates ranging from 0.03 to 0.15 s^{-1} and then held constant for 5s. The temporal variation of the reaction force at the boundary where the strain was applied was recorded over time from the initial application of the strain until the end of the 5-second dwell period.

To implement the numerical homogenization for the sample histological structures, in addition to the prescribed loading condition (i.e. stress relaxation test as mentioned above), a set of prescribed boundary conditions were required. Without loss of generality confined boundary conditions, often used in numerical homogenization scheme for tissue mechanics, were used here [114], [180], as illustrated in Fig. 5-2. For the solid phase, the displacements were constrained along the normal direction for each boundary. For the fluid domain, open boundary conditions were used at the outlets allowing both inflow and outflow, depending on the pressure profile in the channel during relaxation. This effectively mimics fluid exchange with the surrounding tissue.

5.6 Characterization of viscoelasticity

A Prony series was used to fit to the reaction force relaxation profile, Eq 2.15 can be written as[181],

$$F(t) = E\left(1 - \sum_{i=1}^{n} P_i(1 - e^{-\frac{t}{\tau_i}})\right) \tag{5-9}$$

where F denotes the normalized reaction force (i.e. force feedback divided by the peak force), E the instantaneous stiffness, P_i the stiffness of Maxwell elements and τ_i the time constants. For simplicity, a two term Prony series (i.e. n= 2) was used so that P_1 and P_2 are, in effect, weighting factors for the two time constants. It is important to note that these time constants have a considerable influence on the effectiveness of fitting at the instantaneous and long-term extremes of the relaxation curve. It is also worth highlighting here that, although the duration of load application varies with the strain rate, the same relaxation period (i.e. time that material is held under the certain displacement) of 5s was considered in all tests. It should be noted that 5s is chosen based on the consideration of patient comfort during digital rectal examination[182].

5.7 Parametric study using simplified channel models

This section considers the effect of strain rate and structure on the relaxation response of the parameterized models illustrated in Fig. 5-2. As an example, the time evolution of reaction force in Model 1a is shown in Fig. 5-3 for each of the strain rates using the benchmark values of fluid viscosity and modulus of the solid phase. Figure 4a shows the force response including the application of the prescribed strain of 3%, during which the fluid channel is compressed leading to increased pressure therein, which in turn increases the reaction force. It can be seen that using a higher strain rate leads to a higher peak force at 3% strain, due to the more rapid increase of pressure in the channel. This is akin to the viscous term in viscoelastic material models where the viscous stiffness is given by $F_v = \eta\dot{\delta}$, where η is the viscous damping coefficient (N·s·mm^{-1}) and $\dot{\delta}$ is the displacement rate. For the purposes of obtaining a single force response parameter, the 5s period of stress relaxation was represented with respect to the peak force, giving the normalized decay curves shown in Fig. 5-3(b). Two-term Prony series were then used to fit the normalized relaxation curves, which was generally achieved with an R^2 value of better than 0.99. Although a single-term Prony series generally will bias fitting of exponential-shape curves towards either instantaneous or long term behaviour, this was accepted here in the interests of clarity of interpretation. For all the fits here P_2 was significantly greater than P_1 (the weighting factor on instantaneous behaviour), highlighting the importance of τ_2, the time constant for long-term behaviour (in the 5-second range). Thus τ_2 will be used alongside the peak force, F_p, as the key indices of force response in the parametric comparison in the following sections.

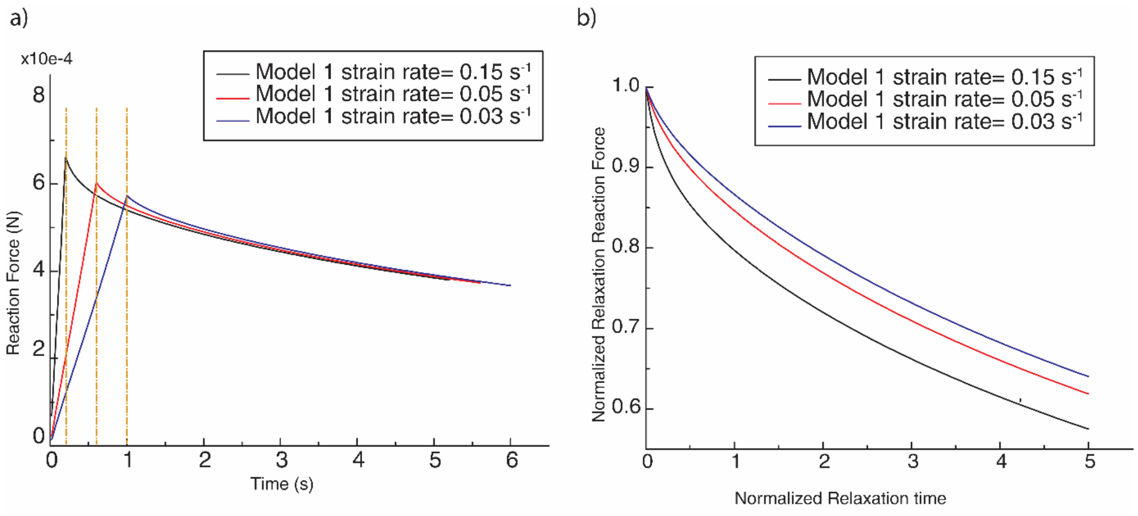

Figure 5-3. Evolutions of reaction force for different strain rates. Model 1a is used here as an example. (a) Three strain rates are used, leading to different loading and stress relaxation profiles. (b) Normalized stress relaxation curves, which are then fitted with two-term Prony series.

5.8 Microstructure

This section examines the influence of the channel geometry (as classified in Fig. 5-2) on the resulting apparent viscoelastic behaviour. Fig. 5-4 shows the effect of strain rate and geometry on peak reaction force F_p and (long) time constant τ_2 using the benchmark values assigned to the fluid viscosity and elastic modulus of the solid phase. As can be seen, the peak force generally increases and the apparent time constant generally becomes smaller (i.e. faster stress relaxation) when the strain rate increases. The peak reaction force (Fig. 5-4(a)), is significantly greater in Model 2 than Model 1. More interestingly, the effect of a change in the amplitude parameter on peak reaction force is different for the two models; in Model 2, the peak force increases significantly for low strain rates, less so at higher strain rates, whereas in Model 1 the peak force increases only slightly with amplitude at low strain rates and decreases with amplitude at higher strain rates. Part of the explanation for this can be seen from the pressure profile in the fluid channel at the time of peak force, as illustrated in Fig. 5-5. At smaller values of H, as in Figs. 5-5(a-b), the relatively flat channel leads to a monotonic gradient in pressure from the centre of the track of the channel to either side. In contrast, at larger values of amplitude, as in Figs. 5-5(d-e), a localized low pressure region appears, associated with the change in the channel curvature. The effect of the internal channel pressure on the Y-component of the reaction force (F_y) across the top of the model is shown in Figs. 5-5(c) and (f), for Models 1 and 2 at the extremes of low amplitude and low strain rate, and high amplitude and high strain rate, respectively. It is clear that the effects of amplitude and strain rate are less pronounced at the low pressure areas where the curvature of the channel is changing.

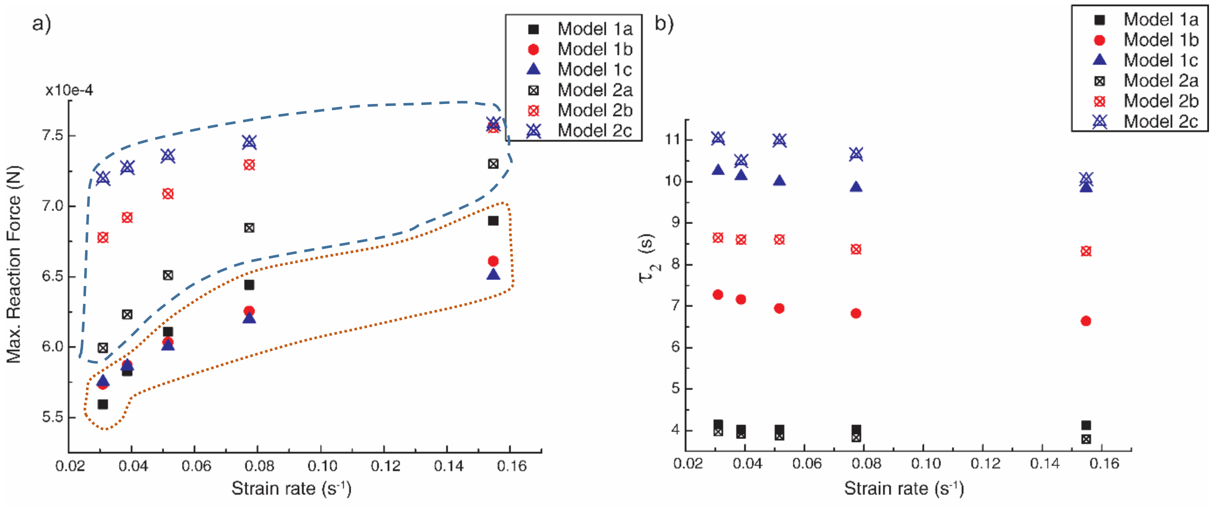

Figure 5-4. Effect of geometry and strain application rate on (a) maximum reaction force and (b) (long) time constant.

In summary, for values of fluid viscosity and tissue modulus typical of prostate, longer channel length and greater channel tortuosity will lead to higher resistance in fluid movement within the channel, hence slower relaxation. This highlights the significant potential of tissue viscoelasticity to serve as a diagnostic index of histological structure; even using relatively simple parameters such as the peak reaction force and the apparent time constant in a press-hold test the interactions between the solid and fluid phases give rise to distinctive profiles of reaction force.

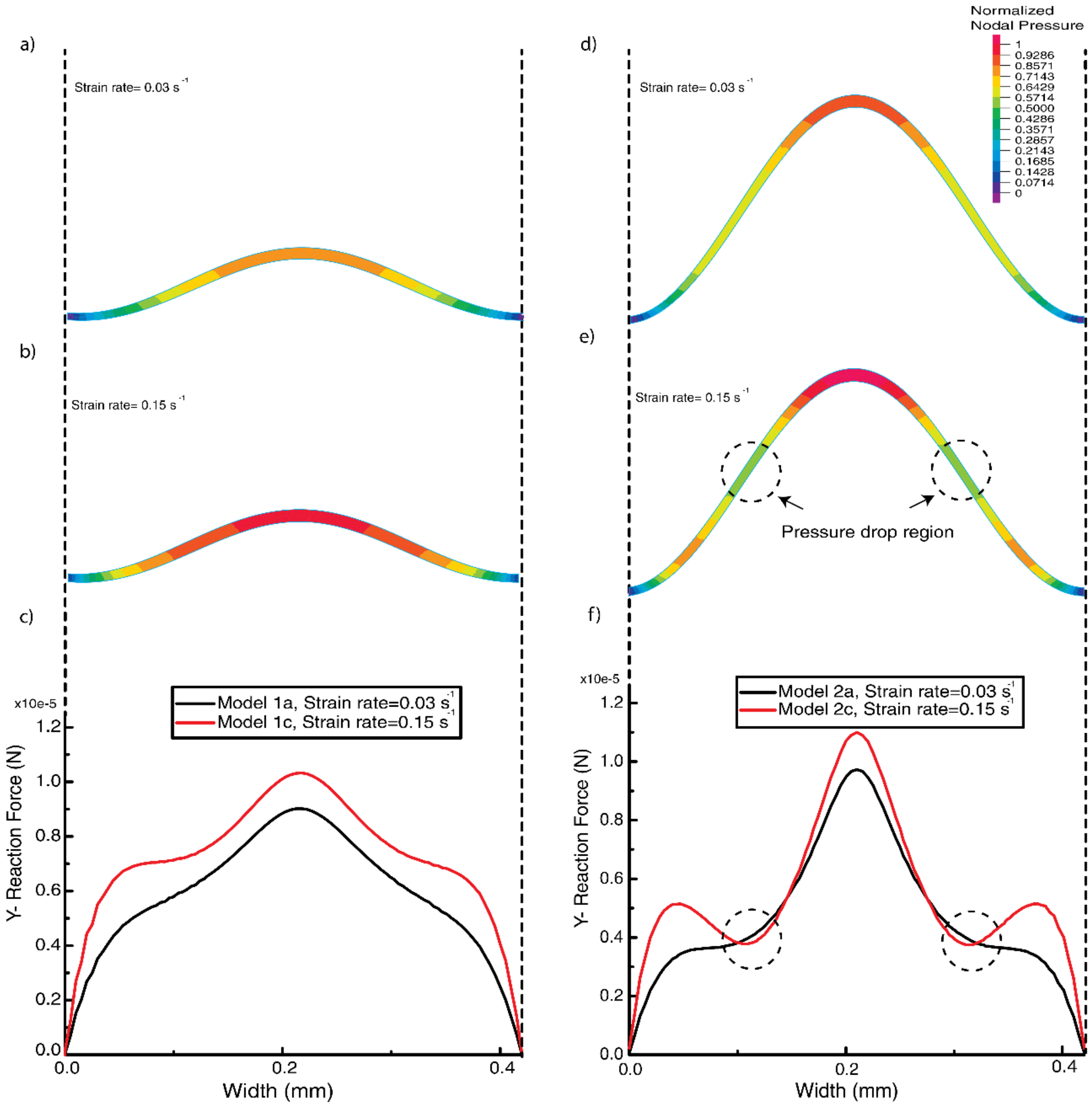

Figure 5-5. Relationship between pressure distribution and reaction force. Pressure distribution in fluid channel, for Model 1a, with (a) high 0.15 s-1 and (b) low 0.03s-1 strain rates, and for Model 1b with (d) high and (e) low strain rates, respectively. Comparison of Y-component of forces exerted by the fluid pressure onto the solid phase with low and high strain rates for Model 1 (c) and Model 2 (f), respectively.

5.9 Effect of component properties

Having established the influence of channel geometry for benchmark properties, this section is concerned with the effects of the properties fluid viscosity and elastic modulus, over the ranges identified in Section 5.6. The values of viscosity used were 1.5, **3.5** and

5cP and, for modulus, 10, **50** and 100kPa, the numbers in bold being the “benchmarks” used in Section 5.4. To reduce the number of geometric variables, only the middle channel amplitude is used here, i.e. Models 1b and 2b. Fig. 5-6 shows the effect of viscosity on peak force and (long) time constant. As already seen in Fig. 5-4, increasing the strain rate results in a higher peak force and a lower time constant, and Model 2 gives higher reaction forces and longer time constants for a given viscosity and strain rate. As might be expected, the viscosity of the fluid has a significant effect on the apparent viscoelastic behaviour, a higher viscosity both increasing the peak force (Fig. 5-6(a)) and the time constant (i.e. slower relaxation) (Fig. 5-6(b)). Although applied to the viscosity of the interstitial fluid (rather than to luminal fluid here), this is consistent with the findings of Parker [68].

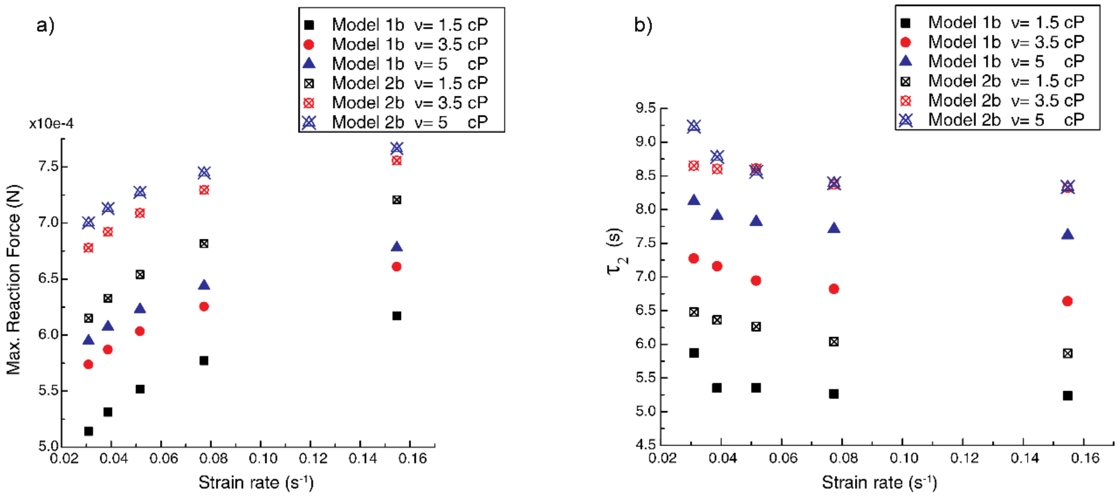

Figure 5-6. Effect of fluid viscosity (ν) on evolution of maximum reaction force (a) and time constant (b) with strain rate.

Fig. 5-7 shows the effect of elastic modulus on peak force and time constant, again for Models 1b and 2b over the range of strain rate used previously and using the benchmark viscosity. Again, increasing the strain rate results in a higher peak force and a lower time constant, and Model 2 gives higher reaction forces and longer time constants for a given modulus and strain rate. However, the strain rate dependence of peak force is less the lower the modulus and changes of modulus have a much stronger effect on peak force and a much weaker effect on relaxation time than do changes in viscosity. During the loading stage of the stress relaxation test, a softer solid phase is less capable of effectively ‘discharging’ the fluid from the channel, leading to a lower apparent peak force (Fig. 5-7(a)) and a slower relaxation (i.e. higher time constant) afterwards (Fig. 5-7(b)).

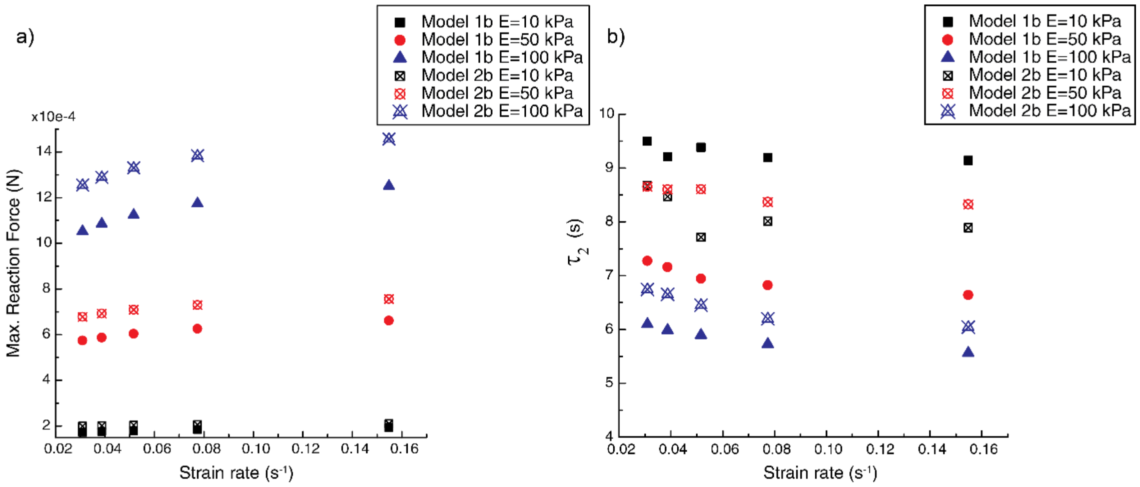

Figure 5-7. Effect of solid phase modulus (*E*) on evolution of maximum reaction force (a) and time constant (b) with strain rate.

Overall, these results indicate that using the elastic or viscous behaviour alone may not be sufficient to gain a deep understanding of the underlying microstructure. This would be of critical significance in clinical practice where such knowledge would lead to more accurate diagnosis. It can be seen that using both elastic and viscous indices would result in an enhanced description of tissue quality.

5.10 Concluding remarks

This study sets out to provide a framework for quantifying the contribution of fluid-solid interaction within the tissue microstructure to its apparent viscoelasticity. Such contribution would be additional to what has been traditionally believed to be the source of viscoelasticity (the intrinsic viscoelasticity of the tissue solid phases such as collagen fibres and proteoglycans), and could be used to take into account the heterogeneous and multiphasic nature of tissue when attempting to characterise the effective properties of tissue microstructure. Such an approach could aid diagnosis of conditions where the fluid-containing structures are known to be significantly affected in size, morphology and distribution. The proposed computational framework quantified the influence of various shape and morphology of the fluid-containing elements, fluid viscosity and modulus of the “solid” phase. As an example of a disease condition, two ROIs were extracted from a histological section affected by prostate cancer. Illustrative results based on the parameterized channel models showed that more complex fluid channels would lead to higher peak reaction forces and slower relaxation. Curvature of the fluid channel, at the microstructural scale, could significantly affect the pressure distribution of the fluid and consequently the apparent viscoelastic behaviour of tissue. The viscosity of the fluid and the modulus of the solid phase, were also shown to be critical in affecting the apparent viscoelasticity of tissue, their effects are as one would expect from “spring” and “dashpot” elements of an analytical viscoelastic model. Representative microstructural models reconstructed from a histological section of example regions of benign and malignant prostatic tissue were used to demonstrate the feasibility of the proposed method when a more complex geometry of tissue microstructure is present. Results illustrated that the variations in tissue morphology associated with prostate cancer lead to significant changes in tissue viscoelasticity. The proposed method captures the multiphasic and multiphysical nature of tissue microstructure and can therefore, in principle, be used for various types of tissue such as prostate, breast and liver. This would allow a more quantitative understanding of how changes in tissue morphology in disease lead to variations in tissue viscoelasticity. Such understanding could be used in conjunction with, for example, novel palpation-based diagnostic devices [32], [56] and more established techniques, such as elastography [35] and multi-parametric MRI [183] for enhanced clinical diagnosis.

CHAPTER 6

Viscoelasticity in Prostate Tissue – Histology-based Fluid-Structure Interaction Modelling

Contents

6.1 Summary

The mechanical properties of soft tissues are known to evolve subject to various factors, such as mechanobiological response to mechanical stimuli, ageing process, and progression of the disease. Various pathological conditions have shown to influence tissue microstructure which subsequently influences its functionality. Taking prostate tissue as an example, branching duct–acinar glandular tissue with regular microstructures

can be found in healthy prostate, whilst in prostate cancer, such structures often consist of tightly packed cells and irregular stromal tissue in unrecognisable patterns. The drastic changes in tissue microstructure could result in disruption of the fluid movement in the glandular structures, leading to certain changes in the mechanical properties of tissue, particularly viscoelasticity. The previous study has shown that the apparent diffusion coefficient in prostate decreased in cancerous tissue due to the reduction in diffusivity of fluid as a result of tissue morphological changes[184]. Similarly, it has also been reported that the relaxation time and elasticity, in liver tissue, increase due to a reduction in the size of fluid channel which, again, leads to the restriction of fluid flow[68]. These findings have suggested a close relationship between fluid movement in the tissue microstructure and its mechanical behaviour (e.g. time dependent one such as viscoelasticity). This needs to be quantified in order to gain a better understanding of the mechanics of tissue.

This chapter presents a computational framework for quantitatively assessing the contribution of fluid movement to the viscoelastic behaviour of tissue due to morphological changes, using prostate as an exemplar tissue. Viscoelastic characterization is performed by incorporating the fluid-structure interaction in the framework of numerical homogenization, on representative acinar structures of prostate tissue for both non-cancerous and cancerous tissues subject to stress- relaxation test. Not only would this work quantify the contribution of fluid movement to the tissue viscoelasticity, it would also examine such relationship in cancerous tissue for the purpose of tissue quality assessment and diagnosis.

6.2 Histology and image processing

Prostate tissue is chosen here as an exemplar to demonstrate the feasibility of the proposed methodology, although the approach is generic and can be applied to any soft tissue that has histologically identifiable elements that are fluid-filled and interact with their ‘‘solid’’ counterparts. The prostate structure can be described as having two components; the “solid” stromal tissue and the fluid-filled glandular tissue (Fig. 6-1).

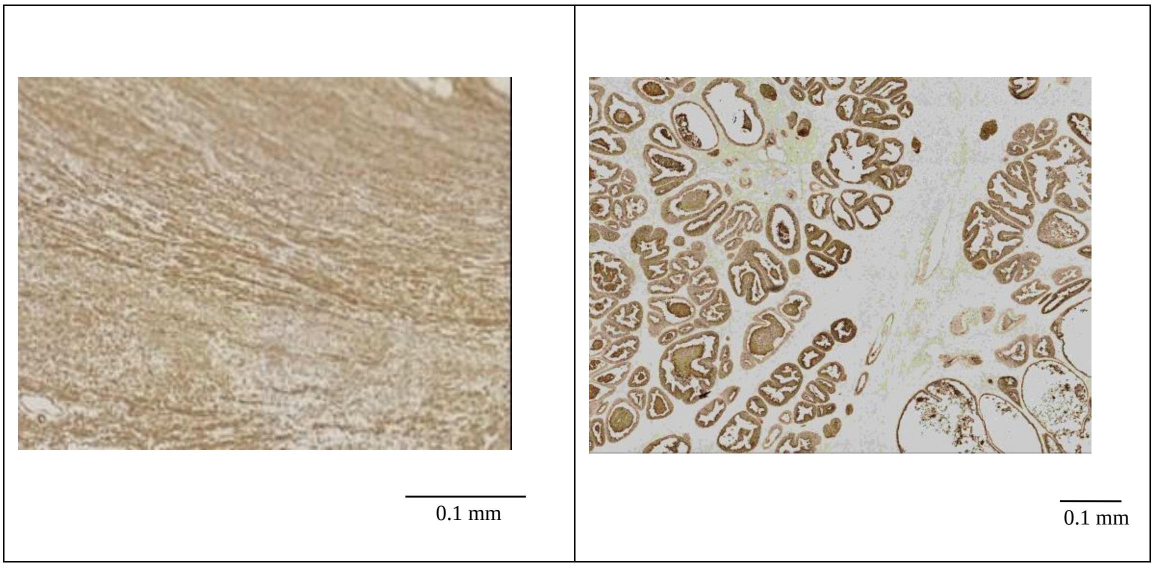

Figure 6-1. The two main histological components of prostate tissue. Left, “stromal”, consisting mostly of connective tissue, smooth muscle cells and fibroblasts, stained with anti-smooth muscle antibody. Right “epithelial”, consisting of glandular acini, lined with epithelial cells, stained with anti-PSA antigen.

Leaving aside the complication that the glands are surrounded by epithelium cells and that the stroma contains interstitial fluid and is, in itself, viscoelastic, this simplified model can be usefully deployed as it is well-established that the stromal/glandular morphology is affected by a number of pathological conditions, most notably prostate cancer [185] and benign prostatic hyperplasia (BPH) [12], and that the morphological changes can be detected mechanically [32], [185]. Moreover, these morphological changes are manifest, in cancer, to a varying degree according to severity using a system originally devised by Gleason[168], which characterizes the extent to which the glandular component of the prostate tissue has become undifferentiated.

Samples of prostatic tissue were extracted from an image of a histological slide of a patient, who has been diagnosed with acinar adenocarcinoma and with Gleason score

3+4. The histological slide stained with hematoxylin and eosin (H&E) is shown in Fig. 6-2(a), and an example of the microstructure of the cancerous tissue in Fig. 6-2(b). In prostate cancer, tissue morphology changes and the glandular structures therein exhibit poorly formed acini in diffuse patterns with agglomeration of epithelium cells [168]. Ten representative acinar structures (in an equal number of cancerous and healthy samples, in representative 'regions of interest', ROIs) obtained from the histological image as shown in Table 6-1, will be used for the computational study. The images were converted into grey scale and segmented in Scan-IP (Simpleware, Exeter, UK), firstly by a greyscale filter using a threshold of 160 (i.e. 0-160 for the 'solid' tissue phase and 161-255 the acinar fluid), and then filtered by an 'island' isolation algorithm to remove the acinar space that is not directly connected to the main structure (e.g. white pixels at the centre), as shown in Fig. 6-2(c). Finally, a boundary smoothing technique is applied[186], which preserves the area fraction of the fluid phase while generating smooth boundaries of fluid channels, making all the tissue samples suitable for fluid-structure interaction analysis (details are given below).

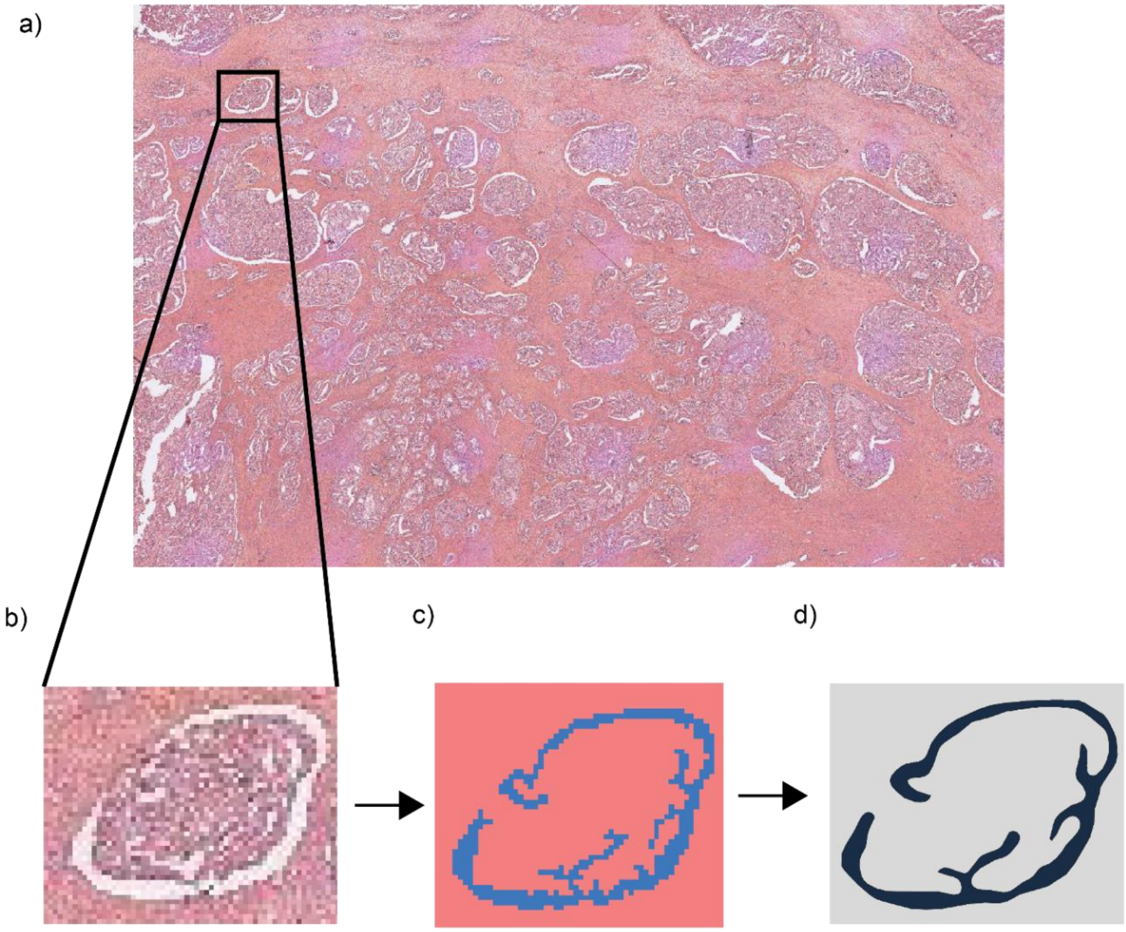

Figure 6-2. From tissue histology to computational models. a) Cancerous region of prostate tissue histology. (b) an ROI of cancerous sample; (c) Image processing performed in Scan IP Simpleware using methods described above; and (d) The computational model prepared for FSI.

Table 6-1. The dimensions and structures of chosen ROIs for both cancerous and non-cancerous samples. Red circles denote the fluid outlets at the ROI boundary.

Samples	Dimension (mm)	Histology	Model
Cancer – No. 1	0.747 × 0.603		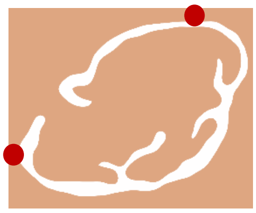

Cancer – No. 2	0.764 × 0.630		
Cancer – No. 3	0.495 × 0.469		
Cancer – No. 4	0.536 × 0.510		
Cancer – No. 5	0.764 × 0.844		
Non-cancer No. 1	0.536 × 0.469		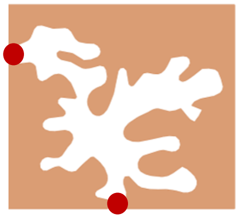
Non-cancer - No. 2	0.509 × 0.509		

Non-cancer - No. 3	0.295× 0.375		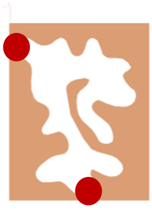
Non-cancer – No. 4	0.469 × 0.295		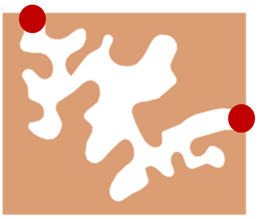
Non-cancer – No. 5	0.348 × 0.322		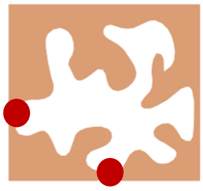

6.3 Modelling of fluid-structure interaction

The simulation of fluid-structure interaction is performed on all chosen ROIs, within a framework of numerical homogenization (discussed later), in order to quantify the viscoelastic response of prostatic tissue subject to stress relaxation, due to the movement of acinar fluid in the tissue microstructures.

In this study, slightly-compressible fluid flow model is used to account for changes in fluid density despite the relatively low fluid velocity. In slightly compressible flows, density depends only on pressure, as

$$\rho = \rho_0(1+\frac{p}{k}) \tag{6-1}$$

where ρ is the fluid density with the compressibility and ρ_0 is the density at $p = 0$. The conservative form of continuity equation remains the same as that in the general case.

The non-conservative form of the continuity equation in slightly compressible flows can be written as[187]

$$\frac{\rho_0}{k}\left[\frac{\partial p}{\partial t} + \mathrm{v}\cdot\nabla p\right] + \rho\nabla.\mathrm{v} = 0 \tag{6-2}$$

where k is the fluid bulk modulus of elasticity and ρ_0 the density at pressure p = 0. The density of fluid component q is assumed as ρ = 1000 kg/m3 with the bulk modulus of k = 2200 MPa and viscosity ʋ = 3.5 cP [178]. Equivalent elastic modulus of 50 kPa is used in this study a Poisson's ratio of 0.49[177], to which the neo-Hookean model is fitted as discussed in chapter 5.

To characterise the viscoelastic properties, stress relaxation is applied to each RoI model, which undergoes an uniaxial deformation with an equivalent strain of 3%, carried out in various duration hence various strain rates, followed by stress relaxation under sustained strain at 3% strain for 6s. Similar to chapter 5, Prony series[69] are used here to characterise time-dependent stress profile resulted from the relaxation test, which is obtained from average of effective stress (e.g. Von Mises) over all integration points of the solid phase Formulation of numerical homogenization.

All models of ROIs are meshed in ADINA (ADINA R&D Inc., MA, USA) using 4-node triangular elements for the phase of acinar fluid and 9 nodes quadrilateral elements for ‘solid’ tissue phase. As mentioned above, stress relaxation is used here to characterise the viscoelastic behaviour of the chosen tissue microstructures, where a uniaxial strain of 3% is applied and then kept constant for a duration of 6s. To better understand the influence of the direction of loading and the degree of anisotropy of the tissue microstructure, each sample was subject to two, i.e. vertical and horizontal, uniaxial stress relaxation tests. In addition, an ALE (Arbitrary Lagrangian Eulerian) algorithm is used to account for fluid mesh deformation, in which the moving boundaries were tracked using the Lagrangian approach and the stationary boundaries by Eulerian approach. As mentioned above, stress relaxation profile over time is obtained by averaging the effective stress of all integration points across the entire solid phase in each ROI. To implement the numerical homogenization, a set of prescribed boundary conditions are used [114], [180], as illustrated in Fig. 6-3. For the solid phase, symmetry boundary conditions were used on two sides of the solid models, whereas for the fluid domain opening boundary conditions are used at the boundary of ROIs, allowing both inlet/outlet flow depending on the pressure profile in the acinar channel compared to the reference pressure (equivalent to the initial pressure in the channel prior to the application of loading, to mimic the far-field interstitial pressure), which allows the fluid exchange (although not modelled explicitly) with the surrounding tissue environment. It should be noted here that, since it is not possible to directly acquire the 3D structure of acini (i.e. off the histological plane), it is hypothesised that each acinar structure modelled has two ‘outlets’ that connect to the external channel network. The position of the outlets is chosen based on the least manipulation in the acini structures (i.e. close to the boundary of the ROI), with the condition of existence of one outlet in each side of the ROI. It should be noted that due to the nonlinearity of the geometry the results may vary by changing the outlet location. The width of the outlets is chosen by using the averaged diameter of all fluid channels measured from 50 points along the channel within of the ROI and it was found to be 4.19 µm for non-cancerous samples and 3.29 µm for cancerous samples, respectively.

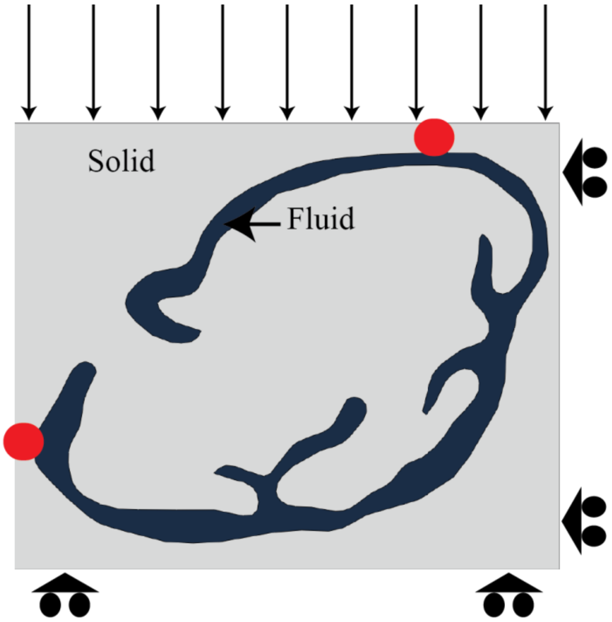

Figure 6-3. The symmetry conditions are applied for solid boundaries, and the red circles denote the fluid outlets at the ROI boundary.

6.4 Results and Discussion

Based on the parametric study presented in chapter 5, the feasibility of the proposed methodology is further demonstrated here using models reconstructed from the tissue histology. The two representative ROIs (i.e. Non-cancer/Cancer – No. 1) illustrated in Table. 6-1, were reconstructed to consist only of solid and fluid phases in order to be compatible with the simplified channel models, although with more complex and realistic tissue microstructure. Again for simplicity and to be compatible with the parametric study of geometry, only the benchmark values were used for the viscosity of the interstitial fluid and modulus of the solid phase. The configurations used in the numerical homogenization remained the same and five strain rates, ranging from 0.03 to 0.15 s^{-1}, were used. In this section, the stress relaxation curves are presented (in Fig. 6-4) alongside maximum average stress in the element as the reaction force curves could be confused by the fact that ROIs are of different sizes.

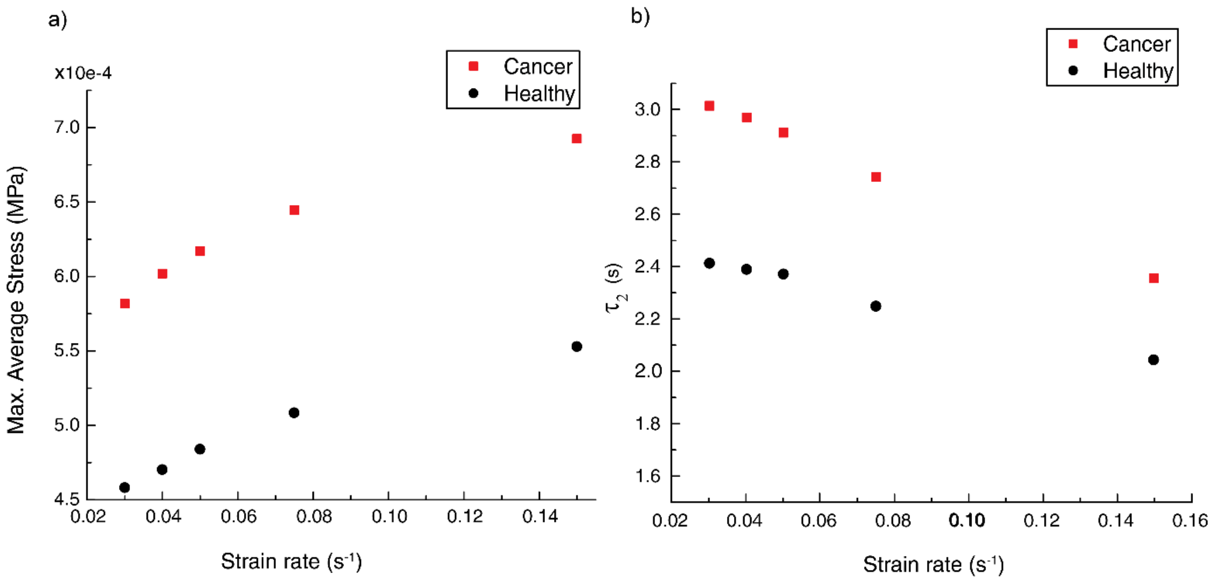

Figure 6-4. Evolutions of maximum average stress and the time constant of both histology-based models subject to increasing strain rate.

From Fig. 6-4(a) it can be seen here that, for both cancerous and non-cancerous ROIs, the peak stress increases when the strain rate becomes higher, and, significantly, that the cancerous model has a higher peak stress than the benign one at all values of strain rate, consistent with much of the published literature. The apparent time constants for both models, as shown in Fig. 6-4(b), reduce with increasing strain rate, the malignant ROI exhibiting a higher time constant, hence a slower relaxation, than the benign one. As for the channel models discussed previously, it seems that the complexity of the tissue microstructure in the cancerous ROI hinders the fluid movement, leading to a slower relaxation. In this regard, it can be seen that the microstructural changes in tissue have significant impact on the apparent viscoelasticity of tissue. It is worth highlighting here that considering only the peak reaction force (stiffness in the sense of elasticity) might not be enough as an effective diagnostic index, and that this could be enhanced by taking into account the viscous behaviour, for example in the form of a time constant. Such conceptualization of the structure-property relationship could enhance the interpretation of diagnostic approaches such as instrumented elastography and palpation [45], [70].

Furthermore, probing tissue dynamically at a range of frequencies could help to reveal processes going on at a range of length scales. Such viscoelastic behaviour could be linked to different biological features such as density and size of acini, which have been related to different Gleason scores for diagnosis of prostate cancer. The method could also be applied to other diseases, such as fibrosis and steatosis of the liver and breast cancer [188].Fig. 6-5 shows the normalised stress profile during relaxation, using the peak value of average effective stress at the start of the relaxation, for non-cancerous and cancerous tissue samples, respectively. The differences between vertical and horizontal directions of stress relaxation are compared in Fig. 6-5(a-b) for non-cancerous samples and Fig. 6-5(c-d) for cancerous samples. It is shown that, at the length scale of the chosen ROIs (i.e. single acinar structures), a certain degree of anisotropy can be observed. However, since the orientation of the acinar structures has no obvious preferential direction (i.e. having a random orientation) in the entire tissue microstructure, such anisotropy is expected to gradually reduce when the size of RoI increases (i.e. at higher length scales). It can also be seen that in most non-cancerous samples the relaxation reaches steady state within 6s. However, this is not the case in most cancerous samples, indicating rather different relaxation characterizations. This indeed shows the influence of narrower channels in the cancerous samples, leading to less capacity of fluid movement, in comparison to the non-cancerous ones. Interestingly, some fluid channels are observed to close during the loading stage (data not shown) due to deformation of the solid structure, leading to possible reduction or even blockage of local fluid movement. Those channels restore their original sizes during stress relaxation, indicating the re-establishing of the flow path while the fluid pressure in those channels stabilises. Such phenomenon, although not revealed in prostate tissue before, has been previously reported in brain tissue showing increased hydrostatic pressure in tissue during confined compression test and fluid dissipation over time during stress relaxation [65].

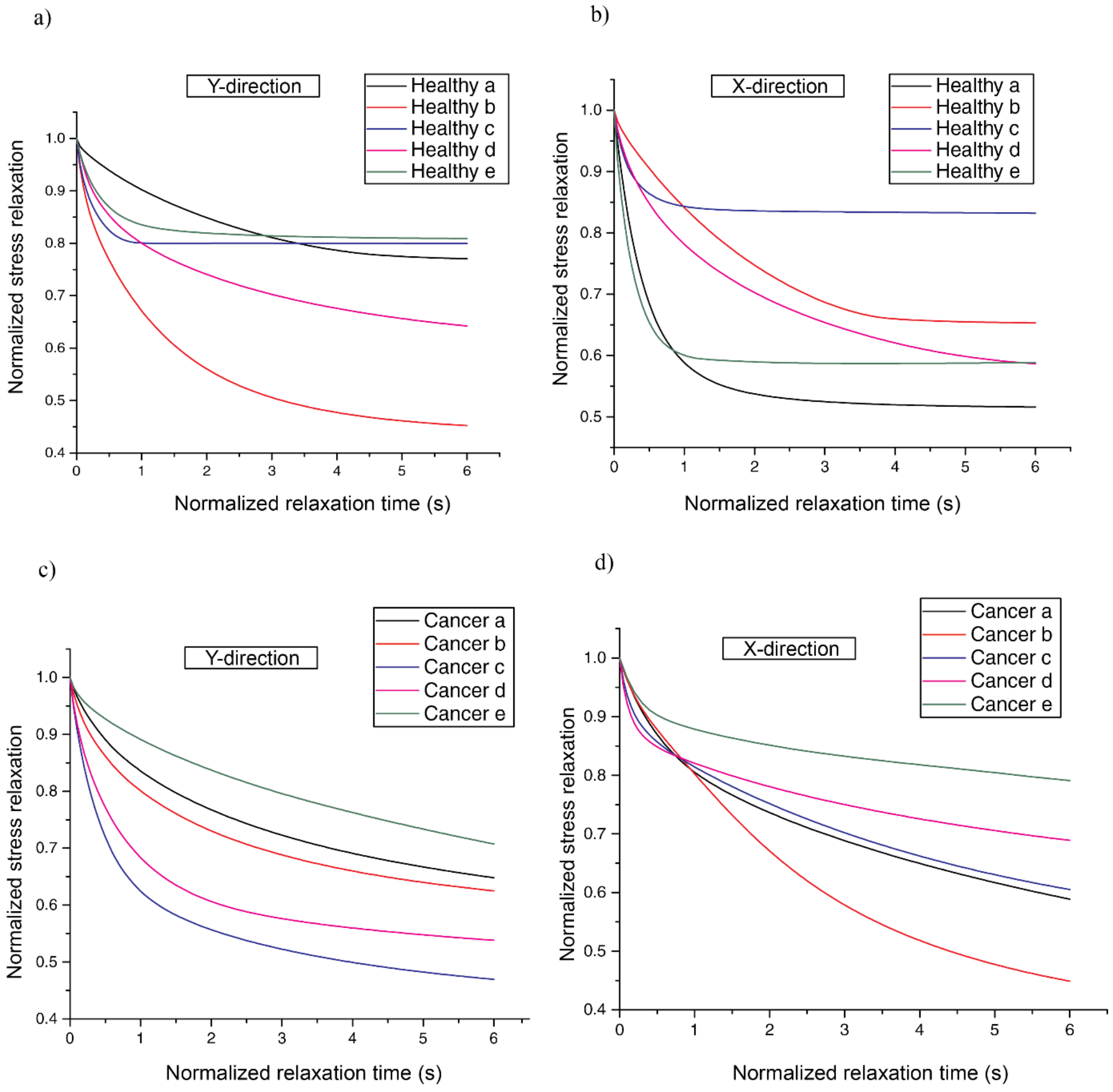

Figure 6-5. Normalised stress relaxation curve for both healthy and cancerous samples in vertical (a,c) and horizontal (b,d) directions respectively.

Fig. 6-6 shows the instantaneous (E_0) and long-term (E_{inf}) moduli along the vertical (x) and horizontal (y) axis of cancerous and non-cancerous samples, respectively. The average E_0 in cancerous samples is higher than those non-cancerous ones, which is in line with the experimental data of the elastic modulus of prostatic tissue under compression that has been previously reported[106]. These results, again, show variations of both moduli between two principal directions, highlighting a certain degree of anisotropy at the length scale of the chosen ROIs. It should also be noted that, comparing box sizes (i.e. distribution of 25%-75% quartile) in two horizontal and vertical directions, in the case of the cancerous tissue the difference is higher which can be linked to the less organised tissue morphology[166]. In cancerous tissue, the channels are narrower, therefore, blockage of fluid movement makes the tissue appear to be stiffer when compressed. On the other hand, for long-term moduli, the average does not show a significant difference between two groups of samples. This can be due to the fact that equilibrium state of the hydrostatic pressure is reached in most samples at the end of the 6s relaxation.

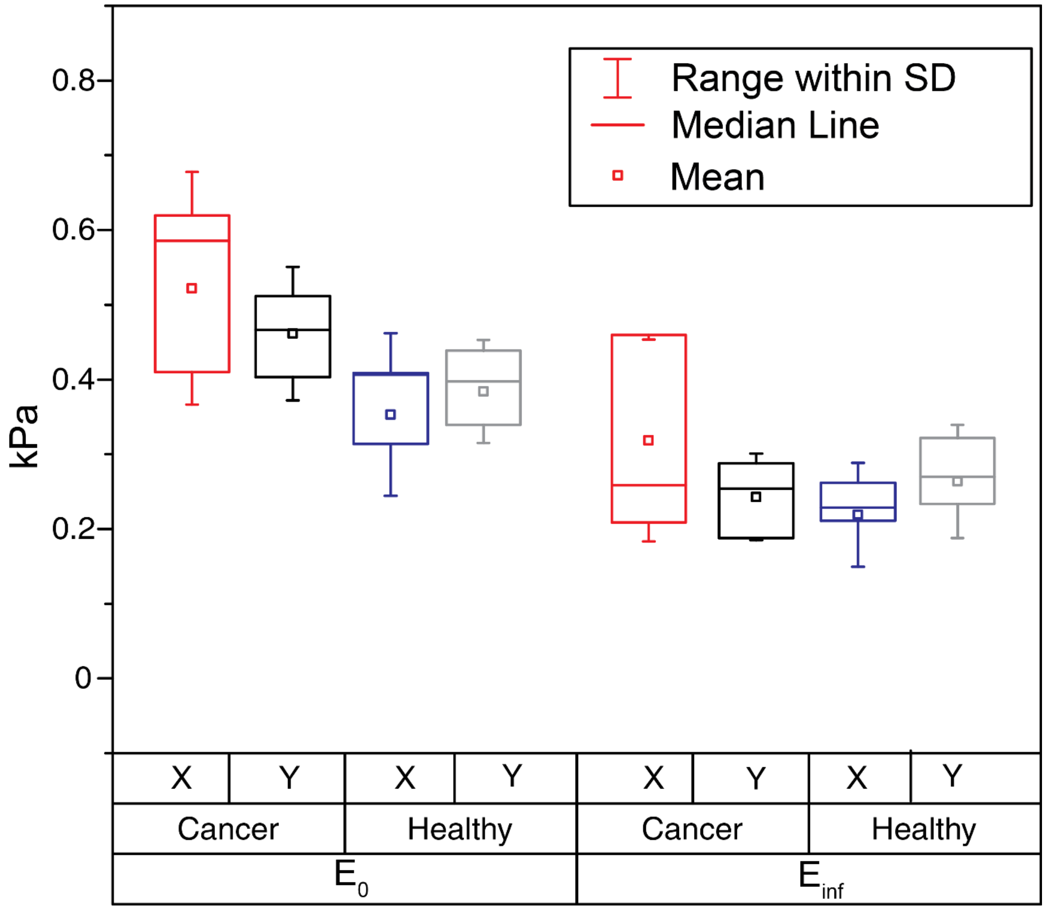

Figure 6-6. Statistics of instantaneous (E_0) and long-term (E_{inf}) moduli of all RoI chosen, for both directions. The boundary of box chart shows 25% -75% quartile.

Fig. 6-7 shows the values of two time constants, τ_1 the short term and τ_2 the long term, obtained from fitting normalized stress relaxation curves with two term Prony series in Eq. (3), for cancerous and non-cancerous samples, respectively. It is noted that τ_1 shows little difference between two groups of tissue samples. On the other hand, τ_2 is significantly higher in cancerous samples, meaning slower stress relaxation. This could be due to the complex morphology (i.e. channel topology) in cancerous tissue in which the fluid is not capable of moving freely in the channels during the relaxation. On the contrary, in non-cancerous samples the, tissue microstructure has wider and more open channels leading to greater capacity of fluid movement. It is evident that the microstructural changes in prostate cancer, which could be correlated to their Gleason score (i.e. morphological indices), could influence its apparent viscoelastic behaviour. Therefore, it is envisaged here that viscoelastic analysis of prostatic tissue could provide critical information of the pathological conditions of the tissue and may be used as a diagnostic index for tissue quality assessment.

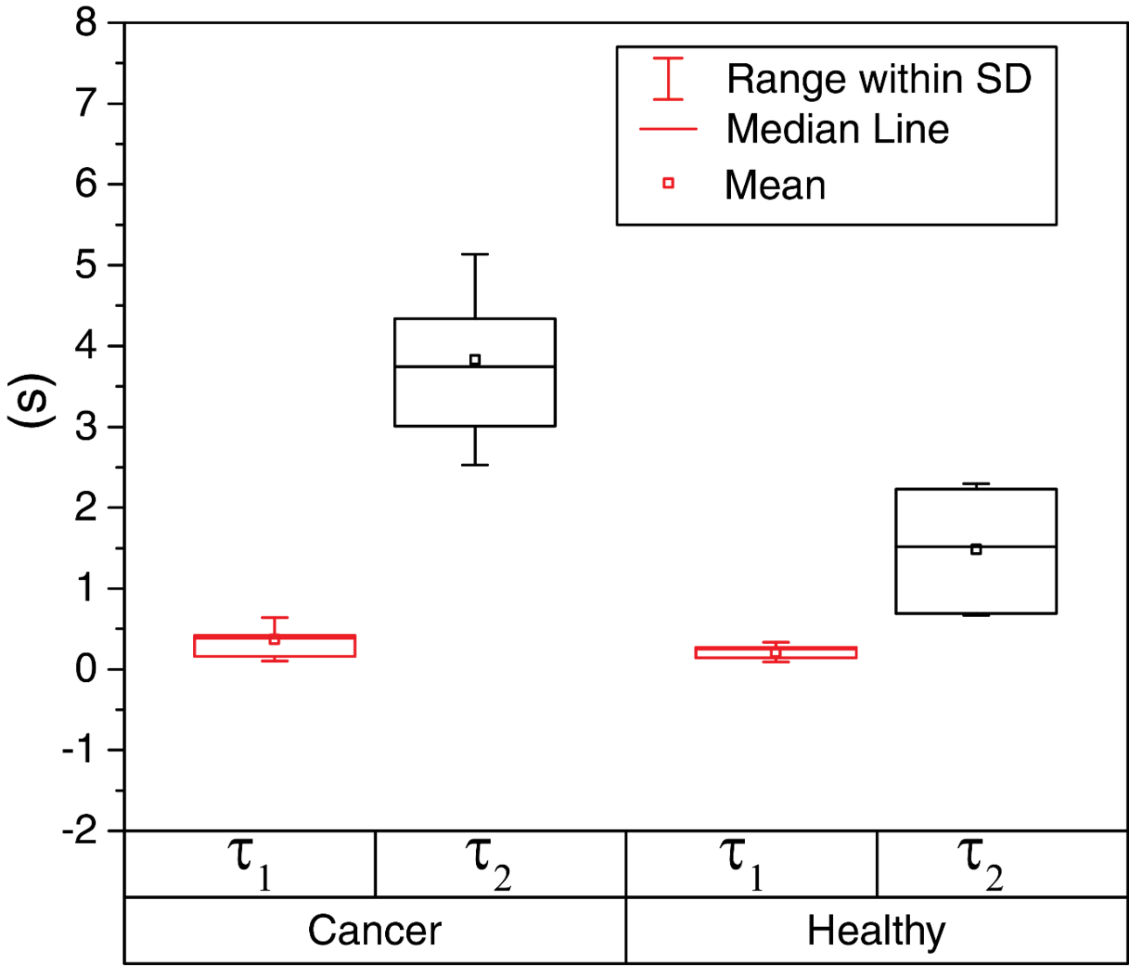

Figure 6-7. Fitting of stress relaxation profiles using two-term Prony series, for cancerous and non-cancerous samples.

Resistance to fluid movement could be another parameter which emphasizes the interaction of fluid with solid tissue structures and its correlation with viscoelasticity. Resistance to fluid movement in the fluid domain is calculated following the Poiseuille's law [189], as

$$R_F = \frac{\Delta P}{Q_V} \tag{6-3}$$

where ΔP is average of pressure difference (i.e. during the relaxation) of all nodes in fluid domain and Q_V the volumetric change of the fluid domain. Although this formulation is simplified and applies only to steady, laminar flow through rigid pipes, Poiseuille’s law has been used in analysis of respiratory[190], cardiovascular[191]and other physiologic flows[192], and is employed here in order to gain an quantitative understanding of how the capacity of fluid movement changes with respect to the evolving tissue microstructure. Fig. 6-8 shows the flow resistance (R_F) calculated from Eq. (6-4) for all tissue samples. It can be seen that R_F is higher in cancerous samples which could be, again, as already discussed above, attributed to the differences in tissue morphology leading to reduced capacity of fluid movement therein. In the case of an idealised cylindrical pipe, the value of R_F is proportional to the length of a pipe and inversely proportional to its radius (to the forth power). In prostate cancer, cells proliferate irregularly giving rise to the drastic changes in the acinar structures[168], leading to narrowed channels and more complex channel topology thus higher flow resistance, which could be also the reason why higher apparent diffusion coefficient was observed in other studies[184], [193]. Parker [68] has observed increase of tissue stiffness by performing a compression ex-vivo test on liver tissue samples which have been swelled from hypotonic saline; swelled samples cause the constriction of fluid channels which therefore results in increase of fluid resistance. Nevertheless, the relationship clearly shows the higher value of R_F is in line with the higher time constant τ_2 for stress relaxation in cancerous samples which has been shown previously in Fig. 6-7. This demonstrate the link between fluid flow resistance and viscoelasticity due to narrowed or even blocked channels subject to compressive deformation of the solid tissue structure, which reduces the fluid moving capacity thus leading to localised increase in the fluid pressure. This confirms that the fluid movement in prostate tissue contributes to the apparent tissue viscoelasticity, since it is the only source of viscoelasticity (the intrinsic viscoelasticity of tissue components is not modelled here).

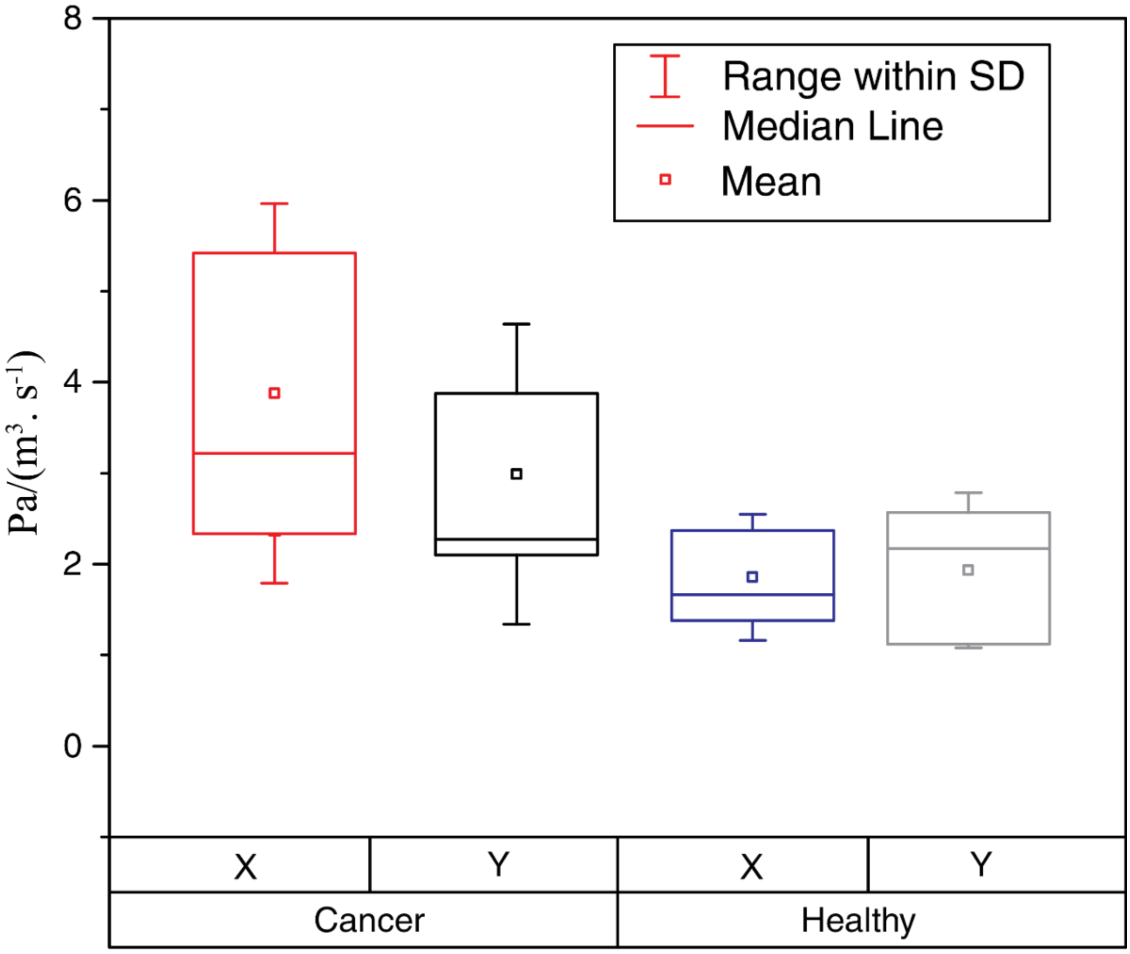

Figure 6-8. Fluid resistant $R_{F,}$ calculated for all chosen ROIs, for both cancerous and non-cancerous samples.

6.5 Concluding remarks

This chapter aims to study the effects of histology-specific features, e.g. cancerous and non-cancerous of prostatic tissue. This study provides an insight into previously stablished framework in order to quantify the contribution of fluid movement in tissue viscoelasticity. The following key findings are highlighted below:

- Micro-morphological changes due to the certain pathological condition of tissue influences the viscoelastic response of the tissue.

- Viscoelastic parameters (e.g. time constant, instantaneous (E_0) and long-term (E_{inf}) moduli) could provide more accurate information about the tissue condition and therefore can be used as indices for tissue quality assessment.
- Changes in the microstructure cause the confinement of fluid channels, conseuquently leading to an increasing fluid resistance.

The findings of this chapter are restricted to histology images presented in Table 6-1. Increasing the number of samples would be beneficial in order to increase the database for the purpose of quantitative tissue assessment. Due to a limitation in how the histological images were acquired, at this stage, the models can only be in 2D. As a result, information regarding the third dimension and 3D nature of the tissue microstructure is missing. Furthermore, this study focused on a single acinar structure, and its 'interaction' with the surrounding acini was modelled using the fluid inlet/outlet (which represents the ambient interstitial pressure). Furthermore, it was assumed that the solid phase of tissue is isotropic and elastic, and the viscoelasticity of tissue components was not taken into account (this is not necessarily a limitation as the aim of this chapter is indeed to quantify the source of viscoelasticity due to the fluid movement within tissue microstructure). It is hoped that as a part of the future work experimental validation of this framework will be conducted, ideally in an in vivo environment where the viscoelastic response is measured and the fluid movement can be monitored by real-time imaging technique. Ultimately, it is expected that such an approach will provide an in-depth understanding of the origin of viscoelasticity in prostate (or in soft tissue in general), and lead to a computational tool that can give more useful information about the quality/condition of tissue in an inexpensive way and allow a reduction in the number of expensive and invasive biopsies and clinical scans.

CHAPTER 7

Thesis conclusions and a glimpse into the future

Contents

7.1 Conclusions

Biomechanical engineering is one of the multidisciplinary fields that has seen a rapid growth in the last few decades. This field involves innovation in the application of mechanical engineering principles to improve the quality of human life by resolving key healthcare challenges in a variety of areas. One such area relevant to this thesis is clinical diagnosis and medical devices. This thesis aimed to contribute specifically to soft tissue characterization by tackling the multiscale, multiphysical and multiphasic problem of mechanics of soft tissue. The work was expected to point the potential advances in diagnostic techniques resulting in an impact on increasing the life expectancy of the patients. In particular, the main objective was to investigate how microstructural changes in soft tissue subject to various pathophysiological conditions influences its mechanical properties, e.g. viscoelasticity, by taking into account its biphasic nature (i.e. consisting of solid and fluid phases).

The main conclusions of this thesis is provided in the following section.

Chapter 3: Image processing and microstructural characterization of prostatic histology

- A framework has been proposed for morphological indices for the microstructural analysis of prostate tissue histology based on image processing.

The advantage of this is that the proposed indices are able to categorise different pathologies in prostate tissue based on variations in their microstructural morphologies. This methodology could be applied to other tissue types, especially those consisting of the glandular structures, e.g. breast tissue. The results of this chapter were further used in Chapter 4, to help correlate the tissue microstructural indices to its apparent mechanical properties.

Chapter 4: Multiscale mechano-morphological homogenization of prostate tissue

- Proposed a framework for microstructure-based numerical homogenization of soft tissue.
- Correlated microstructural indices to the apparent mechanical properties of the tissue.

In this chapter two main contributions were made; firstly, a framework for multiscale homogenization of soft tissue in various pathological conditions was established; secondly, the apparent mechanical properties of tissue samples were correlated to their microstructural indices, which were previously discussed in Chapter 3. This provides quantitative diagnosis on tissue conditions (i.e. either cancerous, BPH or healthy) to be made from both mechanical tests and the image processing results performed on the samples. More importantly, this also provides a deeper understanding of the degree of anisotropy of prostate tissue samples, which can also contribute to diagnostic methods (e.g. those based on mechanical properties) by providing a fresh perspective of the heterogeneity and material anisotropy of the examined tissue.

Chapter 5: Parametric study of simplified tissue structure – considering the biphasic nature of prostate tissue

- A numerical framework integrating fluid-structure interaction modelling with the numerical homogenization scheme was used, to explore the influence of the microstructural variations in various prostate tissue samples in the movement of interstitial fluid therein;
- hypothesised that the viscoelasticity in prostate tissue could be contributed, in part, from the fluid movement in tissue microstructure and its physical interaction with the tissue solid phase;
- Verified the proposed hypothesis in both analytical simplified models and realistic microstructure reconstructed from tissue histology.

In this chapter, compared to the previous efforts made in literature for homogenization analysis in biological tissues[166], the framework established here takes into account the interaction between fluid phase (e.g. acinar fluid in prostate) and structural phase (e.g. stromal tissue in prostate) in prostate tissue. The microstructure of prostate tissue was simplified in order to carry out a parametric study and verify the proposed framework. Furthermore, two realistic tissue microstructures reconstructed from cancerous and non-cancerous part of prostate histology were used to further demonstrate the feasibility of the proposed framework. This chapter highlighted the importance of fluid movement and its effect in the apparent mechanical properties of tissue. This framework could provide a novel insight into the source of viscoelasticity in prostate, and potentially in other glandular tissues, in addition to the well-known source of viscoelasticity as a result of intrinsic properties of tissue components such as elastin and collagen fibres.

Chapter 6: Viscoelasticity in prostate tissue due to fluid-structure interaction – a further study

- Carried out fluid-structure interaction modelling of prostate tissue for cancerous and non-cancerous pathologies;
- Investigated the effect of changes in tissue microstructure in their mechanical properties based on realistic histological samples of prostate;
- Explored the fluid resistance with respect to microstructural changes and its correlation to the apparent tissue viscoelastic properties.

This chapter employed the methodology proposed in the previous chapter and provided a more comprehensive understanding of the tissue viscoelasticity arising from the fluid movement in tissue microstructure. This framework compared the viscoelasticity in cancerous and non-cancerous tissue samples. Changes in the tissue microstructure were shown to affect the apparent viscoelastic time constant and fluid resistance of the tissue. As a result, cancerous samples have higher time constant and instantaneous moduli than non-cancerous ones. Using the apparent time constant as an additional index could provide more information of tissue quality and if a larger database of tissue samples can be obtained, it is envisaged to help improve the precision of non-invasive clinical diagnosis including those based on palpation measurement techniques.

7.2 Limitations and a glimpse into the future

The main aim of this thesis was to gain a deeper quantitative understanding of the elasticity and viscoelasticity in prostate tissue, and more importantly, their variations with respect to different pathologies. Although the methodologies proposed in this thesis have been verified, in some cases, in realistic scenarios such as those using histological images, certain challenges are still to be addressed in the future to further implement this work to clinical practice.

A number of limitations of this study will be discussed below, alongside ideas that could mitigate or resolve those by possible future work. :

A larger database of histological samples: In all the chapters data from patients have been used to check the feasibility of the proposed methodologies. However, the datasets used in Chapters 3 and 4 are limited to one histological image (one prostate sample). It is expected that an increase in the number of histological samples would improve the accuracy of the models in a more statistical way. It would also enable the investigation of the intra- and inter-patient variabilities, which are of critical importance prior to potential clinical application. Such results could also be used to develop tissue classification based on a range of indices (either mechanical or morphological) as an assistant to the clinical diagnostic indices that are currently being used by pathologists.

Applying the approach to other tissues and pathologies: The main focus of this thesis was on prostate tissue. However, it should be noted that prostate tissue was used as an exemplar tissue system in this thesis. The proposed methodologies have the potential to be introduced and tested on other tissue types, especially those with glandular structures, which could significantly extend the impact of this thesis work.

3D implementation: Since all the tissue morphologies used in this thesis were reconstructed from histological images, the microstructures are all in 2D. As a result, the behaviour along the third dimension, and particularly the fluid movement when FSI is used, is neglected. It is expected that, in the future, the acquisition of such 3D models of prostate tissue with detailed microstructural descriptions will be made available. This would provide a better picture of channel interconnectivity in order to fully understand the role of fluid movement in 3D tissue microstructures.

Experimental validation and diagnostic devices: Experimental validation of the proposed framework in Chapter 5 would be an ideal addition to the noble advantage to support the current computational results. This experimental validation could be in the form of ex vivo mechanical measurements (e.g. indentation or uni/bi-axial tensile tests) or even in vivo measurements during surgery. Design of systematic experiments to validate the proposed methodology would make a significant impact on the applicability of the proposed methodology for clinical use. Implementation of such a methodology in a potential medical device (e.g. static or dynamic palpation) for the diagnostic purpose might be of interest. Such a device would provide a measurement of tissue mechanical properties (e.g. viscoelasticity), thus providing useful information about the nature of tissue quality (e.g. classification of pathologies, grade and invasiveness of cancer) by performing in vivo tests during the cancer screening process or surgery.

Bibliography

[1] S. W. Lindley, E. M. Gillies, and L. A. Hassell, “Communicating diagnostic uncertainty in surgical pathology reports: Disparities between sender and receiver,” *Pathol. - Res. Pract.*, vol. 210, no. 10, pp. 628–633, 2014.

[2] E. Mazza, A. Nava, D. Hahnloser, W. Jochum, and M. Bajka, “The mechanical response of human liver and its relation to histology: An in vivo study,” *Med. Image Anal.*, vol. 11, no. 6, pp. 663–672, Dec. 2007.

[3] B. Weigelt, F. C. Geyer, and J. S. Reis-Filho, “Histological types of breast cancer: how special are they?,” *Mol. Oncol.*, vol. 4, no. 3, pp. 192–208, 2010.

[4] “4.1 Types of Tissues | Anatomy and Physiology.” [Online]. Available: https://opentextbc.ca/anatomyandphysiology/chapter/4-1-types-of-tissues/. [Accessed: 22-May-2017].

[5] G. Lippolis, A. Edsjö, L. Helczynski, A. Bjartell, and N. C. Overgaard, “Automatic registration of multi-modal microscopy images for integrative analysis of prostate tissue sections.,” *BMC Cancer*, vol. 13, no. 1, p. 408, 2013.

[6] P. Michael H. Ross Michael H. Ross, P. and C. E. D. of A. and C. Biology, (deceased), F. University of Florida College of Medicine Gainesville, and W. Pawlina, *Histology: A Text and Atlas*, 6th ed. .

[7] M. Malatesta, “Histological and Histochemical Methods - Theory and practice,” *Eur. J. Histochem.*, vol. 60, no. 1, Feb. 2016.

[8] J. M. Potts, “The four categories of prostatitis: a practical approach to treatment.,” *Cleve. Clin. J. Med.*, vol. 68, no. 5, pp. 389–90, 392–3, 397, May 2001.

[9] M. J. Barry, "Epidemiology and natural history of benign prostatic hyperplasia.," *Urol. Clin. North Am.*, vol. 17, no. 3, pp. 495–507, Aug. 1990.

[10] Y. Homma, K. Kawabe, T. Tsukamoto, O. Yamaguchi, K. Okada, Y. Aso, H. Watanabe, E. Okajima, J. Kumazawa, T. Yamaguchi, and Y. Ohashi, "Estimate criteria for diagnosis and severity in benign prostatic hyperplasia.," *Int. J. Urol.*, vol. 3, no. 4, pp. 261–6, Jul. 1996.

[11] G. B. Auffenberg, B. T. Helfand, and K. T. McVary, "Established Medical Therapy for Benign Prostatic Hyperplasia," *Urol. Clin. North Am.*, vol. 36, no. 4, pp. 443–459, 2009.

[12] S. Phipps, T. H. J. Yang, F. K. Habib, R. L. Reuben, and S. a McNeill, "Measurement of the mechanical characteristics of benign prostatic tissue: a novel method for assessing benign prostatic disease.," *Urology*, vol. 65, no. 5, pp. 1024–8, May 2005.

[13] "Cancer Research UK," 2017. [Online]. Available: http://www.cancerresearchuk.org/health-professional/cancer-statistics/statistics-by-cancer-type/prostate-cancer. [Accessed: 09-Aug-2017].

[14] R. Montironi, F. R. Path, and R. Mazzucchelli, "Gleason grading of prostate cancer. Contemporary approach.," *Pathologica.*, vol. 97, no. 4, p. 164, 2005.

[15] D. F. Gleason, "Histologic Grading of Prostate Cancer : A Perspective," 1992.

[16] P. a Humphrey, "Gleason grading and prognostic factors in carcinoma of the prostate," *Mod. Pathol.*, vol. 17, no. 3, pp. 292–306, 2004.

[17] L. He, L. R. Long, S. Antani, and G. R. Thoma, "Histology image analysis for carcinoma detection and grading," *Comput. Methods Programs Biomed.*, vol. 107, no. 3, pp. 538–556, 2012.

[18] S. Doyle, M. Hwang, K. Shah, A. Madabhushi, M. Feldman, and J. Tomaszeweski,

“Automated Grading Of Prostate Cancer Using Architectural And Textural Image Features,” in *2007 4th IEEE International Symposium on Biomedical Imaging: From Nano to Macro*, 2007, pp. 1284–1287.

[19] S. Doyle, A. Madabhushi, M. Feldman, and J. Tomaszeweski, “A Boosting Cascade for Automated Detection of Prostate Cancer from Digitized Histology,” Springer, Berlin, Heidelberg, 2006, pp. 504–511.

[20] S. Doyle, S. Agner, A. Madabhushi, M. Feldman, and J. Tomaszewski, “Automated grading of breast cancer histopathology using spectral clusteringwith textural and architectural image features,” in *2008 5th IEEE International Symposium on Biomedical Imaging: From Nano to Macro*, 2008, pp. 496–499.

[21] S. Naik, S. Doyle, S. Agner, A. Madabhushi, M. Feldman, and J. Tomaszewski, “Automated gland and nuclei segmentation for grading of prostate and breast cancer histopathology,” in *2008 5th IEEE International Symposium on Biomedical Imaging: From Nano to Macro*, 2008, pp. 284–287.

[22] M. Ladekarl, T. Bœk-Hansen, R. Henrik-Nielsen, C. Mouritzen, U. Henriques, and F. B. Sørensen, “Objective malignancy grading of squamous cell carcinoma of the lung. Stereologic estimates of mean nuclear size are of prognostic value, independent of clinical stage of disease,” *Cancer*, vol. 76, no. 5, pp. 797–802, Sep. 1995.

[23] J. Diamond, N. H. Anderson, P. H. Bartels, R. Montironi, and P. W. Hamilton, “The Use of Morphological Characteristics and Texture Analysis in the Identification of Tissue Composition in Prostatic Neoplasia.”

[24] J. Gil, H. Wu, and B. Y. Wang, “Image analysis and morphometry in the diagnosis of breast cancer,” *Microsc. Res. Tech.*, vol. 59, no. 2, pp. 109–118, Oct. 2002.

[25] M. Guillaud, D. Cox, A. Malpica, G. Staerkel, J. Matisic, D. Van Niekirk, K.

Adler-Storthz, N. Poulin, M. Follen, and C. MacAulay, “Quantitative histopathological analysis of cervical intra-epithelial neoplasia sections: methodological issues.,” *Cell. Oncol.*, vol. 26, no. 1–2, pp. 31–43, 2004.

[26] R. Dobrescu, “Diagnosis of Breast Cancer from Mammograms by Using Fractal Measures,” *Int. J. Med. Imaging*, vol. 1, no. 2, p. 32, 2013.

[27] M. Ivanovici, N. Richard, and H. Decean, “Fractal Dimension and Lacunarity of Psoriatic Lesions—A Colour Approach—,” *Proc. 2nd WSEAS Int. Conf. Biomed. Electron. Biomed. INFORMATICS*, pp. 199–202, 2009.

[28] D. Chappard, E. Legrand, B. Haettich, G. Chals, B. Auvinet, J. P. Eschard, J. P. Hamelin, M. F. Basl, and M. Audran, “Fractal dimension of trabecular bone: Comparison of three histomorphometric computed techniques for measuring the architectural two-dimensional complexity,” *J. Pathol.*, vol. 195, no. 4, pp. 515–521, 2001.

[29] D. Sanchez-Molina, J. Velazquez-Ameijide, V. Quintana, C. Arregui-Dalmases, J. R. Crandall, D. Subit, and J. R. Kerrigan, “Fractal dimension and mechanical properties of human cortical bone,” *Med. Eng. Phys.*, vol. 35, no. 5, pp. 576–582, 2013.

[30] P. Waliszewski, “The Quantitative Criteria Based on the Fractal Dimensions, Entropy, and Lacunarity for the Spatial Distribution of Cancer Cell Nuclei Enable Identification of Low or High Aggressive Prostate Carcinomas,” *Front. Physiol.*, vol. 7, p. 34, Feb. 2016.

[31] Po-Whei Huang and Cheng-Hsiung Lee, “Automatic Classification for Pathological Prostate Images Based on Fractal Analysis,” *IEEE Trans. Med. Imaging*, vol. 28, no. 7, pp. 1037–1050, Jul. 2009.

[32] P. Scanlan, S. J. Hammer, D. Good, W. Shu, R. L. Reuben, S. Phipps, G. D.

Stewart, and S. A. McNeill, “A Scalable Actuator for the Dynamic Palpation of Soft Tissue for Use in the Assessment of Prostate Tissue Quality,” *Procedia Eng.*, vol. 87, pp. 656–659, 2014.

[33] J. S. Quon, B. Moosavi, M. Khanna, T. A. Flood, C. S. Lim, and N. Schieda, “False positive and false negative diagnoses of prostate cancer at multi-parametric prostate MRI in active surveillance.,” *Insights Imaging*, vol. 6, no. 4, pp. 449–63, Aug. 2015.

[34] C. Rasch, I. Barillot, P. Remeijer, A. Touw, M. van Herk, and J. V Lebesque, “Definition of the prostate in CT and MRI: a multi-observer study,” *Int. J. Radiat. Oncol.*, vol. 43, no. 1, pp. 57–66, 1999.

[35] Y. K. Mariappan, K. J. Glaser, and Richard L Ehman, “Magnetic Resonance Elastography: a Review,” *Clin. Anat. (New York, NY)*, vol. 23, no. 5, pp. 497–511, 2010.

[36] A. Heidenreich, P. J. Bastian, J. Bellmunt, M. Bolla, S. Joniau, T. van der Kwast, M. Mason, V. Matveev, T. Wiegel, F. Zattoni, and N. Mottet, “EAU Guidelines on Prostate Cancer. Part II: Treatment of Advanced, Relapsing, and Castration-Resistant Prostate Cancer,” 2014.

[37] G. Dougherty and G. M. Henebry, “Lacunarity analysis of spatial pattern in CT images of vertebral trabecular bone for assessing osteoporosis,” *Med. Eng. Phys.*, vol. 24, no. 2, pp. 129–138, 2002.

[38] F. Nensa, K. Beiderwellen, P. Heusch, and A. Wetter, “Clinical applications of PET/MRI: current status and future perspectives.,” *Diagn. Interv. Radiol.*, vol. 20, no. 5, pp. 438–47, 2014.

[39] “Urology Care Foundation - How is Prostate Cancer Diagnosed?” [Online]. Available: http://www.urologyhealth.org/urologic-conditions/prostate-

cancer/diagnosis. [Accessed: 31-May-2017].

[40] E. Kimoto, T. Shoji, K. Shinohara, S. Hatsuda, K. Mori, S. Fukumoto, H. Koyama, M. Emoto, Y. Okuno, and Y. Nishizawa, "Regional arterial stiffness in patients with type 2 diabetes and chronic kidney disease.," *J. Am. Soc. Nephrol.*, vol. 17, no. 8, pp. 2245–52, Aug. 2006.

[41] P. Boutouyrie, A. I. Tropeano, R. Asmar, I. Gautier, A. Benetos, P. Lacolley, and S. Laurent, "Aortic stiffness is an independent predictor of primary coronary events in hypertensive patients: a longitudinal study.," *Hypertens. (Dallas, Tex. 1979)*, vol. 39, no. 1, pp. 10–5, Jan. 2002.

[42] R. Akhtar, M. J. Sherratt, J. K. Cruickshank, and B. Derby, "Characterizing the elastic properties of tissues.," *Mater. Today (Kidlington).*, vol. 14, no. 3, pp. 96–105, Mar. 2011.

[43] A. M. Handorf, Y. Zhou, M. A. Halanski, and W.-J. Li, "Tissue stiffness dictates development, homeostasis, and disease progression.," *Organogenesis*, vol. 11, no. 1, pp. 1–15, 2015.

[44] S. Mueller and L. Sandrin, "Liver stiffness: a novel parameter for the diagnosis of liver disease.," *Hepat. Med.*, vol. 2, pp. 49–67, May 2010.

[45] K. Hoyt, B. Castaneda, M. Zhang, P. Nigwekar, P. A. di Sant'agnese, J. V Joseph, J. Strang, D. J. Rubens, and K. J. Parker, "Tissue elasticity properties as biomarkers for prostate cancer.," *Cancer Biomark.*, vol. 4, no. 4–5, pp. 213–25, 2008.

[46] L. Zhang, S. P. Lake, V. K. Lai, C. R. Picu, V. H. Barocas, and M. S. Shephard, "A coupled fiber-matrix model demonstrates highly inhomogeneous microstructural interactions in soft tissues under tensile load.," *J. Biomech. Eng.*, vol. 135, no. 1, p. 11008, Jan. 2013.

[47] Z. Teng, J. Yuan, J. Feng, Y. Zhang, A. J. Brown, S. Wang, Q. Lu, and J. H. Gillard,

"The influence of constitutive law choice used to characterise atherosclerotic tissue material properties on computing stress values in human carotid plaques," *J. Biomech.*, vol. 48, no. 14, pp. 3912–3921, 2015.

[48] J. G. Snedeker, P. Niederer, F. R. Schmidlin, M. Farshad, C. K. Demetropoulos, J. B. Lee, and K. H. Yang, "Strain-rate dependent material properties of the porcine and human kidney capsule," *J. Biomech.*, vol. 38, no. 5, pp. 1011–1021, 2005.

[49] a. Nordez, J. L. Gennisson, P. Casari, S. Catheline, and C. Cornu, "Characterization of muscle belly elastic properties during passive stretching using transient elastography," *J. Biomech.*, vol. 41, pp. 2305–2311, 2008.

[50] T. Ushiki, "Collagen fibers, reticular fibers and elastic fibers. A comprehensive understanding from a morphological viewpoint.," *Archives of histology and cytology*, vol. 65, no. 2. pp. 109–26, Jun-2002.

[51] P. Sáez, E. Peña, M. Doblaré, and M. a. Martínez, "Hierarchical micro-adaptation of biological structures by mechanical stimuli," *Int. J. Solids Struct.*, vol. 50, no. 14–15, pp. 2353–2370, Jul. 2013.

[52] M. Auer and T. C. Gasser, "Reconstruction and Finite Element Mesh Generation of Abdominal Aortic Aneurysms From Computerized Tomography Angiography Data With Minimal User Interactions," *IEEE Trans. Med. Imaging*, vol. 29, no. 4, pp. 1022–1028, Apr. 2010.

[53] T. C. Gasser, M. Auer, F. Labruto, J. Swedenborg, and J. Roy, "Biomechanical Rupture Risk Assessment of Abdominal Aortic Aneurysms: Model Complexity versus Predictability of Finite Element Simulations," *Eur. J. Vasc. Endovasc. Surg.*, vol. 40, no. 2, pp. 176–185, Aug. 2010.

[54] J. Li, X. Y. Luo, and Z. B. Kuang, "A nonlinear anisotropic model for porcine aortic heart valves," *J. Biomech.*, vol. 34, no. 10, pp. 1279–1289, 2001.

[55] P. S. Wellman, R. D. Howe, E. Dalton, and K. A. Kern, “Breast Tissue Stiffness in Compression is Correlated to Histological Diagnosis,” pp. 1–15.

[56] B.-M. Ahn, J. Kim, L. Ian, K.-H. Rha, and H.-J. Kim, “Mechanical property characterization of prostate cancer using a minimally motorized indenter in an ex vivo indentation experiment.,” *Urology*, vol. 76, no. 4, pp. 1007–11, Oct. 2010.

[57] X. Wang, J. Wang, Y. Liu, H. Zong, X. Che, W. Zheng, F. Chen, Z. Zhu, D. Yang, and X. Song, “Alterations in mechanical properties are associated with prostate cancer progression,” *Med. Oncol.*, vol. 31, no. 3, p. 876, Mar. 2014.

[58] T. Shearer, “A new strain energy function for the hyperelastic modelling of ligaments and tendons based on fascicle microstructure,” *J. Biomech.*, vol. 48, no. 2, pp. 290–297, 2015.

[59] G. A. Holzapfel, “Biomechanics of Soft Tissue,” *Handb. Mater. Behav. Model.*, no. 3, pp. 1049–1063, 2001.

[60] G. A. Holzapfel and T. C. Gasser, “A viscoelastic model for fiber-reinforced composites at finite stains: Continuum basis, computational aspects and applications,” *Comput. Methods Appl. Mech. Eng.*, vol. 190, no. 34, pp. 4379–4403, 2001.

[61] A. Natali, P. Pavan, E. Carniel, P. Dario, and I. Izzo, “Characterization of soft tissue mechanics with aging,” *IEEE Eng. Med. Biol. Mag.*, vol. 27, no. 4, pp. 15–22, Jul. 2008.

[62] C. Y. Huang, V. C. Mow, and G. A. Ateshian, “The role of flow-independent viscoelasticity in the biphasic tensile and compressive responses of articular cartilage.,” *J. Biomech. Eng.*, vol. 123, no. 5, pp. 410–417, 2001.

[63] A. E. Kerdok, M. P. Ottensmeyer, and R. D. Howe, “Effects of perfusion on the viscoelastic characteristics of liver.,” *J. Biomech.*, vol. 39, no. 12, pp. 2221–31,

Jan. 2006.

[64] V. C. Mow, S. C. Kuei, W. M. Lai, and C. G. Armstrong, “Biphasic creep and stress relaxation of articular cartilage in compression? Theory and experiments.,” *J. Biomech. Eng.*, vol. 102, no. 1, pp. 73–84, 1980.

[65] H. W. Haslach, L. N. Leahy, P. Riley, R. Gullapalli, S. Xu, and A. H. Hsieh, “Solid–extracellular fluid interaction and damage in the mechanical response of rat brain tissue under confined compression,” *J. Mech. Behav. Biomed. Mater.*, vol. 29, pp. 138–150, 2014.

[66] H. W. Haslach, L. N. Leahy, and A. H. Hsieh, “Transient solid–fluid interactions in rat brain tissue under combined translational shear and fixed compression,” *J. Mech. Behav. Biomed. Mater.*, vol. 48, pp. 12–27, 2015.

[67] K. J. Parker, “A microchannel flow model for soft tissue elasticity,” *Phys. Med. Biol.*, vol. 59, no. 15, pp. 4443–57, 2014.

[68] K. J. Parker, “Experimental evaluations of the microchannel flow model,” *Phys. Med. Biol.*, vol. 60, no. 11, pp. 4227–4242, 2015.

[69] S. W. Park and R. A. Schapery, “Methods of interconversion between linear viscoelastic material functions. Part I—a numerical method based on Prony series,” *Int. J. Solids Struct.*, vol. 36, no. 11, pp. 1653–1675, 1999.

[70] J. Palacio-Torralba, S. Hammer, D. W. Good, S. Alan McNeill, G. D. Stewart, R. L. Reuben, and Y. Chen, “Quantitative diagnostics of soft tissue through viscoelastic characterization using time-based instrumented palpation.,” *J. Mech. Behav. Biomed. Mater.*, vol. 41C, pp. 149–160, Oct. 2014.

[71] A. Anssari-Benam, D. L. Bader, and H. R. C. Screen, “Anisotropic time-dependant behaviour of the aortic valve,” *J. Mech. Behav. Biomed. Mater.*, vol. 4, no. 8, pp. 1603–1610, 2011.

[72] H. Zhang, Y. Wang, and M. F. Insana, “Ramp-hold relaxation solutions for the KVFD model applied to soft viscoelastic media,” *Meas. Sci. Technol.*, vol. 27, no. 2, p. 25702, 2016.

[73] M. Zhang, B. Castaneda, Z. Wu, P. Nigwekar, J. V. Joseph, D. J. Rubens, and K. J. Parker, “Congruence of Imaging Estimators and Mechanical Measurements of Viscoelastic Properties of Soft Tissues,” *Ultrasound Med. Biol.*, vol. 33, no. 10, pp. 1617–1631, 2007.

[74] L. S. Taylor, A. L. Lerner, D. J. Rubens, and K. J. Parker, “A Kelvin-Voight Fractional Derivative Model for Viscoelastic Characterization of Liver Tissue,” in *Advances in Bioengineering*, 2002, vol. 2002, pp. 447–448.

[75] M. Umut Ozcan, S. Ocal, C. Basdogan, G. Dogusoy, and Y. Tokat, “Characterization of frequency-dependent material properties of human liver and its pathologies using an impact hammer.,” *Med. Image Anal.*, vol. 15, no. 1, pp. 45–52, Feb. 2011.

[76] M. Z. Kiss, T. Varghese, and T. J. Hall, “Viscoelastic characterization of *in vitro* canine tissue,” *Phys. Med. Biol.*, vol. 49, no. 18, pp. 4207–4218, Sep. 2004.

[77] J. H. T. Bates, “A Recruitment Model of Quasi-Linear Power-Law Stress Adaptation in Lung Tissue,” *Ann. Biomed. Eng.*, vol. 35, no. 7, pp. 1165–1174, Jun. 2007.

[78] J. MEAD, “Mechanical properties of lungs.,” *Physiol. Rev.*, vol. 41, pp. 281–330, Apr. 1961.

[79] P. Yu and Y. M. Haddad, “On the dynamic system identification of the response behaviour of linear viscoelastic materials,” *Int. J. Press. Vessel. Pip.*, vol. 67, no. 1, pp. 45–54, Jun. 1996.

[80] A. B. Tran, J. Yvonnet, Q.-C. He, C. Toulemonde, and J. Sanahuja, “A simple

computational homogenization method for structures made of linear heterogeneous viscoelastic materials,” *Comput. Methods Appl. Mech. Eng.*, vol. 200, no. 45, pp. 2956–2970, 2011.

[81] S. Bergstr, “Calculation of Prony Series Parameters From Dynamic Frequency Data Definition of a Prony Series Conversion from Dynamic Frequency Data to Prony Series Data,” pp. 4–5, 2005.

[82] A. Krairi and I. Doghri, “A thermodynamically-based constitutive model for thermoplastic polymers coupling viscoelasticity, viscoplasticity and ductile damage,” *Int. J. Plast.*, vol. 60, pp. 163–181, 2014.

[83] S. A. Norris, “Stability analysis of a viscoelastic model for ion-irradiated silicon,” Jan. 2012.

[84] M. Unnikrishnan, A. C. Menon, and J. Joseph, “Analysis of Blood Flow through Viscoelastic Blood Vessel,” *Int. J. Appl. Res. Mech. Eng.*, no. 1, pp. 2231–5950, 2011.

[85] P. P. Provenzano, R. S. Lakes, D. T. Corr, and R. Vanderby, “Application of nonlinear viscoelastic models to describe ligament behavior,” *Biomech. Model. Mechanobiol.*, vol. 1, no. 1, pp. 45–57, Jun. 2002.

[86] B. S. Elkin, A. I. Ilankovan, and B. Morrison, “A Detailed Viscoelastic Characterization of the P17 and Adult Rat Brain,” *J. Neurotrauma*, vol. 28, no. 11, pp. 2235–2244, Nov. 2011.

[87] S. W. Park and Y. R. Kim, “Fitting Prony-Series Viscoelastic Models With Power-Law Presmoothing,” 2001.

[88] G. A. Holzapfel and T. C. Gasser, “A viscoelastic model for fiber-reinforced composites at finite strains: Continuum basis, computational aspects and applications,” *Comput. Methods Appl. Mech. Eng.*, vol. 190, no. 34, pp. 4379–

4403, 2001.

[89] G. A. Holzapfel, T. C. Gasser, and R. W. Ogden, “A New Constitutive Framework for Arterial Wall Mechanics and a Comparative Study of Material Models,” *J. Elast.*, vol. 61, no. 1/3, pp. 1–48, 2000.

[90] “Gerhard A. Holzapfel Nonlinear Solid Mechanics- A Continuum Approach for Engineering 2000.pdf.” .

[91] E. Peña, V. Alastrué, A. Laborda, M. A. Martínez, and M. Doblaré, “A constitutive formulation of vascular tissue mechanics including viscoelasticity and softening behaviour,” *J. Biomech.*, vol. 43, no. 5, pp. 984–989, 2010.

[92] T. C. Gasser and C. Forsell, “The numerical implementation of invariant-based viscoelastic formulations at finite strains. An anisotropic model for the passive myocardium,” *Comput. Methods Appl. Mech. Eng.*, vol. 200, no. 49–52, pp. 3637–3645, 2011.

[93] J. S. Bergström and M. C. Boyce, “Constitutive modeling of the time-dependent and cyclic loading of elastomers and application to soft biological tissues,” *Mech. Mater.*, vol. 33, no. 9, pp. 523–530, 2001.

[94] J. Bergstrom, “Constitutive modeling of the large strain time-dependent behavior of elastomers,” *J. Mech. Phys. Solids*, vol. 46, no. 5, pp. 931–954, 1998.

[95] H. R. C. Screen, “Investigating load relaxation mechanics in tendon,” *J. Mech. Behav. Biomed. Mater.*, vol. 1, no. 1, pp. 51–58, 2008.

[96] B. R. Simon, “Multiphase poroelastic finite element models for soft tissue structure,” *Appl. Mech. Rev.*, vol. 45, no. 6, 1992.

[97] D. L. Brown, P. Popov, and Y. Efendiev, “Effective equations for fluid-structure interaction with applications to poroelasticity,” *Appl. Anal.*, vol. 93, no. 4, pp. 771–790, Nov. 2013.

[98] L. Yin and D. M. Elliott, “A biphasic and transversely isotropic mechanical model for tendon: Application to mouse tail fascicles in uniaxial tension,” *J. Biomech.*, vol. 37, no. 6, pp. 907–916, 2004.

[99] S. Raghunathan, D. Evans, and J. L. Sparks, “Poroviscoelastic Modeling of Liver Biomechanical Response in Unconfined Compression,” *Ann. Biomed. Eng.*, vol. 38, no. 5, pp. 1789–1800, 2010.

[100] G. U. Unnikrishnan, “Constitutive Material Modeling of Cell: A Micromechanics Approach,” *J. Biomech. Eng.*, vol. 129, no. 3, p. 315, 2006.

[101] J. Palacio, a Jorge-Peñas, a Muñoz-Barrutia, C. Ortiz-de-Solorzano, E. de Juan-Pardo, and J. M. García-Aznar, “Numerical estimation of 3D mechanical forces exerted by cells on non-linear materials.,” *J. Biomech.*, vol. 46, no. 1, pp. 50–5, Jan. 2013.

[102] R. Leiderman, P. E. Barbone, a a Oberai, and J. C. Bamber, “Coupling between elastic strain and interstitial fluid flow: ramifications for poroelastic imaging,” *Phys Med Biol*, vol. 51, no. 24, pp. 6291–6313, 2006.

[103] W. C. Carson, G. J. Gerling, T. L. Krupski, C. G. Kowalik, J. C. Harper, and C. a Moskaluk, “Material characterization of ex vivo prostate tissue via spherical indentation in the clinic.,” *Med. Eng. Phys.*, vol. 33, no. 3, pp. 302–9, Apr. 2011.

[104] P. Garteiser, S. Doblas, J.-L. Daire, M. Wagner, H. Leitao, V. Vilgrain, R. Sinkus, and B. E. Van Beers, “MR elastography of liver tumours: value of viscoelastic properties for tumour characterisation.,” *Eur. Radiol.*, vol. 22, no. 10, pp. 2169–77, Oct. 2012.

[105] R. Sinkus, M. Tanter, T. Xydeas, S. Catheline, J. Bercoff, and M. Fink, “Viscoelastic shear properties of in vivo breast lesions measured by MR elastography.,” *Magn. Reson. Imaging*, vol. 23, no. 2, pp. 159–65, Feb. 2005.

[106] T. a Krouskop, T. M. Wheeler, F. Kallel, B. S. Garra, and T. Hall, “Elastic moduli of breast and prostate tissues under compression.,” *Ultrason. Imaging*, vol. 20, no. 4, pp. 260–274, 1998.

[107] M. KJÆR, “Role of Extracellular Matrix in Adaptation of Tendon and Skeletal Muscle to Mechanical Loading,” *Physiol. Rev.*, vol. 84, no. 2, 2004.

[108] L. Cheng, R. Mazzucchelli, T. D. Jones, A. Lopez-Beltran, and R. Montironi, “Chapter 3 – The Pathology of Prostate Cancer,” in *Early Diagnosis and Treatment of Cancer Series: Prostate Cancer*, 2010, pp. 45–83.

[109] M. Zhou and J. R. Srigley, “Benign mimickers and potential precursors of prostatic adenocarcinoma,” *Diagnostic Histopathol.*, vol. 17, no. 10, pp. 434–446, 2011.

[110] J. Palacio-Torralba, E. Jiménez Aguilar, D. W. Good, S. Hammer, S. A. McNeill, G. D. Stewart, R. L. Reuben, and Y. Chen, “Patient specific modeling of palpation-based prostate cancer diagnosis: effects of pelvic cavity anatomy and intrabladder pressure,” *Int. j. numer. method. biomed. eng.*, vol. 32, no. 1, p. e02734, Jan. 2016.

[111] J. Ophir, I. C??spedes, H. Ponnekanti, Y. Yazdi, and X. Li, “Elastography: A quantitative method for imaging the elasticity of biological tissues,” *Ultrason. Imaging*, vol. 13, no. 2, pp. 111–134, 1991.

[112] A. Itoh, E. Ueno, E. Tohno, H. Kamma, H. Takahashi, T. Shiina, M. Yamakawa, and T. Matsumura, “Breast Disease: Clinical Application of US Elastography for Diagnosis,” *Radiology*, vol. 239, no. 2, pp. 341–350, 2006.

[113] G. a. Ateshian, N. O. Chahine, I. M. Basalo, and C. T. Hung, “The correspondence between equilibrium biphasic and triphasic material properties in mixture models of articular cartilage,” *J. Biomech.*, vol. 37, no. 3, pp. 391–400, Mar. 2004.

[114] H. W. Haslach, L. N. Leahy, P. Riley, R. Gullapalli, S. Xu, and A. H. Hsieh, “Solid-extracellular fluid interaction and damage in the mechanical response of rat brain

tissue under confined compression,” *J. Mech. Behav. Biomed. Mater.*, vol. 29, pp. 138–150, 2014.

[115] H. Narayanan, E. M. Arruda, K. Grosh, and K. Garikipati, “The micromechanics of fluid-solid interactions during growth in porous soft biological tissue.,” *Biomech. Model. Mechanobiol.*, vol. 8, no. 3, pp. 167–81, Jun. 2009.

[116] K. Garikipati, E. M. Arruda, K. Grosh, H. Narayanan, and S. Calve, “A continuum treatment of growth in biological tissue: The coupling of mass transport and mechanics,” *J. Mech. Phys. Solids*, vol. 52, no. 7, pp. 1595–1625, 2004.

[117] W. Ehlers and B. Markert, “A Linear Viscoelastic Biphasic Model for Soft Tissues Based on the Theory of Porous Media,” *J. Biomech. Eng.*, vol. 123, no. 5, p. 418, 2001.

[118] M. R. DiSilvestro, Q. Zhu, M. Wong, J. S. Jurvelin, and J.-K. F. Suh, “Biphasic Poroviscoelastic Simulation of the Unconfined Compression of Articular Cartilage: I—Simultaneous Prediction of Reaction Force and Lateral Displacement,” *J. Biomech. Eng.*, vol. 123, no. 2, p. 191, 2001.

[119] K. J. Parker, J. Ormachea, S. A. McAleavey, R. W. Wood, J. J. Carroll-Nellenback, and R. K. Miller, “Shear wave dispersion behaviors of soft, vascularized tissues from the microchannel flow model,” *Phys. Med. Biol.*, vol. 61, no. 13, pp. 4890–4903, 2016.

[120] M. Zhang, P. Nigwekar, B. Castaneda, K. Hoyt, J. V Joseph, A. di Sant’Agnese, E. M. Messing, J. G. Strang, D. J. Rubens, and K. J. Parker, “Quantitative characterization of viscoelastic properties of human prostate correlated with histology.,” *Ultrasound Med. Biol.*, vol. 34, no. 7, pp. 1033–1042, 2008.

[121] Y.-T. Cheng and C.-M. Cheng, “Scaling, dimensional analysis, and indentation measurements,” *Mater. Sci. Eng. R Reports*, vol. 44, no. 4–5, pp. 91–149, Aug.

2004.

[122] S. R. Quake and A. Scherer, “From Micro- to Nanofabrication with Soft Materials,” *Science (80-.).*, vol. 290, no. 5496, 2000.

[123] A. Muntean and V. Chalupeck, “Homogenization Method and Multiscale Modeling.”

[124] A. Needleman, “Void Growth in an Elastic-Plastic Medium,” *J. Appl. Mech.*, vol. 39, no. 4, p. 964, 1972.

[125] D. F. Adams and D. R. Doner, “Transverse Normal Loading of a Unidirectional Composite,” *J. Compos. Mater.*, vol. 1, no. 2, pp. 152–164, Apr. 1967.

[126] A. L. Kalamkarov, I. V. Andrianov, and V. V. Danishevs’kyy, “Asymptotic Homogenization of Composite Materials and Structures,” *Appl. Mech. Rev.*, vol. 62, no. 3, p. 30802, May 2009.

[127] M. Wang and N. Pan, “Predictions of effective physical properties of complex multiphase materials,” *Mater. Sci. Eng. R Reports*, vol. 63, no. 1, pp. 1–30, 2008.

[128] W. Kreher and W. Pompe, *Internal stresses in heterogeneous solids*. Akad.-Verl, 1989.

[129] C. P. Wong and R. S. Bollampally, “Thermal conductivity, elastic modulus, and coefficient of thermal expansion of polymer composites filled with ceramic particles for electronic packaging,” *J. Appl. Polym. Sci.*, vol. 74, no. 14, pp. 3396–3403, Dec. 1999.

[130] R. Landauer, “The Electrical Resistance of Binary Metallic Mixtures,” *J. Appl. Phys.*, vol. 23, no. 7, pp. 779–784, Jul. 1952.

[131] J. Wang, J. K. Carson, M. F. North, and D. J. Cleland, “A new approach to modelling the effective thermal conductivity of heterogeneous materials,” *Int. J. Heat Mass Transf.*, vol. 49, no. 17–18, pp. 3075–3083, Aug. 2006.

[132] Y. Agari and T. Uno, “Estimation on thermal conductivities of filled polymers,” *J. Appl. Polym. Sci.*, vol. 32, no. 7, pp. 5705–5712, Nov. 1986.

[133] Z. Hashin and S. Shtrikman, “A variational approach to the theory of the elastic behaviour of multiphase materials,” *J. Mech. Phys. Solids*, vol. 11, no. 2, pp. 127–140, Mar. 1963.

[134] R. W. Zimmerman, “Hashin-Shtrikman bounds on the poisson ratio of a composite material,” *Mech. Res. Commun.*, vol. 19, no. 6, pp. 563–569, Nov. 1992.

[135] S. P. Friedman, “A saturation degree-dependent composite spheres model for describing the effective dielectric constant of unsaturated porous media,” *Water Resour. Res.*, vol. 34, no. 11, pp. 2949–2961, Nov. 1998.

[136] G. P. Loor, “Dielectric properties of heterogeneous mixtures with a polar constituent,” *Appl. Sci. Res.*, vol. 11, no. 1, pp. 310–320, 1964.

[137] T. J. Kelleners, M. S. Seyfried, J. M. Blonquist, J. Bilskie, and D. G. Chandler, “Improved Interpretation of Water Content Reflectometer Measurements in Soils,” *Soil Sci. Soc. Am. J.*, vol. 69, no. 6, p. 1684, 2005.

[138] E. Li, Z. Zhang, C. C. Chang, G. R. Liu, and Q. Li, “Numerical homogenization for incompressible materials using selective smoothed finite element method,” *Compos. Struct.*, vol. 123, pp. 216–232, 2015.

[139] Y.-M. Yi, S.-H. Park, and S.-K. Youn, “Asymptotic homogenization of viscoelastic composites with periodic microstructures,” *Int. J. Solids Struct.*, vol. 35, no. 17, pp. 2039–2055, Jun. 1998.

[140] D. H. Pahr and P. K. Zysset, “Influence of boundary conditions on computed apparent elastic properties of cancellous bone,” *Biomech. Model. Mechanobiol.*, vol. 7, no. 6, pp. 463–476, Dec. 2008.

[141] S. Sturm, S. Zhou, Y.-W. Mai, and Q. Li, “On stiffness of scaffolds for bone tissue

engineering—a numerical study," *J. Biomech.*, vol. 43, no. 9, pp. 1738–1744, 2010.

[142] M. Hain and P. Wriggers, "Numerical homogenization of hardened cement paste," *Comput. Mech.*, vol. 42, no. 2, pp. 197–212, Aug. 2007.

[143] İ. Temizer, T. Wu, and P. Wriggers, "On the optimality of the window method in computational homogenization," *Int. J. Eng. Sci.*, vol. 64, pp. 66–73, Mar. 2013.

[144] A. Düster, H.-G. Sehlhorst, and E. Rank, "Numerical homogenization of heterogeneous and cellular materials utilizing the finite cell method," *Comput. Mech.*, vol. 50, no. 4, pp. 413–431, Oct. 2012.

[145] K. A. Acton, "Meso-Scale Homogenization Methods For Moving Window Analysis," *Blucher Mech. Eng. Proc.*, vol. 1, no. 1, 2014.

[146] F. Marignetti, V. Delli Colli, and Y. Coia, "Design of Axial Flux PM Synchronous Machines Through 3-D Coupled Electromagnetic Thermal and Fluid-Dynamical Finite-Element Analysis," *IEEE Trans. Ind. Electron.*, vol. 55, no. 10, pp. 3591–3601, Oct. 2008.

[147] S. Koric, L. C. Hibbeler, R. Liu, and B. G. Thomas, "Multiphysics Model of Metal Solidification on the Continuum Level," *Numer. Heat Transf. Part B Fundam.*, vol. 58, no. 6, pp. 371–392, Dec. 2010.

[148] M. Brocchini and O. M. Faltinsen, "Advances in fluid mechanics for offshore engineering: a modelling perspective.," *Philos. Trans. A. Math. Phys. Eng. Sci.*, vol. 373, no. 2033, Jan. 2015.

[149] M. Malvè, a. P. del Palomar, S. Chandra, J. L. López-Villalobos, E. a. Finol, a. Ginel, and M. Doblaré, "FSI Analysis of a Human Trachea Before and After Prosthesis Implantation," *J. Biomech. Eng.*, vol. 133, no. 7, p. 71003, 2011.

[150] D. Bluestein, Y. Alemu, I. Avrahami, M. Gharib, K. Dumont, J. J. Ricotta, and S.

Einav, “Influence of microcalcifications on vulnerable plaque mechanics using FSI modeling.,” *J. Biomech.*, vol. 41, no. 5, pp. 1111–8, Jan. 2008.

[151] C. M. Murea, “NUMERICAL SIMULATION OF A PULSATILE FLOW THROUGH A FLEXIBLE CHANNEL,” *ESAIM Math. Model. Numer. Anal.*, vol. 40, no. 6, pp. 1101–1125, 2006.

[152] A. Quarteroniab and L. Formaggia, *Mathematical Modelling and Numerical Simulation of the Cardiovascular System*, vol. 12. Elsevier, 2004.

[153] H. Gao, X. Ma, N. Qi, C. Berry, B. E. Griffith, and X. Luo, “A finite strain nonlinear human mitral valve model with fluid-structure interaction,” *Int. j. numer. method. biomed. eng.*, vol. 30, no. 12, pp. 1597–1613, Dec. 2014.

[154] K. S. Kunzelman, D. R. Einstein, and R. P. Cochran, “Fluid-structure interaction models of the mitral valve: function in normal and pathological states.,” *Philos. Trans. R. Soc. Lond. B. Biol. Sci.*, vol. 362, no. 1484, pp. 1393–406, Aug. 2007.

[155] M. Malvè, a. P. Del Palomar, J. L. López-Villalobos, a. Ginel, and M. Doblaré, “FSI analysis of the coughing mechanism in a human trachea,” *Ann. Biomed. Eng.*, vol. 38, no. 4, pp. 1556–1565, 2010.

[156] D. Tang, C. Yang, S. Kobayashi, and D. N. Ku, “Effect of a Lipid Pool on Stress/Strain Distributions in Stenotic Arteries: 3-D Fluid-Structure Interactions (FSI) Models,” *J. Biomech. Eng.*, vol. 126, no. 3, p. 363, 2004.

[157] D. Tang, C. Yang, J. Zheng, P. K. Woodard, G. a Sicard, J. E. Saffitz, and C. Yuan, “3D MRI-based multicomponent FSI models for atherosclerotic plaques.,” *Ann. Biomed. Eng.*, vol. 32, no. 7, pp. 947–60, Jul. 2004.

[158] W. Wu, D. Pott, B. Mazza, T. Sironi, E. Dordoni, C. Chiastra, L. Petrini, G. Pennati, G. Dubini, U. Steinseifer, S. Sonntag, M. Kuetting, and F. Migliavacca, “Fluid–Structure Interaction Model of a Percutaneous Aortic Valve: Comparison

with an In Vitro Test and Feasibility Study in a Patient-Specific Case," *Ann. Biomed. Eng.*, vol. 44, no. 2, pp. 590–603, 2016.

[159] M. Xenos and D. Bluestein, "Biomechanical Aspects of Abdominal Aortic Aneurysm (AAA) and its Risk of Rupture: Fluid Structure Interaction (FSI) Studies," in *Biomechanics and Mechanobiology of Aneurysms*, T. McGloughlin, Ed. Berlin, Heidelberg: Springer Berlin Heidelberg, 2011, pp. 181–220.

[160] E. Birmingham, J. a Grogan, G. L. Niebur, L. M. McNamara, and P. E. McHugh, "Computational modelling of the mechanics of trabecular bone and marrow using fluid structure interaction techniques.," *Ann. Biomed. Eng.*, vol. 41, no. 4, pp. 814–26, Apr. 2013.

[161] C. Kamphues, D. Klatt, R. Bova, A. Yahyazadeh, M. Bahra, B. J., F. Klauschen, P. Neuhaus, and I. Sack, "Viscoelasticity-based magnetic resonance elastography for the assessment of liver fibrosis in hepatitis c patients after liver transplantation," *RoFo Fortschritte auf dem Gebiet der Rontgenstrahlen und der Bildgeb. Verfahren*, vol. 184, no. 11, pp. 1013–1019, 2012.

[162] Y. Guo, H. Lin, X. Zhang, S. Zhong, Y. Yin, and X. Chen, "Noninvasive Assessment of Liver Viscoelasticity by Acoustic Radiation Force with a Rat Model," *2013 9th Int. Conf. Information, Commun. Signal Process.*, pp. 1–4, 2013.

[163] W. C. Allsbrook, K. A. Mangold, M. H. Johnson, R. B. Lane, C. G. Lane, and J. I. Epstein, "Interobserver reproducibility of Gleason grading of prostatic carcinoma: General pathologist," *Hum. Pathol.*, vol. 32, no. 1, pp. 81–88, 2001.

[164] C. Mosquera-Lopez, S. Agaian, A. Velez-Hoyos, and I. Thompson, "Computer-Aided Prostate Cancer Diagnosis From Digitized Histopathology: A Review on Texture-Based Systems," *IEEE Rev. Biomed. Eng.*, vol. 8, pp. 98–113, 2015.

[165] L. S. Liebovitch and T. Toth, "A fast algorithm to determine fractal dimensions by

box counting," *Phys. Lett. A*, vol. 141, no. 8–9, pp. 386–390, Nov. 1989.

[166] J. Palacio-Torralba, D. W. Good, S. A. McNeill, R. L. Reuben, and Y. Chen, "Histology-based homogenization analysis of soft tissue: application to prostate cancer," *J. R. Soc. Interface*, vol. 14, no. 129, 2017.

[167] A. Mauri, A. E. Ehret, D. S. a. De Focatiis, and E. Mazza, "A model for the compressible, viscoelastic behavior of human amnion addressing tissue variability through a single parameter," *Biomech. Model. Mechanobiol.*, 2015.

[168] D. F. Gleason, "Histologic grading of prostate cancer: A perspective," *Hum. Pathol.*, vol. 23, no. 3, pp. 273–279, 1992.

[169] S. C. Barnes, B. M. Lawless, D. E. T. Shepherd, D. M. Espino, G. R. Bicknell, and R. T. Bryan, "Viscoelastic properties of human bladder tumours," *J. Mech. Behav. Biomed. Mater.*, vol. 61, pp. 250–257, Aug. 2016.

[170] X. Z. K.J.Bathe, H.Zhang, "Some advances in the analysis of fluid flows," *Comput. Struct.*, vol. 64, no. 5–6, pp. 909–930, Sep. 1997.

[171] K.J. Bathe, *ADINA Theory and Modeling Guide, Volume III: ADINA CFD , FSI*. 2012.

[172] U. ADINA R&D Inc., MA, "ADINA - Finite Element Analysis Software." [Online]. Available: http://www.adina.com/. [Accessed: 10-Jul-2017].

[173] J. Foucher, E. Chanteloup, J. Vergniol, L. Castéra, B. Le Bail, X. Adhoute, J. Bertet, P. Couzigou, and V. de Lédinghen, "Diagnosis of cirrhosis by transient elastography (FibroScan): a prospective study.," *Gut*, vol. 55, no. 3, pp. 403–8, 2006.

[174] E. E. W. Van Houten, M. M. Doyley, F. E. Kennedy, J. B. Weaver, and K. D. Paulsen, "Initial in vivo experience with steady-state subzone-based MR elastography of the human breast," *J. Magn. Reson. Imaging*, vol. 17, no. 1, pp.

72–85, 2003.

[175] R. Sinkus, J. Lorenzen, D. Schrader, M. Lorenzen, M. Dargatz, and D. Holz, “High-resolution tensor MR elastography for breast tumour detection.,” *Phys. Med. Biol.*, vol. 45, no. 6, pp. 1649–1664, 2000.

[176] Gill, W. Murray, and M. Wright, “The Levenberg-Marquardt Method,” *Pract. Optim. London Acad.*, pp. 136–137, 1981.

[177] F. Maceri, M. Marino, and G. Vairo, “A unified multiscale mechanical model for soft collagenous tissues with regular fiber arrangement.,” *J. Biomech.*, vol. 43, no. 2, pp. 355–63, Jan. 2010.

[178] W. Yao, Y. Li, and G. Ding, “Interstitial Fluid Flow: The Mechanical Environment of Cells and Foundation of Meridians,” *Evidence-Based Complement. Altern. Med.*, vol. 2012, pp. 1–9, 2012.

[179] Y. Wang and M. Insana, “Sbc2012-80 in Vivo Imaging of Dynamic Shear Modulus of Rodent Mammary Tumors,” pp. 2–3, 2012.

[180] S. Le Pense and Y. Chen, “Contribution of Fluid in Bone Extravascular Matrix to Strain-Rate Dependent Stiffening of Bone Tissue – A Poroelastic Study,” *J. Mech. Behav. Biomed. Mater.*, vol. 65, pp. 90–101, 2016.

[181] U. S. Army, “Determining Viscoelastic Strain Data a Prony Material Series for a From Time Varying,” no. May, 2000.

[182] L.-M. Su, *Early Diagnosis and Treatment of Cancer Series: Prostate Cancer*. Saunders/Elsevier, 2010.

[183] B. Turkbey, A. M. Brown, S. Sankineni, B. J. Wood, P. a Pinto, and P. L. Choyke, “Multiparametric Prostate Magnetic Resonance Imaging in the Evaluation of Prostate Cancer,” *Ca Cancer J Clin*, vol. 0, no. 0, pp. 1–11, 2015.

[184] J. Xu, P. A. Humphrey, A. S. Kibel, A. Z. Snyder, V. R. Narra, J. J. H. Ackerman,

and S.-K. Song, "Magnetic resonance diffusion characteristics of histologically defined prostate cancer in humans.," *Magn. Reson. Med.*, vol. 61, no. 4, pp. 842–50, Apr. 2009.

[185] S. Phipps, T. H. J. Yang, F. K. Habib, R. L. Reuben, and S. a McNeill, "Measurement of tissue mechanical characteristics to distinguish between benign and malignant prostatic disease.," *Urology*, vol. 66, no. 2, pp. 447–50, Aug. 2005.

[186] K. E. Herold, W. E. Bentley, J. Vossoughi, P. G. Young, D. Raymont, V. Bui Xuan, and R. T. Cotton, "IFMBE Proceedings 32 - New Tools for Image-Based Mesh Generation of 3D Imaging Data," *IFMBE Proc.*, vol. 32, pp. 470–472, 2010.

[187] H. Zhang, X. Zhang, S. Ji, Y. Guo, G. Ledezma, N. Elabbasi, and H. deCougny, "Recent development of fluid–structure interaction capabilities in the ADINA system," *Comput. Struct.*, vol. 81, no. 8–11, pp. 1071–1085, May 2003.

[188] J. L. Peterson, L. A. Vallow, S. L. Hines, and S. J. Buskirk, "Ductal carcinoma in situ of the breast," *Oncol. Rev.*, vol. 3, no. 4, pp. 237–246, 2009.

[189] S. P. Sutera and R. Skalak, "THE HISTORY OF POISEUILLE'S LAW," *Annu. Rev. Fluid Mech*, vol. 993, no. 259.

[190] P. Cazeaux and C. Grandmont, "Homogenization of a multiscale viscoelastic model with nonlocal damping, application to the human lungs," *Math. Model. Methods Appl. Sci.*, vol. 25, no. 6, pp. 1125–1177, Jun. 2015.

[191] H. M. Müller, P. H. Rehak, M. Puchinger, D. Wagner, W. Marte, and K.-H. Tscheliessnigg, "Measurement of cardiac output and pulmonary transit time for assessment of pulmonary vascular resistance in domestic piglets," *Exp. Physiol.*, vol. 94, no. 6, pp. 659–664, Jun. 2009.

[192] P.-H. Jarreau, B. Louis, G. Dassieu, L. Desfrere, P. W. Blanchard, G. Moriette, D. Isabey, and A. Harf, "Estimation of inspiratory pressure drop in neonatal and

pediatric endotracheal tubes," *J. Appl. Physiol.*, vol. 87, no. 1, 1999.

[193] J. H. Kim, J. K. Kim, B.-W. Park, N. Kim, and K.-S. Cho, "Apparent diffusion coefficient: Prostate cancer versus noncancerous tissue according to anatomical region," *J. Magn. Reson. Imaging*, vol. 28, no. 5, pp. 1173–1179, Nov. 2008.